The Dissertation Committee for Joseph Frederic Tansey Certifies that this is the approved version of the following dissertation:

Multiscale Pore Network Modeling of Carbonate Acidization

Committee:

Matthew Balhoff, Supervisor

David DiCarlo

Larry Lake

Maša Prodanović

Murtaza Ziauddin

Multiscale Pore Network Modeling of Carbonate Acidization

by

Joseph Frederic Tansey, B.S.P.E.; M.S.E.

Dissertation

Presented to the Faculty of the Graduate School of

The University of Texas at Austin

in Partial Fulfillment

of the Requirements

for the Degree of

Doctor of Philosophy

The University of Texas at Austin

December 2016

Acknowledgements

First, I would like to thank my graduate advisor, Dr. Matthew Balhoff, for his extensive support and guidance during this work. His expertise, both technical and professional, has been instrumental towards the progress and quality of this research. He has shown great initiative and thoughtfulness, allowing me to diverge from the path when I believed strongly in the academic merit of alternative solutions, while also keeping me focused on achieving our original goals.

I also greatly appreciate my committee members. Dr. Murtaza Ziauddin, for providing raw experimental data through Schlumberger to support our modeling, as well as the founding impetus for this research. Dr. Maša Prodanović, for providing feedback and expert opinion on the construction and quality of network models extracted from carbonates. Dr. Larry Lake, for attending my many SPE poster presentation meetings and helping me represent UT to the best of my abilities at ATCE 2015. Dr. David DiCarlo, for his continued friendship and guidance since I was an undergraduate in his thermodynamics class.

I would additionally like to thank Dr. Yashar Mehmani, who in addition to being a great friend, is also a brilliant engineer and scientist. While the benefits of being able to use his mortar coupling code to supplement my thesis are obvious, his extensive academic achievements always inspired me to reach deeper and more rigorously in my own work.

Finally, I would like to acknowledge my colleagues and friends, Dr. Tie Sun, Nkem Egboga, Pengpeng Qi, and Hongtao Yang. Whether you helped my research directly or were just there to bounce ideas off, I appreciated you greatly.

Multiscale Pore Network Modeling of Carbonate Acidization

Joseph Frederic Tansey, Ph.D.

The University of Texas at Austin, 2016

Supervisor: Matthew Balhoff

Matrix acidization is important in many applications, particularly near-wellbore stimulation in carbonate reservoirs. Ideally, injected acid creates an array of highly conductive channels that greatly enhance permeability. A pore network model of matrix acidization is developed to predict this optimal injection rate, using novel representations of pore-scale physics in the form of a mass transfer coefficient and pore-merging criterion. Results are presented for both computer generated sphere packs and networks extracted from CT scans of carbonates. Simulations return an optimal Damköhler number close to experimental optimums, but predict significantly higher pore volumes to breakthrough than most experiments. This is posited to be due to the small domain size of network models.

Mortar coupling is employed as a domain decomposition technique, and is verified to accurately capture the unique physics of matrix acidization. Many networks are coupled together to extend the simulated domain size in a parallel computing environment. A hybrid modeling technique is used to simplify large-scale simulations with the inclusion of Darcy-scale grid blocks in nonreactive regions. This is shown to preserve a high degree of simulation accuracy while improving computation time substantially.

A two-scale continuum model is developed for integration with the hybrid technique. A pore network model is used to develop and upscale mass transfer coefficients, porosity-permeability relationship, and other structure-property relations. The resultant two-scale continuum model is shown to preserve a high degree of accuracy at high injection rates, but falls short of capturing intermediate dissolution regimes due to insufficient description of pore-scale species channeling. Simulations on larger domain sizes show reduced pore volumes to breakthrough. Radial domains are also investigated and show the characteristic dissolution regimes, lending support to common field-scale acidizing practice. Two-scale continuum models are concluded to be accurate representations of pore scale physics that can be used efficiently at larger scales. However, pore-scale modeling is still necessary to calibrate input parameters for the two-scale continuum model without resorting to destructive acidization experiments.

Table of Contents

List of Tables

List of Figures

CHAPTER 1: INTRODUCTION

Approximately half of global oil reserves are found in carbonate reservoirs (Klemmel, 2013). Low-permeability carbonates (<10 mD) are ideal candidates for acid fracturing, whereby injection at high pressure causes fractures to form, and remain enlarged by means of acid etching (Abass et al., 2006). Acid fracturing is distinguished from matrix acidization, where the goal is to dissolve the pore space without fracturing the formation. Matrix acidization is a cost effective production technique used to stimulate carbonate formations, ameliorating compacted or crushed-zone damage to the wellbore during drilling (McLeod, 1984). Matrix acidization forms deep and penetrating channels known as "wormholes" that dramatically increase well productivity (Bazin, 2001).

Strong acids, such as hydrochloric acid (HCl), are typically used in matrix acidizing to enhance the near-wellbore permeability. Highly conductive wormhole channels are formed in the ideal case (Figure 1.1A), greatly enhancing wellbore production. Traditional field practice has tended towards injecting acid at the maximum allowable rate (Williams et al., 1979; Paccaloni and Tambini, 1993). However, inefficient acid delivery can result in poor permeability improvement and the failure to establish strong channeling. Injection speed, acid concentration, acid volume, and acid type, can be controlled to achieve a high permeability response while using minimal acid (Wang et al., 1993). The industry standard for "optimum" is the minimum "pore volumes to breakthrough" (PVBT), with decreasing performance outside this value (Figure 1.1B).

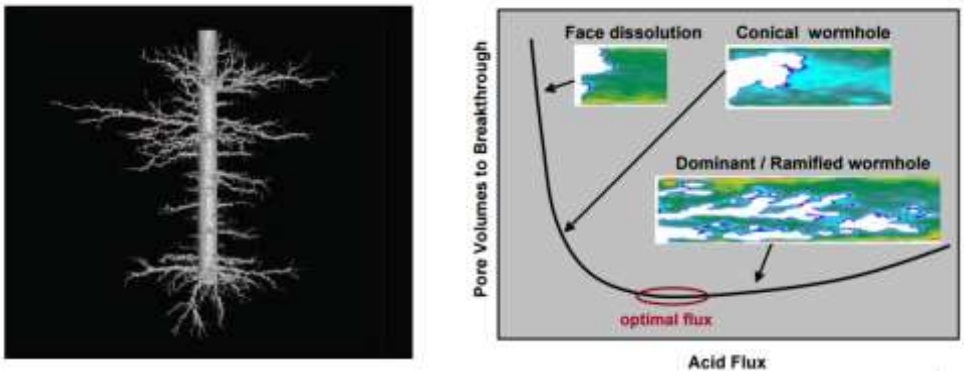

(A) (B)

Figure 1.1: (A) An X-ray image of wormhole formed in ~1m^3 carbonate block. A pseudo-wellbore has been drilled through the middle. Injected acid forms branching wormholes away into the "formation". (B) Pore volumes to breakthrough versus acid flux. Both images from McDuff (2010).

Many models have been developed to predict the process of matrix acidizing (Daccord et al., 1989; Hung et al., 1989; Fredd and Fogler, 1998b; Buijse and Glasbergen, 2005; Maheshwari et al., 2013). The primary goal of these models is to predict optimal injection conditions for a given rock type, or to predict the number of pore volumes to breakthrough during treatment. Semi-empirical models (Gong, 1999; Talbot, 2008), often provide a good fit to experimental of field data of acidizing, but require input parameters that must be determined experimentally. For example, two-scale continuum models (Panga et al., 2005; Maheshwari et al., 2013) utilize small continuum scale grid blocks to simulate a core-scale experiment (approximately 1" diameter, 6" length). Darcy's law is used to simulate the flow field, and properties such as permeability and porosity are ascribed to each block. Two-scale continuum models match core-flood experiments of acidization extremely well (in addition to being able to

simulate domain sizes large enough to capture an entire core-scale experiment), but require calibration with core acidizing trials in order to establish a porosity/permeability relationship. The two-scale continuum models are reported in the literature to be extremely sensitive to this parameter (Maheshwari et al., 2013), and it is not clear that once calibrated these models can successfully predict permeability response at larger scales or for different rock/fluid systems.

Pore-scale models of acidization allow for modeling the fundamental flow and transport equations on a physical representation of the pore space and require no destructive experiments for calibration. However, they often fail to be predictive of acidiziation experiments conducted in core floods because an oversimplified geometry or equations are used. They range in complexity from modeling the wormhole as a growing cylindrical tube (Schechter et al., 1969), to direct Lattice-Boltzmann simulation of dissolution on pore space from a micro-CT image (Kang et al., 2014). While the latter is a rigorous representation of pore-scale physics, dissolution of only a few pores in 2D can be studied at a given time due to computational constraints of direct methods and thus it is difficult to reach a representative elementary volume (REV).

Pore-network models represent an intermediate resolution method, where physics are still simulated on a physically representative domain, but approximations to the geometry (as pore nodes connected by throat bonds) allow larger domain sizes to be studied. Fredd and Fogler (1998b) presented a 3D physically-representative pore network model of carbonate acidization. The model included transport, reaction, and dissolution of the pore space, with inputs derived from fundamental experiments or analytic relations

(e.g. Levich's (1962) expression for mass transfer). The model was able to reproduce the qualitative trends observed on core scale experiments, namely face dissolution, wormholing, and uniform dissolution. However, optimal injection rate was overpredicted by a factor of ~10. Additionally, the number of pore volumes to breakthrough was much higher than is typically seen in experiments.

One major problem with single network models is the small simulation domain (~1 mm^3) is many orders of magnitude smaller than core-scale experiments (~5×10^5 mm^3). Core scale experiments are in turn even smaller than actual field-scale wormholes, thought to extend at least one meter into the reservoir (Buijse and Glasbergen, 2005). This provides an impetus to determine how large simulations and experiments need to be in order to reach an REV that is predictive of field-scale wormholing. Qiu et al. (2013) argued that even core-scale experiments are below the REV for field-scale wormholing because they are not long enough to adequately spend acid before it reaches the tip of the wormhole. Regardless, it is likely that pore network models are below the representative elementary volume (REV) for wormholing and simple upscaling may be insufficient.

Mortar coupling is a domain decomposition technique that has allowed pore network models to simulate larger domains by parallelizing subdomain solutions (Balhoff et al., 2008; Mehmani et al., 2012a) while maintaining solution accuracy. Briefly, the technique is able to link subdomains together continuously at the interface using "mortars", a coarse grid representation of physical variables at the interface. The mortars project boundary conditions onto subdomains in an iterative fashion such that mass and species flux are matched to within a prescribed tolerance. Mehmani et al. (2012a)

simulated reactive transport on 64 mm^3 of domain size, while Sun et al., (2012) simulated the flow field in ~ 0.0075 m^3. Both authors utilized a single high-performance computer (HPC), and therefore it is plausible that a much larger domain size can be simulated in a distributed computing environment.

In addition to domain size issues, existing pore network models (Hoefner and Fogler, 1989; Fredd and Fogler, 1998b; Syzmczak and Ladd, 2009) have failed to quantitatively predict optimal injection strategies due to an incomplete description of pore-scale physics. Reaction rate expressions are often upscaled from measurements in macroscopic experiments. For example, reaction rate coefficients can be determined from spinning disc, flow-through reactor, or continuous fluidized bed reactor experiments. These results may not be applicable to reaction rates in individual pores, as the smaller scale magnifies the effects of mass transfer resistance and concentration gradients. Raoof et al. (2010) demonstrated the importance of incorporating kinetics developed for the pore scale, rather than relying on macroscopic averages.

Finally, network models involving significant matrix dissolution treat pore growth and overlap in an *ad hoc* fashion. For example, Fredd and Fogler (1998b) allowed pores to grow until their constituent grains are dissolved, at which point pore growth and reactant consumption is no longer modeled. Therefore, a large volume of completely "dissolved" space will actually be composed of a network of pores and throats, which all continue to provide resistance to flow. A quantitatively accurate pore network model of advanced matrix dissolution must allow complete dissolution of the grain space. A novel pore-merging algorithm to achieve this goal is presented and validated.

The dissertation is outlined as follows: Chapter 2 is an extensive literature review. First, the theory and experiments surrounding injection optimization are discussed. Second, semi-empirical and continuum scale models of acidization are described. Last, pore scale models of reactive transport and dissolution are reviewed and critiqued. Literature verifying the accuracy of pore scale models and mortar coupling techniques is also reviewed.

The basic pore scale model of matrix dissolution is presented in Chapter 3. A novel pore-scale mass transfer coefficient and pore merging criterion are defended and shown to be critical to capturing the familiar dissolution regimes. Sensitivity analysis shows that accurate pore merging is a critical component missing from past network models of matrix dissolution.

In Chapter 4 the pore scale model of matrix dissolution is used for networks constructed from micro-CT scans of carbonate cores. Experiments provided by Schlumberger are available for comparison. Network agreement with tracers is generally poor, which is attributed to insufficient domain size. However, when tracers match well, optimal injection rate is predicted near that of experiments.

Chapter 5 applies mortar coupling techniques to the pore scale model of matrix dissolution. Permeability and non-reactive tracers are compared between a single-network simulated as above, and the same network split into two subdomains. Permeability and nonreactive tracers are shown to match almost perfectly. Problems unique to matrix dissolution arise and novel modules must be adapted to merge pores

across boundaries. Mortars are shown to be extremely accurate in capturing permeability response during dissolution when compared to solution on a single domain.

Chapter 6 extends mortar coupling to larger domain sizes. First, a hybrid model is introduced using Darcy-scale grid blocks to model nonreactive subdomains. Second, a two-scale continuum model is developed to model reactive subdomains. A hybrid modeling technique utilizing this two-scale continuum model under certain conditions is shown to provide a favorable tradeoff between simulation resolution and computation time. Large-scale examples utilizing the two-scale continuum model show effects of domain size and wellbore geometry.

Chapter 7 discusses overarching conclusions and outlines areas of future work.

Chapter 2: Literature Review

2.1 Introduction to Acidizing

Matrix acidization has been employed extensively during hydrocarbon recovery for many purposes. Hydrofluoric acid is commonly used to remove near wellbore damage in sandstone reservoirs (Smith and Hendrickson, 1965), however permeability response in sandstones is modest and requires large volumes of acid to achieve the desired effect (McLeod, 1986). Acid is also injected in the context of acid fracturing in low permeability carbonate reservoirs to create long, acid-etched fractures (Navarrete et al., 1998). Most frequently, however, is the use of strong acids, such as hydrochloric (HCl) to quickly dissolve moderate and high permeability carbonate reservoirs. The reaction expression is given by:

$$2H^+ + CaCO_3 \rightleftarrows CO_2 + Ca_2^+ + H_2O \tag{2.1}$$

The backwards rate expression is usually found to be negligible, and the reaction goes very quickly to completion (Williams et al., 1970). CO_2 evolution is commonly believed to remain in the aqueous phase at typical reservoir pressures (Mumallah et al., 1991). HCl/Calcite systems are often mass-transfer limited, where reaction at the fluid/solid boundary is extremely fast compared to the rate of species transport to the solid. The dissolution of calcite using HCl is mass transfer limited above 0 degrees Celsius (Lund et al., 1975).

The primary goal of matrix acidization is to enhance the near-wellbore conductivity. In the ideal case, highly conductive wormholes are formed, reducing near wellbore skin, and therefore increasing the permeability of the rock. Improper stimulation design can result in lackluster productivity due to inefficient placement of the acid (Thomas et al., 1998). Field stimulation strategy is also constrained by factors such as the maximal injection rate (Huang et al., 2000). Choice of fluid type, injection rate, and injection concentration are key design parameters to maximize the stimulation effect (Wang et al., 1993). Wormholes are believed to form because of the natural heterogeneity of carbonates, whereby acid flows preferentially through high-permeability pathways. These high-permeability pathways are enlarged, and in turn divert more acid to themselves. Dominant channels form which provide negligible resistance to flow around the wellbore.

Productivity increases observed in field conditions vary widely. Al-Dahlan et al. (2000) recorded a tripling of the injectivity index in a carbonate water disposal well. Mohamed et al. (1999) studied over 80 water injectors in carbonate reservoirs treated with hydrochloric acid below the fracture gradient. They found injectivity increased by approximately a factor of two.

2.2 INJECTION OPTIMIZATION

An optimal injection rate is generally associated with wormhole formation. Optimality is defined in terms of minimizing pore volumes to breakthrough (PVBT), where “breakthrough” is defined many ways in the literature, although it generally refers

to percolation of acid to the end of the domain (Fredd and Fogler, 1998b; Wang et al., 1993; Nasr-El-Din et al, 2015). Injecting too slowly results in "compact dissolution" around the wellbore face, where acid primarily dissolves the domain inlet, and a negligible permeability response. Injecting too quickly disperses the acid out into the formation, resulting in poorly connected "uniform dissolution". An intermediate rate is thought to correspond to an ideal wormholing case that provides a strong permeability increase for some minimum treatment criterion. Computed Tomography (CT) scans of cores acidized across a range of injection rates show characteristic dissolution regimes (Figure 2.1).

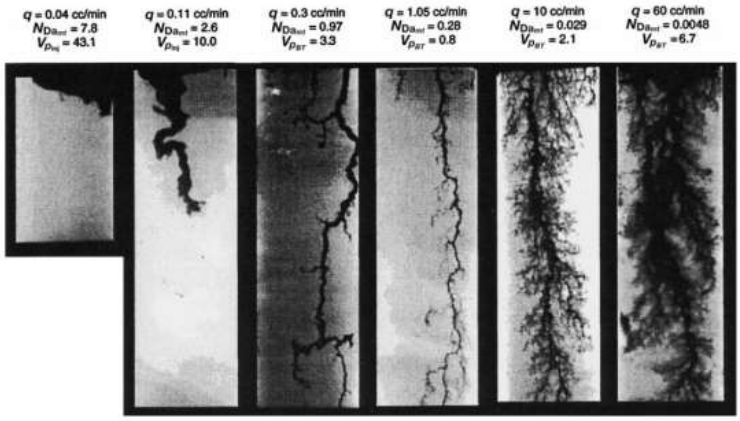

(a) (b) (c) (d) (e) (f)

Figure 2.1: Compact dissolution (a), Wormholing (c-d), Uniform Dissolution (f). (Fredd and Fogler 1996)

Numerous authors have attempted to obtain a general criterion or expression for the optimal injection rate. A transition pore-size approach was formulated by Wang (1993), hypothesizing that wormhole formation could not begin until local pores reached

a certain level of dissolution, which in turn was related to the Damköhler number. Semi-empirical relations were presented by Gong (1999) and Talbot (2008), assuming acid dissolution along a wormhole of characteristic length, bond length, bond diameter, and several other constants. These models showed good agreement with experiments, but require many laboratory measurements, limiting their utility as predictive models.

Fredd and Fogler (1998b) measured breakthrough trends for various fluid/rock systems (limestone, plaster, CDTA, DTPA, EDTA, HCl, HAc), and showed their behavior collapsed onto a single type curve if plotted in terms of a Damköhler number. The Damköhler number is defined as the ratio of the net rate of dissolution by acid to the rate of convective transport of acid (Eqn. 2.2),

$$Da_{mt} = 6.33\left(\frac{LD_e}{Q}\right)^{(2/3)}. \tag{2.2}$$

where L is the length of the domain, D_e is the effective diffusion coefficient, and Q is the volumetric flow rate (Fredd and Fogler, 1999). The coefficients 6.33 and 2/3 come from Levich's (1962) expression for mass transfer in a cylindrical tube. Under their interpretation, the optimum injection conditions are assumed to be independent of domain cross section due to wormhole diversion of flow away from the bulk domain. Thus, the Damköhler number includes both the injection rate and concentration of acid. An optimal Damköhler number of 0.29 was observed for the studied fluid/rock systems (Figure 2.2).

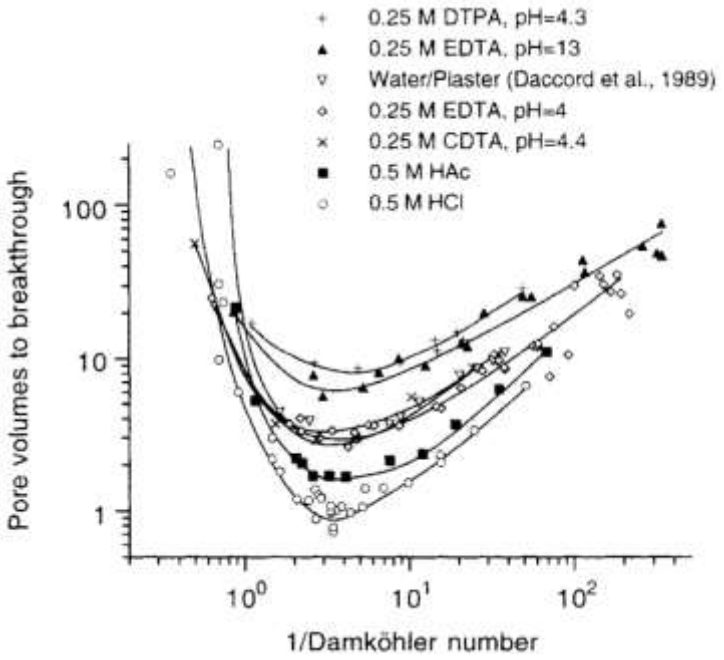

Figure 2.2: Pore volumes to breakthrough plotted versus inverse Damköhler number for a variety of rock/fluid systems, primarily limestone 15-20% porosity and 0.8 to 2 mD permeability (Fredd and Fogler, 1998b). Most trials show an optimal Damköhler number close to 0.29.

2.3 UPSCALING LABORATORY AND SIMULATION RESULTS

The Fredd and Fogler (1998b) experiments suggest that a universal optimum Damköhler number exists that can be extrapolated to all scales. However, their experiments were conducted on cores of a single dimension (1.5" diameter × 4" length). Therefore, it is unknown whether the same optimal Damköhler number would be found for larger samples. This problem was investigated in Bazin (2001), who conducted acidizing experiments on cores of different length (5cm and 20cm) and reproduced pore volumes to breakthrough curves for a variety of injection rates (Figure 2.3), showing that an increase in core length increased optimal injection rate.

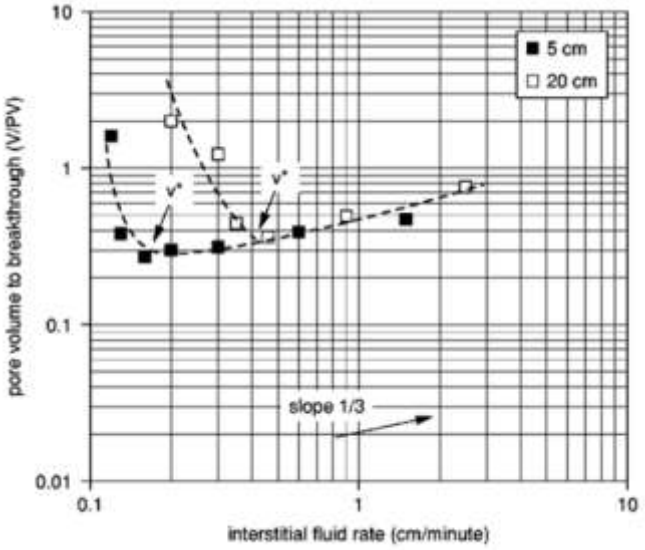

Figure 2.3: Comparison of pore-volumes-to-breakthrough curves generated by Bazin, 2001 for different length cores.

Figure 2.3 predicts that an increase in domain length required a proportionate increase in flow rate. This result is summarized in terms the Damköhler number in Table 2.1.

Table 2.1: Injection rate and Damköhler number corresponding to optimal breakthrough in Bazin (2001) experiments.

Length (cm)	Experimental Optimum Injection Rate (cc/sec)	Damkohler Number (Eqn 2.2)
5	0.05	0.14
20	0.15	0.18

While neither result exactly matches the predicted optimal value of 0.29, the values are likely within expected variance, given the initial spread of Fredd and Fogler's (1998b) results. Additionally, Bazin's data have sufficient scatter, leading to some uncertainty in the optimum injection rate. An interstitial injection rate of 0.6 cm/min in

the 20 cm core would have corresponded to a Damköhler number of 0.14, but only 0.45 (Da = 0.17) and 0.9 (Da = 0.11) cm/min are investigated as data points. This highlights an inherent difficulty in studying optimal injection conditions, as the range of trial injection rates must be large enough to capture the characteristic dissolution regimes, but fine enough to distinguish the optimal injection conditions. Thus results from the Bazin (2001) experiments are inconclusive regarding the size for a representative elementary volume problem with acidization. In fact, when the optimal injection rates studied are converted to a Damköhler number, they are consistent with Fredd and Fogler (1998b)'s hypothesis of a domain size independent optimal Damköhler number.

While the optimal injection conditions may be independent of domain size, pore volumes to breakthrough curves seem to vary by up to two orders of magnitude depending on rock/acid type. The Bazin (2001) experiments (Figure 2.3) on different length carbonate cores showed that a "four-fold increase of wormhole length requires a seven-fold higher volume of acid and a higher injection rate". This implies that pore volumes to breakthrough varies nonlinearly with domain size, or that qualitatively different wormhole patterns form as domain size increases. So while optimal injection strategy may be scale independent, pore volumes to breakthrough is likely not.

The purpose of core scale experiments is generally to inform field scale treatment recommendations. However, core flood experiments are typically performed in 1D, and the impact of wormhole competition and radial (as opposed to linear) flow significantly impacts wormholing patterns (Gdanski, 1999). This is due to the dependence of interstitial velocity on radial distance from the wellbore in real acidizing jobs (Buijse,

2005). Therefore, while there is not a direct approach to upscale core experiments, they are still useful for model calibration. Ideally, these models can be extended to radial flow regimes, which can in turn yield more reliable recommendations for the field scale.

2.4 NON-NEWTONIAN FLUIDS

Non-Newtonian fluids are also of interest for their ability to improve acid placement in formations. Lungwitz et al. (2007) studied a viscoelastic acid system in core floods that increases in viscosity as acid is spent. While self-diverting fluids are typically believed to be most useful in acid-fracturing applications, Al-Mutawa et al. (2003) found that viscoelastic self-diverting acid was highly effective for matrix acidizing in a field study involving multi-layered carbonate structures (3md to 400md). The authors claim that diversion of acid away from highly permeable zones results in better acid coverage, and report productivity increases of 2-4 in all 17 wells treated. Similarly, Nasr-El-Din et al. (2006) reported a 95% success rate of 20 wt% hydrochloric acid system with viscoelastic surfactant in conventional carbonate reservoirs. Increased viscosity is thought to improve stimulation of low-permeability zones that would otherwise receive negligible acid contact (Buijse et al., 2000).

The mechanism for self-diversion is well understood. In unspent viscoelastic acids, polymers are linked together efficiently in spherical micelles. However, as the acid is spent, these micelles unravel and the polymers become tangled, increasing viscosity significantly (Figure 2.4). This is believed to improve acid coverage as high-permeability

domains that initially receive the most flow will become plugged with spent acid, allowing fresh acid to contact less permeable zones.

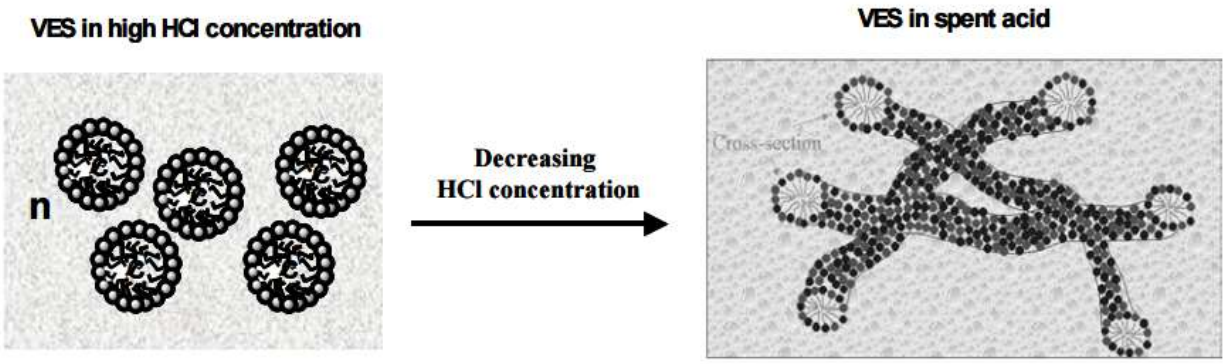

(A) (B)

Figure 2.4: Image of viscoelastic self-diverting acid (Taylor et al., 2003). Spherical micelles (A) flow easily in unspent acid. As acid spends, the micelles unravel and become tangled (B), increasing viscosity.

In addition to viscoelastic acids, gelled emulsified acids are often utilized for their retardation of acid consumption. Bazin and Abdulahad (1999) conducted experiments showing that breakthrough of emulsified acid is almost insensitive to injection rate, a finding at odds with the "optimal Damköhler number" theory that describes Newtonian water-based acids. Sayed et al. (2012) also report deep wormholes with emulsified acid across two orders of injection magnitude, with no observable face dissolution regime, despite finding that dissolution by emulsified hydrochloric acid is still mass transfer limited (Sayed et al., 2013). Assuming that all cores exhibit similar levels of dissolution at "breakthrough", this suggests the possibility that the diffusion coefficient varies favorably with injection rate.

Emulsified acid is commonly cited as diffusing about 10 times slower than water based formulations (de Rozieres et al., 1994; Navarrete et al., 1998). The Stokes-Einstein relation for Brownian diffusion lends some theoretical support for this phenomenon (Eqn 2.3),

$$D_B = \frac{R_g T}{6\pi N_a r_D \eta} \qquad (2.3)$$

where R_g is the universal gas constant, N_a is Avogadro's number, η is viscosity, and r_d is the droplet radius. However, Al-Mutairi et al. (2009) conclude that Brownian diffusion does not describe acid-droplet systems, even qualitatively. Attempts to relate droplet size to fundamental equations fall short by approximately an order of magnitude (de Rozieres et al., 1994). However, Al-Mutairi et al. (2009) report a strong relationship between the diffusion coefficient and droplet size of emulsified acid.

Hansford and Litt (1968) present a semi-empirical relationship, predicting that dissolution rate scales with disk rotational speed to the power [1/(1+n)] (Eqn 2.4),

$$K_{mt} = \varphi(n) D^{2/3} \left(\frac{k}{\rho}\right)^{\frac{-1}{3(1+n)}} a^{\frac{1-n}{3(1+n)}} \omega^{\frac{1}{1+n}} \qquad (2.4)$$

where φ(n) are tabulated empirical constants across a range of power law indices, *n*, *D* is the diffusion coefficient, *k* is the power law index, *a* is disk radius, and ω is angular disk velocity.

This empirical model shows agreement with experiments conducted on non-Newtonian acids, including power law fluids studied by de Rozieres et al., 1994. A

dynamic mass transfer coefficient could play a large role in explaining why emulsified acid performance is almost invariate with injection rate.

Zakaria et al. (2015) conducted a series of acidizing experiments using emulsified acid on carbonate cores. The familiar pore volumes to breakthrough curve was reproduced for each of the rock types (Figure 2.5) and correlated with the rock-types' "flowing fraction", defined as the "cumulative pore volume injected corresponding to the normalized tracer concentration at $C/C_0 = 0.5$)". All rock types showed a similar optimal injection rate, which is consistent with the optimal Damköhler number discussed above for Newtonian acids.

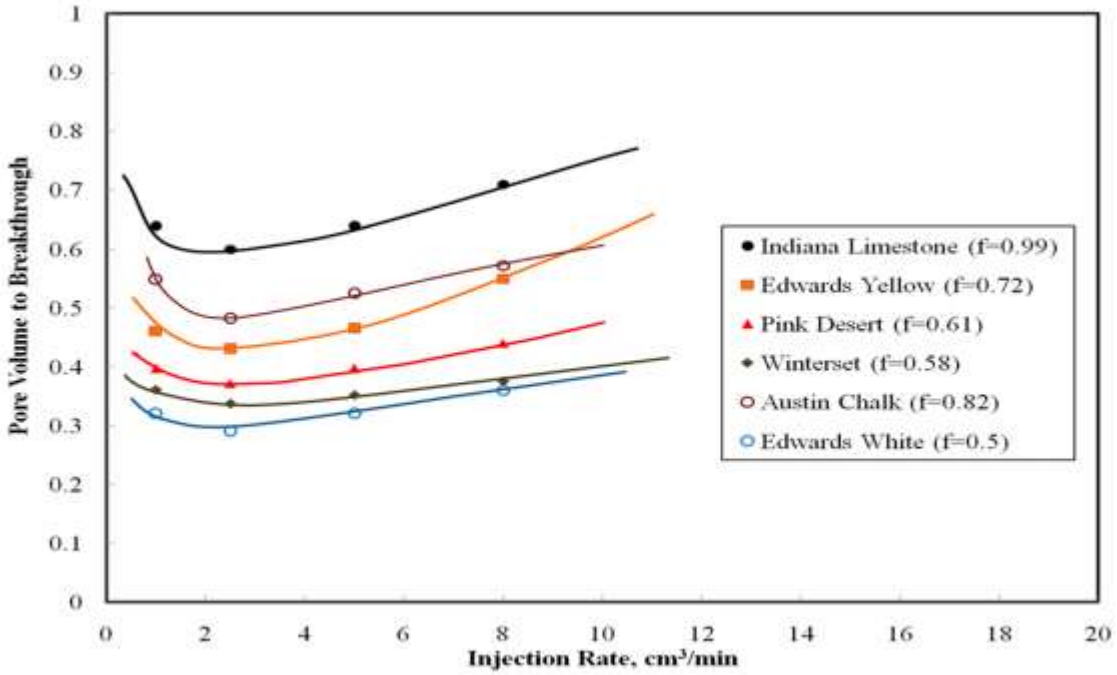

Figure 2.5: Pore volumes to breakthrough curve for different rock types using emulsified acid (Zakaria et al., 2015), where *f* is the flowing fraction.

Importantly, a power law relation was found to describe fluid rheology during acid spending (Eqn 2.5),

$$\mu_{eff} = k\left(\gamma\right)^{n-1} \qquad (2.5)$$

where k is the flow consistency index, γ is the shear rate, and n is the flow behavior index . Zakaria et al. (2015) found a value of $n \sim 0.6$ across a range of 1 to 1000 s^{-1} shear rate, indicating a strongly shear-thinning fluid in this region.

2.5 EARLY MODELS OF ACIDIZATION

Many models have been proposed that qualitatively and quantitatively capture the acidizing process. Early capillary tube models captured the propagation of wormholes under rigid assumptions. Schechter et al. (1969) studied the evolution of pore size distribution by considering an array of short cylinders distributed randomly throughout a solid. Glover (1973) experimentally verified Schechter's predicted change in pore size distribution by using sintered glass disks. Hung et al. (1989) modeled the wormhole as a growing cylindrical tube inside a solid core, using Darcy's law and coupling the wormhole/core interface (Figure 2.6). The core grows in width and length as acid is injected. Results show increasing wormhole length with increasing injection rate. Simulations on growth of multiple wormholes suggest that a dominant wormhole is more likely with a high diffusion rate or a low fluid-loss rate. No experimental comparisons were made.

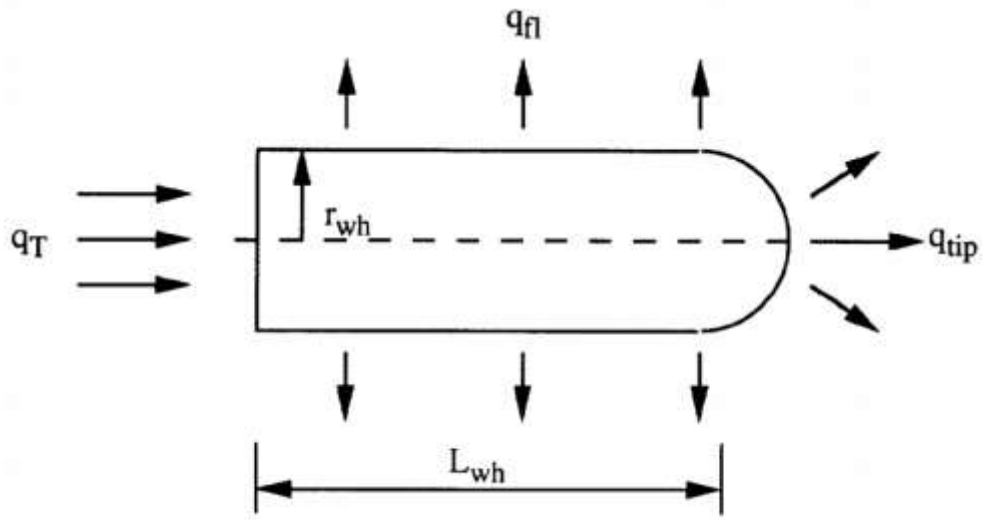

Figure 2.6: Schematic of fluid leakoff and tip propagation during wormhole growth employed by Huang (1997). Hung et al. (1989) and Huang et al. (2000) used similar models.

Walsh et al. (1982) modeled the effect of acidization and precipitation on permeability for various minerals, using a semi-empirical relationship between permeability and porosity. Their results correlate well with experimental data, although no acidizing regimes are produced. Walsh et al. (1984) extended this work in porous media using a 1D reactive model, successfully predicting the distribution roll-front uranium deposits. Huang (1997) and Huang et al. (2000) extended this capillary model to field conditions using Darcy's law in radial flow, concluding that fluid loss from wormholes in field treatments exceeds that found in linear corefloods, thus overpredicting wormhole formation in field conditions.

Numerous authors have attempted to obtain a general criterion or expression for the optimal injection rate. A transition pore-size approach was formulated by Wang et al.

(1993). Semi-empirical relations were presented by Gong and El-Rabaa (1999) and Talbot and Gdanski (2008), which showed good agreement with experiments, but require many laboratory measurements. For example, Talbot and Gdanski (2008)'s final expression for wormhole frontal velocity is given in Eqns 2.6 and 2.7

$$V_{wh} = W_{eff} \cdot (V_i \cdot \Phi)^{2/3} \cdot B(V_i) \qquad (2.6)$$

$$\Phi = a_1 \cdot \phi^{a_2} \cdot k^{\delta} \qquad (2.7)$$

where W_{eff} is the wormhole efficiency factor, Φ is the morphology factor, and $B(V_i)$ is the "wormhole B-function".

These variables are given by correlations with permeability, core length, core area, and temperature. For example, the expression for Φ is given in Eqn 2.6, where a_1 and a_2 are regression coefficients, k is the permeability, and δ is a function of porosity and two more regression coefficients. While the models provide an extremely good fit to the chosen experimental database, the predictive value this has for more complex rock/fluid systems is unclear, particularly at scales larger (or smaller) than the cores studied.

2.6 CONTINUUM MODELS OF ACIDIZATION

Several Darcy-scale models have been used to describe the dissolution process. Chen et al. (1997) presented an early Darcy-scale model of acidization, calibrating reaction and dissolution rates using acidizing experiments. Golfier (2002) presented a 3D

Darcy scale finite-difference model using 201×101 nodes (Figure 2.7). Briefly, the model solves pressure using Darcy's law (eqn 2.8),

$$U = \frac{1}{\mu} \overline{\overline{K}} \cdot \nabla P \qquad (2.8)$$

where $\overline{\overline{K}}$ is the permeability tensor, P is the pressure. The advection diffusion reaction equation is also solved (eqn 2.9),

$$\frac{\partial(\varepsilon C_f)}{\partial t'} + \nabla \cdot (U C_f) = \nabla \cdot (\varepsilon D_e \cdot \nabla C_f) - k_c a_v (C_f - C_s) \qquad (2.9)$$

where ε is the porosity, C_f is the cup-mixing concentration of the acid, C_s is the concentration of acid at the fluid-solid interface, D_e is the effective dispersion tensor, k_c is the local mass transfer coefficient, and a_v is the interfacial area. Individual blocks were assumed to have a homogeneous permeability.

The classical Kozeny-Carman relationship between porosity and permeability was chosen (eqn 2.10),

$$\frac{K}{l^2{}_\beta} = k_{cte} \left(\frac{\varepsilon_\beta}{1-\varepsilon_\beta}\right)^3 \qquad (2.10)$$

where K is the porosity, $l^2{}_\beta$ is the characteristic pore-scale length, ε_β is the porosity, and k_{cte} is an empirical constant.

The model was able to capture the characteristic dissolution regimes, and with the selection of appropriate length scales, reproduced the optimal Damköhler number of around 0.29 from Fredd and Fogler (1998b). The model is very sensitive to the choice in

mass transfer coefficient, whose selection depends on an arbitrary shape-factor coefficient and the local Péclet number. Their optimal Damköhler number is identified on the basis of maximizing wormhole length, rather than reaching a permeability threshold, which makes comparison with core scale experiments difficult.

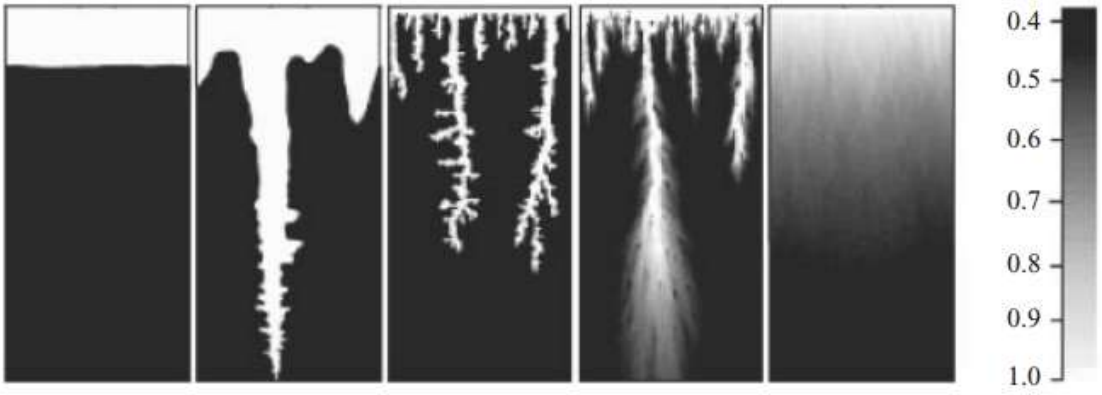

Figure 2.7: Porosity field for acidization simulations using two-scale continuum model from Golfier et al. (2002).

Panga et al. (2005) employed a 2-D two-scale continuum model to simulate the dissolution process. Changes in local permeability are correlated to porosity using a semiempirical formula (Eqn 2.11),

$$\frac{k}{k_0} = \frac{\varepsilon}{\varepsilon_0}\left(\frac{\varepsilon(1-\varepsilon_0)}{\varepsilon_0(1-\varepsilon)}\right)^{2\beta} \quad (2.11)$$

where ε is the porosity, ε_0 is the initial porosity, k_0 is the permeability, and β is a fitted parameter. The model shows good agreement with breakthrough curves for salt packs after calibration with experimental data (Figure 2.8).

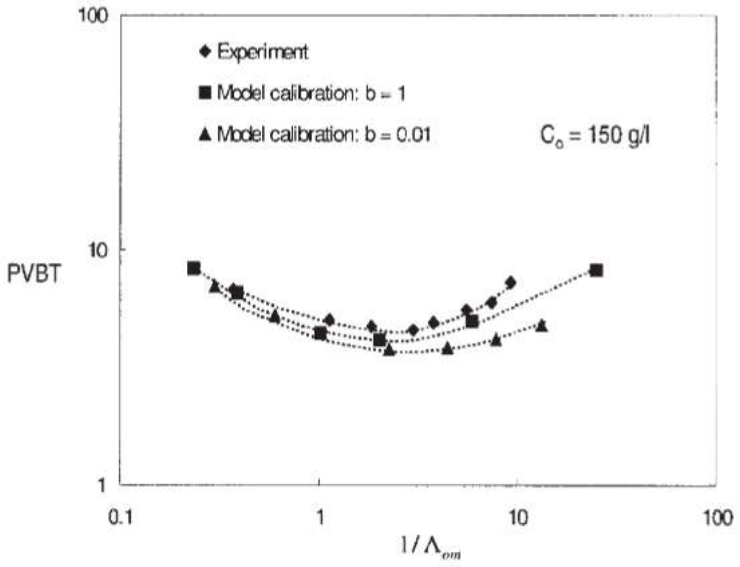

Figure 2.8: Pore volumes to breakthrough versus injection rate normalized by the diffusion coefficient, reaction rate constant, mass transfer coefficient, and reactive surface area. Results for salt-pack experiments and model realizations are shown.

Maheshwari et al. (2013) extended this two-scale continuum model to 3-D. Mesh size was set at 180×72×72 in a rectangular lattice (Figure 2.9). Results show excellent agreement when compared to the limestone-HCl system from Hoefner and Fogler (1988). Variations in simulation heterogeneity reveal that wormhole branching increases with increasing heterogeneity, and that there exists an "optimum" heterogeneity that minimizes breakthrough time.

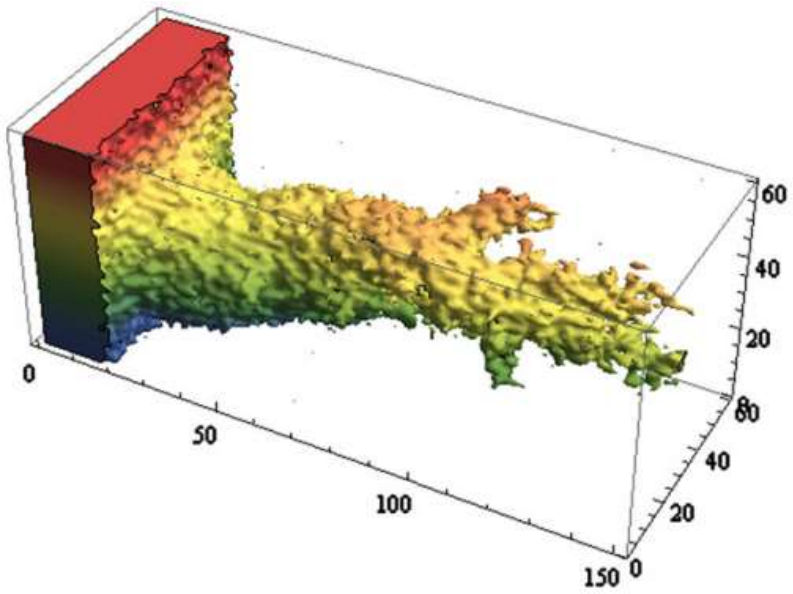

Figure 2.9: 3D 2-scale continuum model employed by Maheshwari et al. (2013). Cells are visualized above a fixed dissolution threshold.

The primary limitation of continuum models is the difficulty in capturing pore-scale heterogeneities. Heterogeneity is introduced artificially as deviation from some mean porosity, rather than reflecting real variations in rock quality. Additionally, Maheshwari et al. (2013) also rely on porosity-permeability correlations from modified Kozeny-Carman relations (Eq 2.12) very similar to Panga et al. (2005) in Eqn 2.10. This approach further homogenizes the simulation under the assumption that all porosity changes translate into a predetermined amount of permeability.

$$\frac{K}{K_0} = \left(\frac{\varepsilon}{\varepsilon_0}\right)^{\gamma} \left(\frac{\varepsilon(1-\varepsilon_0)}{\varepsilon_0(1-\varepsilon)}\right)^{2\beta} \qquad (2.12)$$

The 2-scale continuum model investigated by Pomes et al. (2001) showed high sensitivity in pore volumes to breakthrough to the permeability/porosity relationship chosen. It is also likely that there is not one single permeability/porosity relationship, since nearly all literature acknowledges or shows different permeability is realizations for different injection strategies (Fredd and Fogler, 1998b; Gdanski et al., 1999; Buijse et al., 2005). Lattice Boltzman simulations show a different rate of change in permeability at different injection rates (Kang, 2014). The assumption that all porosity changes translates into a fixed change in permeability is a major limitation of 2-scale continuum models.

Upscaling of laboratory reaction rates to the continuum scale for use in 2-scale models is also problematic in the context of matrix dissolution. Lichtner (2003) found that volume-averaging methods to upscale reaction rate constants for quartz dissolution resulted in effective reaction rate constants that varied as a function of time, which they attributed to heterogeneous distribution of grain sizes.

2.7 PORE SCALE MODELS OF MATRIX DISSOLUTION

2.7.1 Lattice Boltzmann models

The Lattice Boltzmann Method (LBM) has also been applied for modeling the acidizing process. Kang et al. (2002) used the LBM on 2D cross sections of a Brent Triassic Sandstone measuring approximately 0.5mm in length, and assuming a limestone mineralogy for the purposes of simulating matrix dissolution. The Navier-Stokes equation was solved over each voxel, and coupled with a simple transport (advection-

diffusion equation) and reactive model. Dissolution by 0.5M HCl and HF is performed (Figure 2.10). No comparisons with experiments were made; however, the number of pore volumes to breakthrough was significantly closer to typical experiments than most other *a priori* models (Figure 2.11). Optimal injection strategies were obtained, although no clear dissolution regimes were presented.

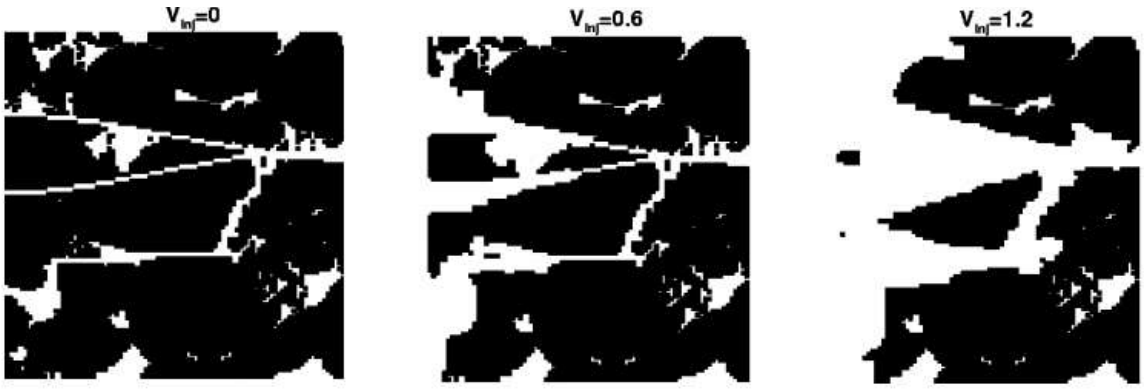

Figure 2.10: Dissolution of calcite from Kang et al. (2002). Figures show formation of a preferential pathway.

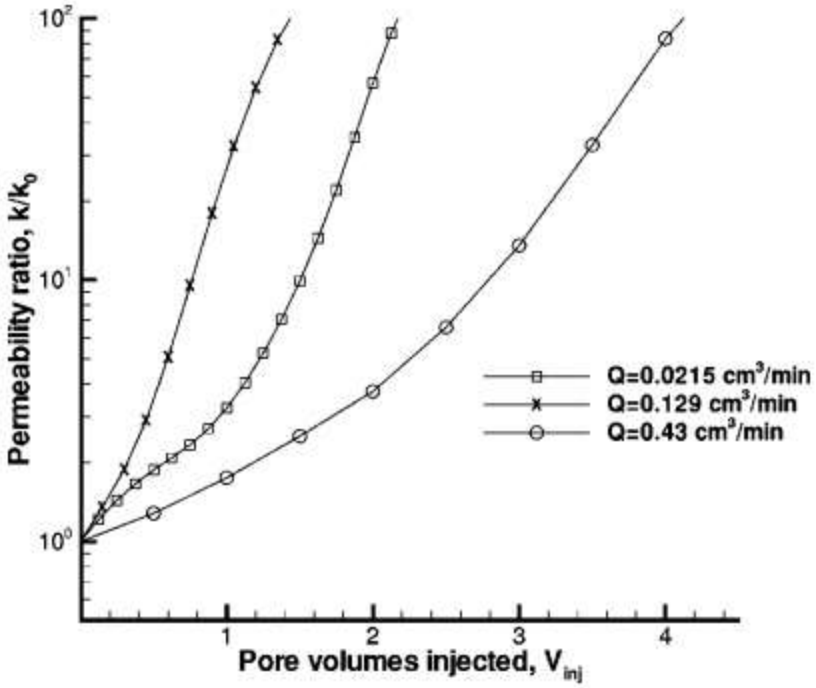

Figure 2.11: Permeability response versus pore volumes injected using 0.5 M HCl.

Szymczak et al. (2009) also employed the LBM to study the evolution of wormhole channels in fracture surfaces textured with randomly placed objects. Experiments on homogeneous fracture planes 99 × 152 mm (essentially 2D) were used to validate the LBM. The characteristic dissolution regimes were reproduced, and optimal injection rates obtained. Mass transfer limited regimes were found to produce the most channeling, although no direct comparison to acidizing experiments was provided. The major drawbacks of LBM are the extremely small (likely unrepresentative) domain size and long computation times. It is not practical to use LBM to simulate dissolution on significant samples of cores ($7 \times 10^5 mm^3$).

Mostaghimi et al. (2016) simulated reactive transport and matrix acidization using the finite volume method, where lattice Boltzmann methods are used to solve the velocity field. Each grid block represents a voxel on a micro-CT image of a sand pack, Berea sandstone, or limestone carbonate. Samples were dissolved at various Péclet and Damköhler numbers using a HF:HCL mixture, and the qualitative dissolution regimes were reproduced (Figure 2.12). The Damköhler number is defined in terms of a reaction rate constant that is not a function of advection. Thus they do not find that channeling occurs at a specific optimal Damköhler number, but rather at a combination of Damköhler and Péclet numbers.

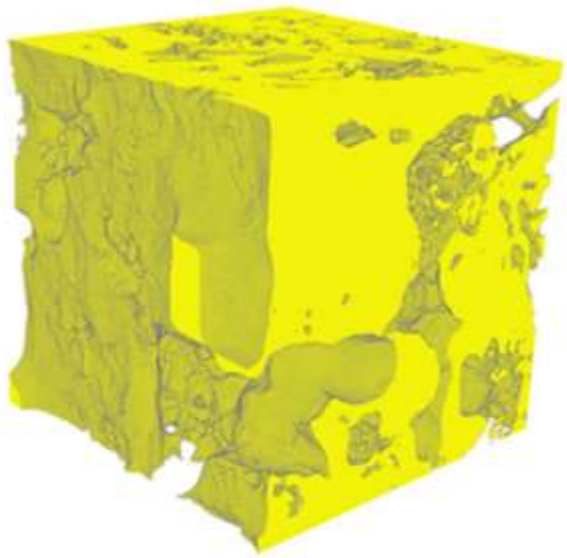

Figure 2.12: Porous structure of limestone carbonate dissolved at Pe = Da = 0.1
(Mostaghimi et al., 2016)

2.7.2 Network models

The first network model of a porous medium was used by Fatt (1956) to study multiphase characteristics of pore space. Pore network models have since been used to

study a variety of complex petrophysical phenomena. Bryant et al. (1993) generated networks from disordered sphere packs that accurately predicted single phase permeability in sandstones. Blunt et al. (2002) present a more modern pore network model to study multiphase permeability and capillary pressure. A 3D representation of the pore space was used in conjunction with a network extraction algorithm to trace a medial axis path through the network, finding local maxima (pores) and minima (throats) (Figure 2.13).

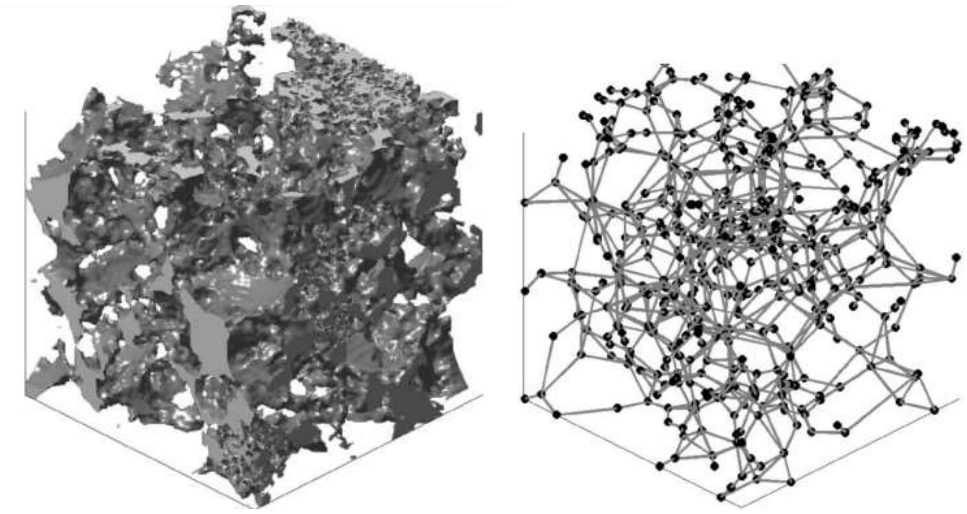

(a) (b)

Figure 2.13: (a) 3D voxel space generated by simulating geological processes, (b) resultant pore network model with pore-nodes shown as black dots, and throats shown as grey lines connecting pores.

Extracting a network from a CT image requires image segmentation and analysis. Qajar and Barns (2016) provide a modern pore-scale imaging technique validated with reactive flow experiments on carbonate rocks. Images are taken before and after

acidization. Greyscale intensity is normalized with respect to the original image. A *t*-test (Urdan, 2005) is used to represent grain space and pore space image intensity values. A non-linear anisotropic diffusion filter is used to reduce sample noise. Greyscale images are segmented into three phases (macropore, intermediate, and grain) using watershed and active contour methods. Intermediate voxels outside one standard deviation of phase intensity are then assigned to pore or grain space. The remaining microporosity is divided into bins and identified as a microporous phase (Figure 2.14). Their technique is primarily used to study evolution of porosity and fines migration, but provides solid guidelines for image segmentation in carbonate rocks.

Figure 2.14: Intermediate microporosity phases used in Qajar and Burns (2016)

While most authors utilize specialized pore-scale physics to study specific problem areas, it is common to begin by solving the single-phase pressure field. Assuming an incompressible fluid, a system of equations can be written over each pore (Eqn 2.13),

$$\sum_j q_{ij} = \sum_j \frac{g_{ij}}{\mu}\left(P_i - P_j\right) = 0 \qquad (2.13)$$

where q_{ij} is the flow between pores numbered i and j, and g_{ij} is the conductivity between them. P_i is the pressure in pore i, P_j is the pressure in the corresponding

neighboring pore, and μ is the viscosity. For the special case in which one assumes the connecting throats are perfect cylinders, the expression for g reduces to the Hagen–Poiseuille relation (Eqn 2.14).

$$g = \frac{\pi R^4}{8\mu L} \qquad (2.14)$$

Flow of non-Newtonain fluids is also possible to simulate in pore network models. Power laws are easily incorporated into pore network simulations. For example, Lopez et al., (2003) model the non-Newtonian behavior of xantham gum using the Cross model (Eqn 2.15),

$$\mu_{eff} = \mu\infty + \frac{\mu_0 - \mu\infty}{1+\left(\lambda\gamma\right)^m} \qquad (2.15)$$

where $\mu\infty$ is the viscosity at high shear rate, μ_0 is the viscosity at low shear rate, and λ and m are fitted constants. They calculate local throat shear rates using simplifying geometric assumptions. Balhoff and Thompson (2008) also model power law fluids using a direct power law model in their pore network simulations.

Afsharpoor et al. (2015) also obtained a pressure equation for viscoelastic fluids for use with pore network models. The pressure term is broken up into viscous and elastic components to form a nonlinear system of equations. The results from the network model are validated with experimental results on bead packs, thus implying suitability for solving for viscoelastic advection in carbonate networks.

Pore network models have also been used to study reactive transport. Li (2005) modeled transport of CO_2 by assuming perfect pore-level mixing and a simple reaction

rate law while solving the advection-diffusion-reaction equation. They observed significant discrepancy between reaction rates predicted by continuum scale models compared to their pore network model. For example, at steady state, the continuum model underestimated kaolinite precipitation by almost two orders of magnitude. The authors attribute this discrepancy to the highly heterogeneous local reaction rates that occur because of non-uniform dispersion of reactant in the network.

Network models have been applied to study matrix acidization. Hoefner and Fogler (1989) used a 2-D network consisting of a regular triangular lattice of 20 × 30 nodes. Hagen-Poiseuille flow is assumed between nodes, with reaction enlarging the connecting throats. The three primary dissolution regimes (face, wormhole, and uniform) are observed (Figure 2.15), but no quantitative experimental comparisons were made.

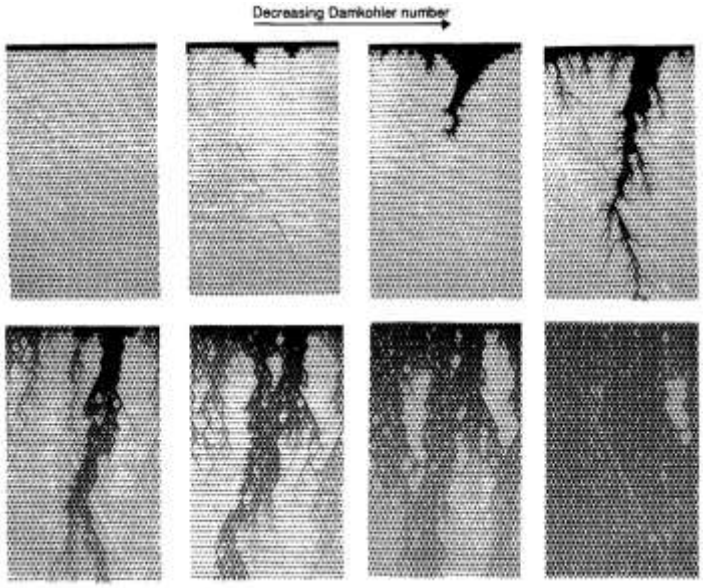

Figure 2.15: Dissolution regimes produced by Hoefner and Fogler (1989) across 3 orders of magnitude change in Damköhler number.

Fredd and Fogler (1998b) presented a 3-D physically representative network model using a packed bed spheres with variable size. Delaunay tessellation of the spheres was used to identify pore centers and throats. Conductivity between pores was calculated numerically using the solution for a hyperbolic Venturi tube. Pore scale mass-transfer was modeled using a Hagen-Poiseuille relationship and Levich's (1962) solution for mass transfer (Eqn 2.16),

$$K_{mt} = 1.86 D_e^{\,2} \left(\frac{u}{dl} \right)^{1/3} \qquad (2.16)$$

where D_e is the effective diffusion coefficient, u is the local velocity, d is the throat diameter, and l is the throat length. The spherical grains were allowed to shrink under dissolution, increasing pore volume. Merging of pores was purportedly facilitated by the fact that grains can completely dissolve, although the network maintained its structure and fixed coordination number, and the dissolved throat continued to provide resistance to flow even when the surrounding matrix is completely dissolved.

Simulations were performed on networks of approximately 3,300 pores and 0.1 cm length. The initial permeability and porosity was reported as 8 Darcies and 40%. They reproduced the expected dissolution regimes (Figure 2.16) and provide breakthrough curves for different fluids which collapse on top of each other when normalized by their macroscopic Damköhler number. However, the simulations overpredicted the optimal injection rate by more than a factor of 10. Additionally, the number of pore volumes to breakthrough in simulations exceeded those found in experiments by about a factor of 40.

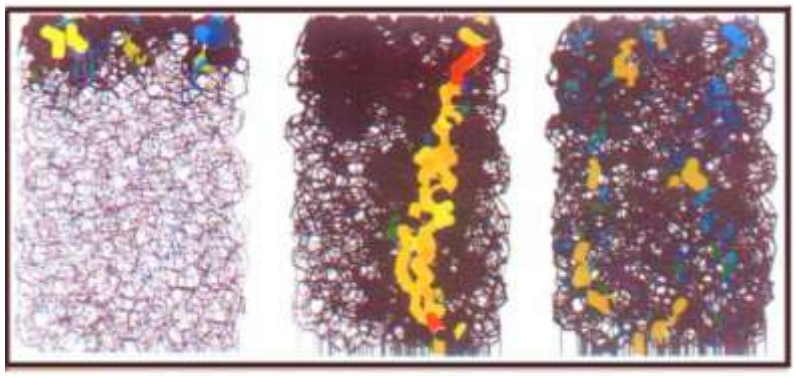

Figure 2.16: Dissolution regimes produced by Fredd and Fogler (1998b) in 3D pore network model

The authors speculated that small domain size and unrealistically permeable networks are major sources of error. Large pore throats were posited to have more mass transfer limitations compared to small throats. Upon reducing the mean particle size by a factor of 10, the optimal Damköhler number improved towards (but still far from) the experimental optimum. The authors concluded that sphere packs are likely to be a poor basis of comparison to heterogeneous and irregular carbonate samples.

A more fundamental issue with the relatively large pore space of sphere packs is the issue of how to define "breakthrough". The authors defined breakthrough as an increase in permeability by a factor of 100, which is arbitrary and does not guarantee a particular dissolution pattern. For the relatively impermeable (0.8 to 2 mD) samples used in the Fredd and Fogler (1998b) experiments, a small wormhole channel may indeed increase permeability by a factor of 100 or more. However, a much larger channel is required to raise permeability from 8 to 800 Darcies in sphere packs. The optimal strategy to reach such a high absolute level of permeability may actually correspond

better to face dissolution, which is commonly thought to be less desirable than sharp, penetrative wormholes.

Other reasons for discrepancy with experiments include the handling of grain dissolution and pore merging. The authors "merged" pores by allowing spherical grains to dissolve and shrink to zero radius. However, all pore-nodes were preserved during simulation, with their conductivities calculated based on the initial tessellation geometry. Therefore, a dissolved portion of the matrix will actually continue to provide significant resistance to flow and result in less channeling. This may explain why the authors did not show any simulated permeability increasing by more than a factor of 80, despite presumably attempting to simulate to their breakthrough criterion of 100.

Budek and Szymczak (2012) modeled network model dissolution and compared the effects of pore merging strategy on the optimal Damköhler number. They found that if pores are forced to stop growing once they touch, they break through slowly and there are several local minimum Damköhler numbers (Figure 2.17). If instead pores are allowed to merge into a single node when they begin to overlap, the number of pore volumes to breakthrough decreases and the curve smooths into the familiar "U" (Figure 1.1a) with a single minimum. This highlights the utility of a pore merging criterion in capturing wormhole formation.

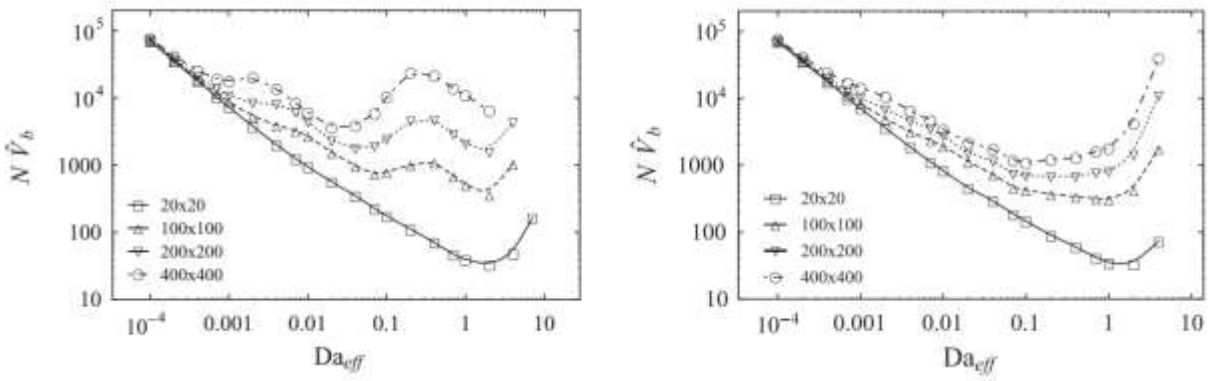

Figure 2.17: Pore volumes to breakthrough ($\hat{V}b$) curve normalized by network dimension (N) produced by Budek and Szymczak (2012). (a) shows results without pore merging, (b) shows results with pore merging.

Finally, many reactive pore network models (Fredd and Fogler, 1998b, Raoof 2012, Li et al (2006), Meile and Tuncay, 2004) relied on a reaction rate or mass transfer coefficient measured in a macroscopic experiment. For example, reaction rate coefficients might be determined from a spinning disc, mixed-flow reactor, or continuous fluidized bed reactor. These results may not be applicable to reaction rates in individual pores, as the smaller scale magnifies the effects of mass transfer resistance and concentration gradients.

2.9 Network Models at Larger Domain Sizes

For most time-dependent applications, networks larger than a few hundred thousand pores are impractical to simulate on a single processor. Larger domain sizes can be reached by using domain decomposition techniques which allow the problem to be parallelized, partitioned, and sent to multiple processors for efficient solution.

Mortar coupling is a domain decomposition technique whereby a large domain can be decomposed into subdomains, using mortar spaces at block interfaces to represent physical variables. Mortar spaces are described by a linear combination of finite element basis functions whose coefficients (Lagrange multipliers) are determined iteratively to ensure physical continuity between adjacent blocks (Bernardi et al., 1994; Arbogast et al., 2000). Wheeler et al. (1999) presented a parallel multidomain approach to Darcy-scale reservoir simulation, where the full domain is decomposed into different regions depending on their local physics (black oil, fracture flow, near-wellbore region, etc.). Computations are performed independently on each block, while 2D mortar spaces placed between blocks enforce mass conservation and flux-matching at the interface (Figure 2.18). Peszynska et al. (2002) provide a practical example, where finer-scale grid blocks are used to simulate the top of a reservoir (above the oil-water-contact), and using coarse-scale grid blocks to simulate the bulk aquifer (Figure 2.19). They demonstrate up to 10% error in well rates if coarser blocks are used universally.

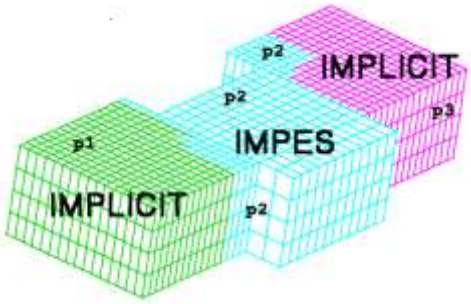

Figure 2.18: Horseshoe shaped reservoir split into 3 subdomains separated by two faults. Subdomains are solved independently using different numerical solvers and different timestepping schema (Wheeler et al., 1999).

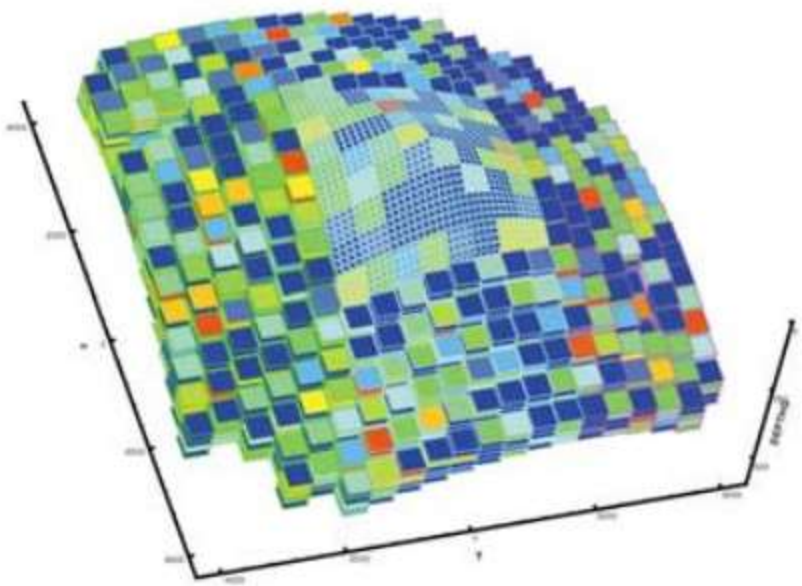

Figure 2.19: Domain decomposition of Khursaniyah field. Fine-scale grid blocks are utilized at the top of the reservoir to provide extra resolution near wellbores. Large scale grid blocks are used below the oil-water-contact.

Arbogast et al. (2007) developed an iterative method for solving the pressure field on a mortar space placed between (and connecting) adjacent subdomains. A brief

algorithm for this process is to first decompose the domain into the desired number of nonoverlapping subdomains. Then, guess values for Lagrange multipliers at the interface (i.e. the pressure boundary conditions for each subdomain). For example, in the case of a 2D domain with a 1D mortar using three nodes to describe pressure (Figure 2.20), the expression is given by Eqn 2.17,

$$p(x) = \alpha_1\phi_1(x) + \alpha_2\phi_2(x) + \alpha_3\phi_3(x) \qquad (2.17)$$

where $p(x)$ describes the pressure field on the mortar face, ϕ_i are the basis functions, and α_i are the Lagrange multipliers. The subdomains can then be solved independently using these boundary conditions. Then fluxes on each side of the mortar are compared and boundary conditions adjusted iteratively until they match within a prescribed tolerance.

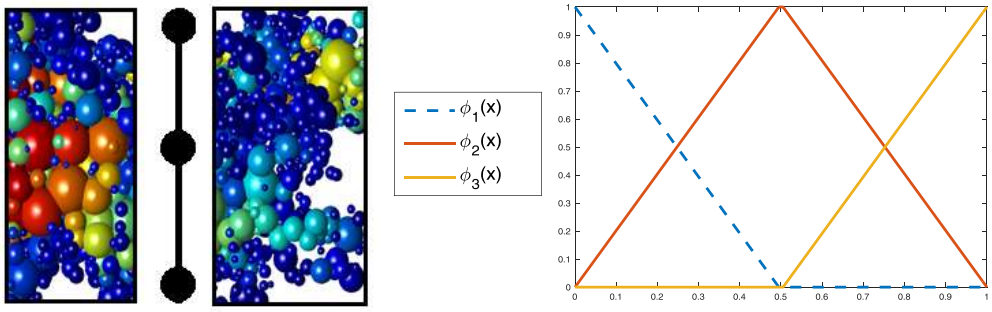

(A) (B)

Figure 2.20: (A) 2D schematic of two network-model subdomains joined at their interface. (B) Example of three linear basis functions $\phi_i(x)$ for each node at the interface.

While Arbogast et al. (2007) developed their mortar coupling technique for continuum problems (e.g. Darcy's law), Balhoff et al. (2008) adapted this method and showed the accuracy of mortar coupling techniques for solving flow fields in network models. Pressure and flux from two copies of a periodic sphere pack (arranged in series) were compared using both a single network and a mortar placed between the two networks (Figure 2.21). Because of the homogeneity of the subdomains, one might expect the mid-point pressure to be well-approximated by 50% of the inlet pressure. However, the pressure field at the interface was shown to deviate significantly from this value, and that the mortar solution was able to capture this accurately (Figure 2.22).

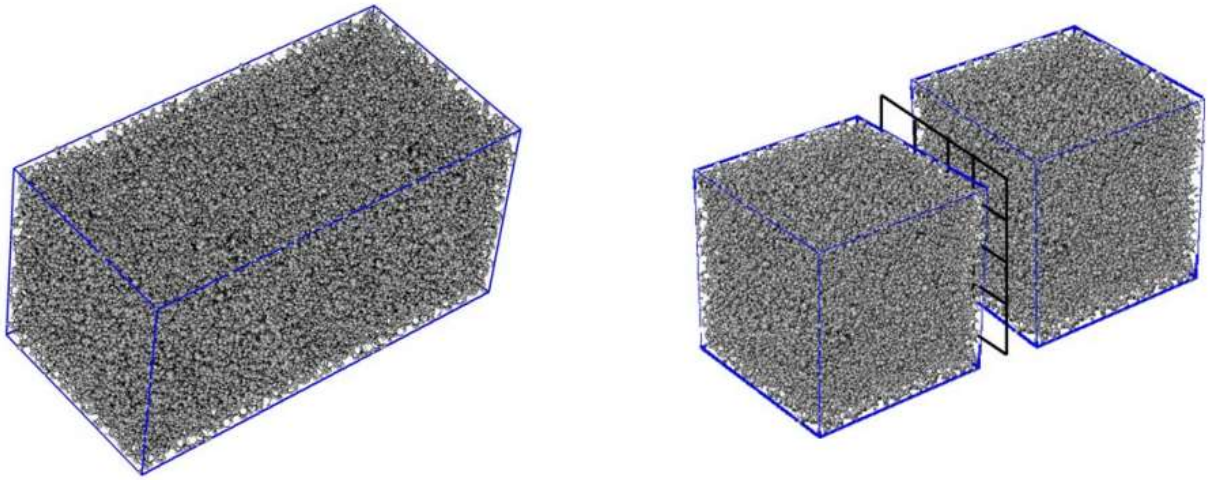

Figure 2.21: Single network solution (left) to be compared with mortar coupled solution (right) from Balhoff et al. (2008).

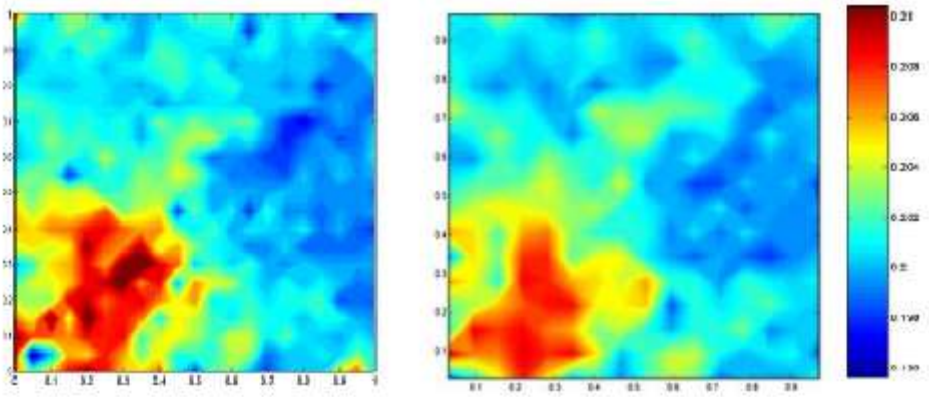

Figure 2.22: Comparison of pressure fields at the mid-point produced by single-domain solution (left) and mortar solution (right).

Mehmani et al. (2012) showed mortars can also be used to accurately model reactive transport in pore networks. Injection of CO_2 is posited to precipitate calcite on the walls of pores during simulation, decreasing their volume and hydraulic conductivity. This has some similarities to the current problem of dissolution of calcite in hydrochloric acid, except in precipitation the permeability decreases with time. Pressure and concentration are shown to match the single-network solution reasonably well during injection of one pore volume worth of fluid (Figure 2.23).

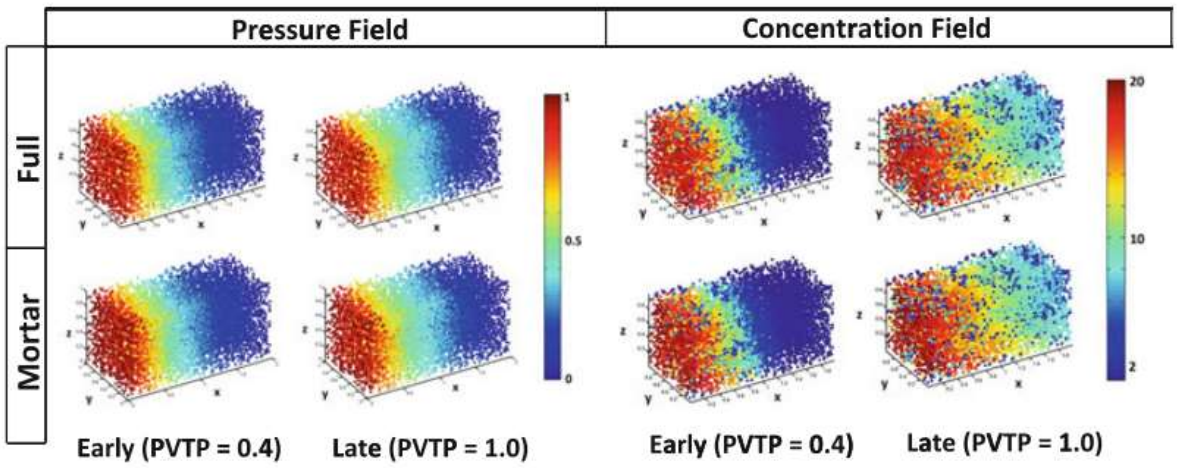

Figure 2.23: Comparison between single network solution (top rows) to mortar solutions (bottom rows) in Mehmani et al., 2012.

While the previous verification exercises have focused on a small number of networks, much larger scale simulations are possible using mortars, especially if parallel computing is used. Mehmani et al. (2012a) used mortar coupling to simulate reactive transport of CO_2 in 64 separate pore networks coupled as one large domain (Figure 2.24). Precipitation of reactants reduced throat sizes and therefore permeability. A variety of precipitation regimes were observed for different injection conditions. Results were demonstrated to be very accurate when compared to non-mortar solutions. Simulations were completed in a single quad core computer, implying that much greater domain sizes can be easily reached using computing clusters. Theoretically, each of these subdomains could be sent to an individual processor to be solved independently, since fluxes at the mortar interfaces are sufficient for iteration of the Lagrange multipliers that compose the interface pressure field. They showed significant improvements using mortars to simulate multiple blocks in parallel compared to in series (Figure 2.25).

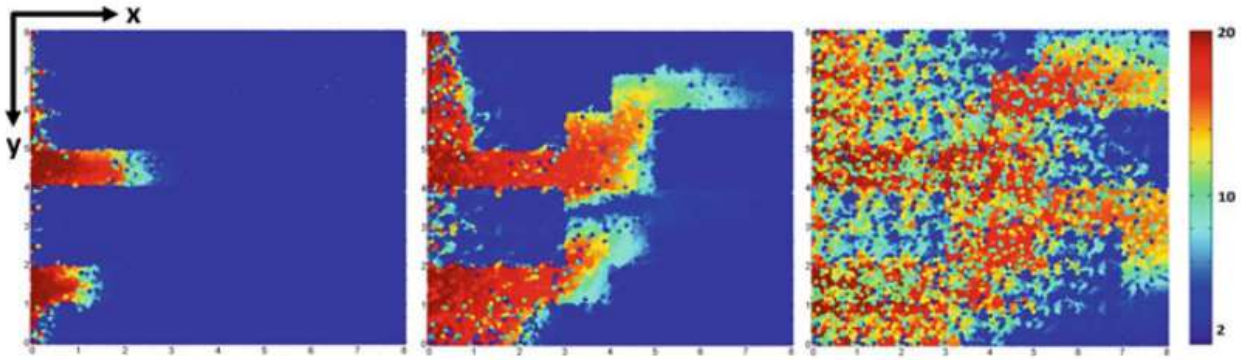

Figure 2.24: Concentration field at various times for 8x8 grid of networks. Network properties are distributed such that two dominant flow paths cut through the domain, although flow diversifies as the dominant flow paths are plugged by calcite precipitation.

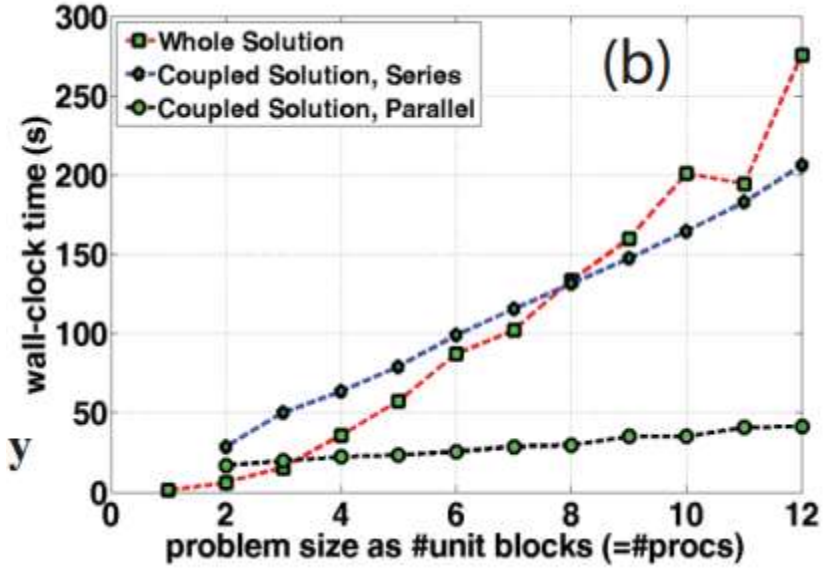

Figure 2.25: Plot of simulation time versus domain size for mortar coupling in series and parallel

2.10 HYBRID MODELING WITH MORTAR COUPLING

Since mortar coupling only requires subdomains to generate fluxes at the interface in order to iterate a pressure solution, pore network models can be coupled to subdomains

whose internal physics are described using entirely different techniques. Balhoff et al. (2008) showed results for coupling of different pore network models and for coupling of pore network models to Darcy scale blocks (represented by a static permeability value) (Figure 2.26).

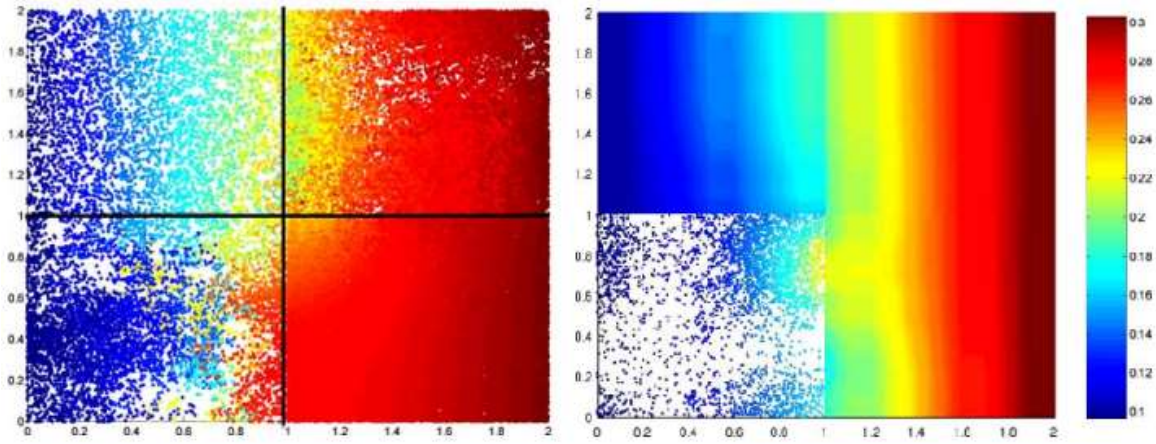

Figure 2.26: Pressure fields for coupling of different pore network models (left) and pore network model coupled to 3 Darcy scale blocks (right).

The previous examples have coupled nonreactive flow in pore network models to continuum scale blocks. Scheibe et al. (2007) performed coupled simulation of reaction/precipitation in porous media, utilizing a smoothed particle hydrodynamic (SPH) model. A continuum porous media approximation was used in nonreactive regions, while a fine-scale direct representation of the pores is used in the central reactive region (Figure 2.27). Tartakovsky et al. (2008) performed a very similar simulation using SPH, this time comparing their hybrid-solution to the full solution conducted at the pore-scale (Figure 2.28), showing the reliability of coarser scale representations of nonreactive regions in porous media.

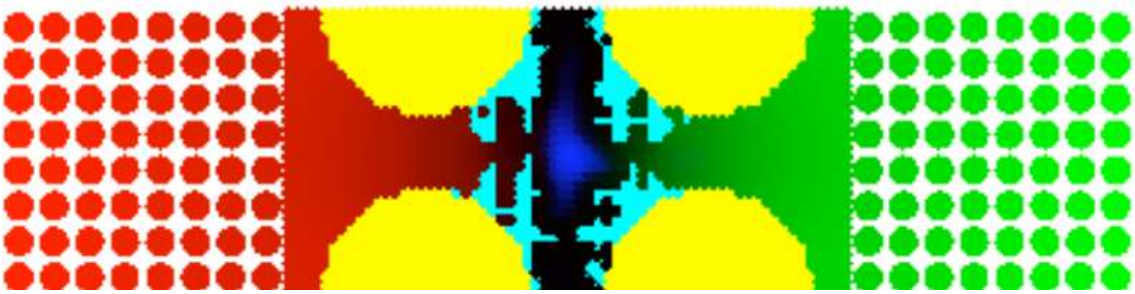

Figure 2.27: Hybrid model presented by Scheibe et al. (2007). Two solutes (red and green) are mixing and precipitating (blue) on the grain surfaces (yellow). The central portion is simulated at the pore scale, whereas the outer regions are simulated at the continuum scale.

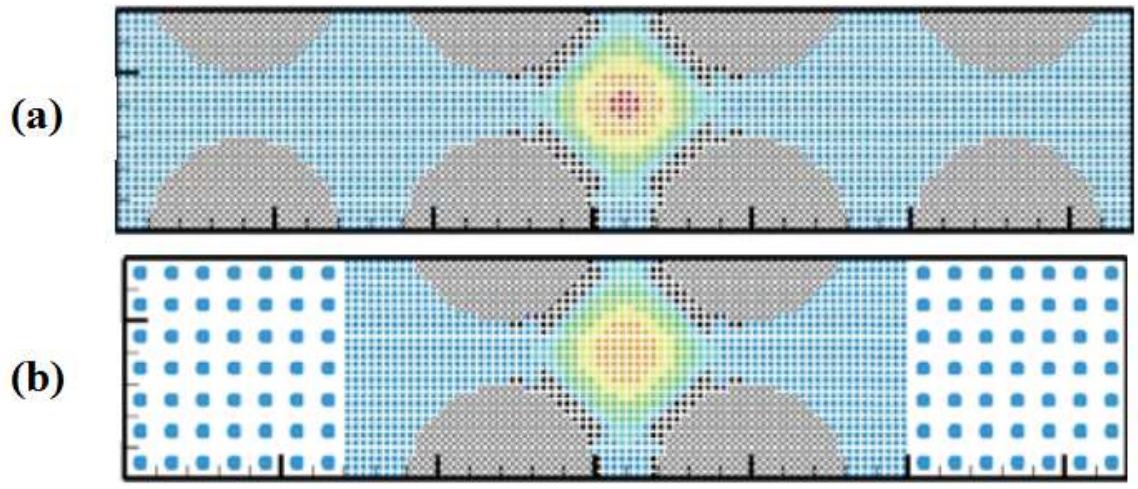

Figure 2.28: Hybrid model presented by Tartakovsky et al. (2008). Precipitation of solute in porous media. Full pore-scale simulation (a), hybrid approach (b).

Building upon this intuitive approach to hybrid modeling, Battiato and Tartakovsky (2011) developed quantitative heuristics for the suitability of domain coarseness for a simple realization of the advection-diffusion-reaction (ADR) equation. Figure 2.29 shows bracketed regions in terms of the Péclet and Damköhler numbers. The

grey regions show where the macroscopic equations for advection-reaction-diffusion hold. In the white regions, coupling with micro-scale models is necessary for accurate solution. For example, on $(-1 \le \alpha < 0)$, diffusion dominates advection and the ADR reduces to a dispersion-reaction equation. The suitability of a continuum scale model then depends upon the relative speed of reaction.

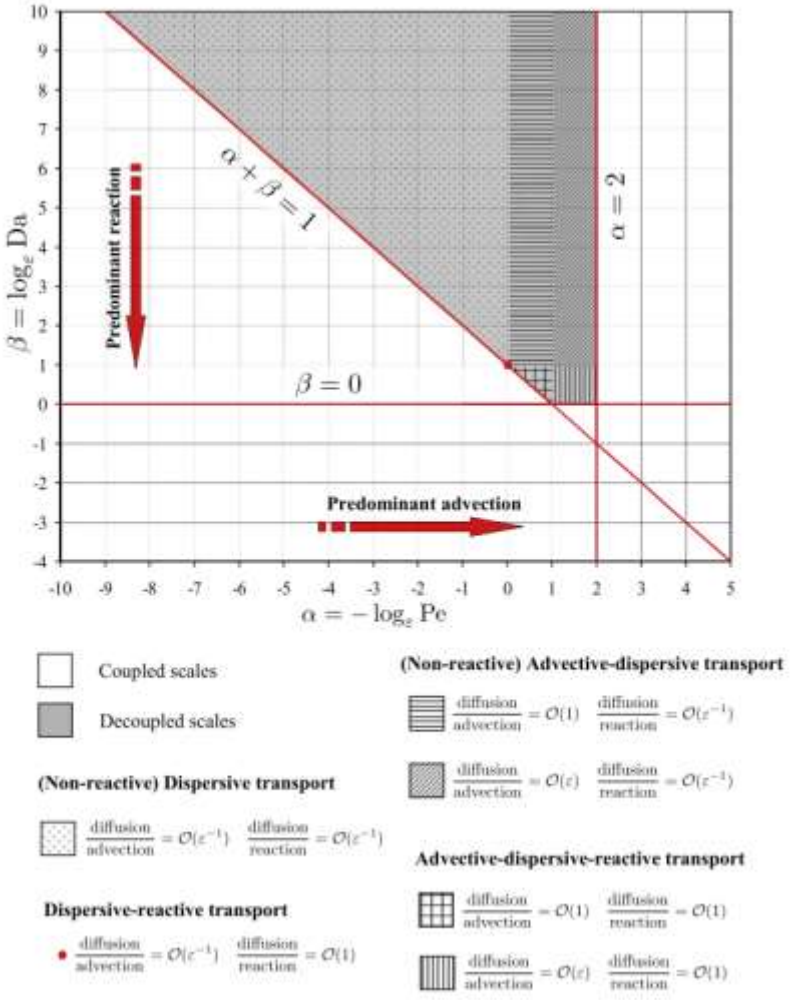

Figure 2.29: Phase diagram representing the suitability of macroscopic-only (decoupled scales, grey) or a hybrid fine-scale model (coupled scales, white) (Battiato and Tartakovsky, 2011)

For the HCl/carbonate systems considered in this thesis, reactant consumption is extremely fast (mass transfer limited), and most advection rates are fast relative to diffusion. Since mass transfer is amplified by advection, the diagonal-hatched region corresponds to matrix dissolution at sufficiently fast injection rates. This implies that pore-scale models of acidization could also be represented at the coarse scale (such as by a two-scale continuum model) for sufficiently high injection rates. Thus, there exists the possibility for a hybrid model for carbonate acidization, whereby pore network models are used to simulate intermediate zones, and continuum scale models are used to describe homogenized regions.

Chapter 3: Pore Network Modeling of Reactive Transport and Dissolution in Porous Media

3.1. INTRODUCTION

This chapter focuses on development of a general pore-scale model of matrix dissolution. The primary goal is to improve on existing network models in order to predict the optimal Damköhler number and reproduce the classical pore-volumes-to-breakthrough (PVBT) curves found in experiments. A novel pore-scale mass transfer coefficient and pore-merging criterion using finite element simulations are developed in COMSOL®. These modules are shown to dramatically improve the predictive capability of networks. The optimal Damköhler number determined from our network simulations closely matches the optimum of 0.29 reported experimentally for mass-transfer dissolution in porous media.

3.2. MODEL DEVELOPMENT

3.2.1. Network Generation

Pore network models can be constructed from idealized representations of media, such as sphere packs, where the exact grain centers and pore dimensions are known analytically. Networks can also be extracted from 3D binary voxel representations of media, commonly available from computed tomography (CT) scans of rock samples.

This work utilizes the network extraction algorithm employed in Thompson et al. (2008). Pore geometry, location, and throat conductivities are quantified for use in transport simulations. A full description of the network extraction technique can be found

This chapter is based primarily on the following work, of which Joseph Tansey is the primary contributor: Tansey, Joseph, and Matthew T. Balhoff. "Pore Network Modeling of Reactive Transport and Dissolution in Porous Media." *Transport in Porous Media*(2016): 1-25

in Sheng (2013). To summarize, a medial axis is traced through the pore space of the medium. The medial axis path is a skeleton of connected lines through the pore space whose segments are equidistant from at least two different points on the object border. A pore is defined as the intersection of three or more paths, and the radius is checked based on the maximum sized voxel-sphere that can be grown before contacting the grain boundaries. A similar dilation method is used to calculate the inscribed radii of pore throats. Throat conductivity is calculated using methods from Patzek and Silin (2001), whereby irregular throat shapes are mapped onto triangular, square, and circular geometries, depending on their shape factors. During simulation, these initial relationships between throat cross-section and conductivity are preserved as a static "shape factor".

3.2.2. Simulation of Flow and Transport

The dissolution process is simulated in five steps. (1) The pore pressure field (and therefore connecting throat flow rates) is computed for the entire network by imposing mass balance at every pore. (2) Using the obtained flow field, species can be advanced via advection and diffusion. (3) Species consumption via heterogeneous surface reaction is modeled using the pore-scale mass transfer coefficient developed herein. (4) A volume of dissolved grain is computed for each pore based on the stoichiometric ratio of the reaction. Pores grow, assuming a static geometry, and throat conductivities are recomputed. (5) Finally, a pore merging criterion determines if pore growth warrants representation of two pores as a single node. This process is repeated until a specified

ratio of permeability increase is obtained, usually corresponding to "breakthrough" (defined in section 3.3.1). The simulation procedure is also outlined in the flowchart in the appendix.

3.2.2.1. Pressure Field

The pressure field is solved by enforcing mass balance over each pore, assuming creeping, single-phase, Newtonian flow. Eqn 3.1 is written for each pore, where q_{ij} is the flow between pores numbered i and j, and g_{ij} is the conductivity between them. P_i is the pressure in pore i, P_j is the pressure in the corresponding neighboring pore, and μ is the viscosity. The sum of all flow in and out of each pore is zero for an incompressible fluid.

$$\sum_j q_{ij} = \sum_j \frac{g_{ij}}{\mu}\left(P_i - P_j\right) = 0. \qquad (3.1)$$

This system of equations is solved to obtain pressure in each pore. In this way, flow rate through each throat can be calculated. Macroscopic flow rate can be measured by summing flux over outlet pores on each boundary, and permeability can be determined by back-calculation using Darcy's law, $q = -KA(P_{inlet} - P_{outlet})/\mu L$,where K is the bulk permeability [L^2], A is the cross-sectional area open to flow, and L is the domain length. The pressure is solved at each timestep due to the widening of pore throats and merging of pores.

3.2.2.2. Species Transport

The pressure field is used to advance species through the network explicitly via the advection-diffusion equation (Eqn 3.2), where V_{pi} is the volume of pore i, c_i is the

concentration in pore i, D_e is the effective diffusivity, a_{ij} is the cross-sectional area of the connecting throat, and l_{ij} is the length of the connecting throat. An operator splitting method is used to solve reaction separately from advection and diffusion. Flux into and out of each pore carries fluid with concentration equal to the upstream concentration. The timestep is constrained to be no larger than the minimum time required to evacuate a single pore for the given pressure profile in accordance with the Courant-Friedrichs-Lewy (CFL) condition. The equation is solved explicitly using this minimum timestep.

$$V_{p_i} \frac{dc_i}{dt} = \sum_i D_e a_{ij} \frac{\Delta c_i}{l_{ij}} - \sum_i c_i q_{ij} . \qquad (3.2)$$

For the purposes of interpore species transport, the concentration in each pore is assumed to be uniform (perfect mixing), and is referred to here as the Mixed Cell Method (MCM). This assumption is regularly employed in reactive transport models (Fredd and Fogler 1998b, Li et al. 2006, Kim et al. 2011). Many authors have recognized the limitations of this assumption and developed alternatives for pore mixing such as streamtube routing (Berkowitz and Naumann, 1994; Stockman et al., 1997; Bijeljic, 2004), the Brownian Particle Tracking Model (BPTM) (Archarya et al., 2007), and attempts to split the streamlines at pores (Bruderer and Bernabe, 2001; Jha et al., 2011; Mehmani et al. 2014). Nonetheless, Archarya et al. (2007) show that dispersivity obtained from MCM and BPTM are equally reliable in pore network models and Mourzenko et al.. (2002) show that MCM is accurate at moderate Peclet numbers for their fractured system. In Mehmani et al. (2014), MCM is shown to have high accuracy in

large 3D networks (>4000 pores) for transverse mixing, where structural mixing dominates over pore level mixing.

Advection's influence on the assumption of perfect mixing is somewhat complicated when transport is reactive. Although beyond the scope of this paper to generate detailed analysis, it is hypothesized that consumption of species dampens the ability of diverging advection streams to produce heterogeneous outlet concentrations, thus further ameliorating the MCM assumption. Therefore, for the purposes of species transport by advection and diffusion, it is argued that the assumption of uniform pore concentration is acceptable for the current application.

3.2.2.3. Species Consumption and Development of Mass Transfer Coefficient

Species consumption is solved explicitly over each pore according to the reaction expression in Eqn 3.3,

$$V_{p_i} \frac{dc_i}{dt} = R(c_i) \qquad (3.3)$$

where $R(c_i)$ is the rate of species consumption in pore i. A heterogeneous reaction is considered that occurs between solute and the solid grain space. Past network models of reactive transport have used much larger-scale experiments to model reaction in individual pores. For example, Li et al. (2006) rely on experiments conducted in a mixed-flow reactor to obtain kinetic parameters. Combined with the assumption that concentration in each pore is uniform, this may be an effective way to model reaction-rate limited regimes. However, in the mass transfer-limited regime, it is implied that the reaction rate is sufficiently fast such that the local rate of diffusion plays a large role.

Assuming uniform species concentration is similar to assuming an infinite mass transfer rate, which is counterproductive towards modeling a mass transfer limited process. Therefore, although uniform species concentration is assumed for the purposes of inter-pore advective and diffusive transport, mass transfer-limited species consumption requires recognition of the intrapore concentration gradient. A specialized mass transfer coefficient is developed to accurately model species spending in the mass transfer-limited regime.

Finite element simulations in COMSOL®, were used to estimate the mass transfer coefficient under the assumption of infinite reactivity at pores walls. The pressure field is determined by solving the Stokes equation (Eqn. 3.4), assuming creeping, incompressible flow. Species transport is solved via the steady-state advection diffusion equation (Eqn. 3.5) assuming dilute species (concentration does not affect diffusion), where P is pressure, μ is fluid viscosity, and u is the velocity. Boundary conditions are defined in Eqs. (3.6)–(3.10) and illustrated in Fig. 2. A uniform inlet concentration (Eqn. 3.8) was used for consistency with our assumption of perfect mixing during advection. This assumption is also employed in derivations for mass transfer coefficients in the mass-transfer limited regime (Levich, 1968; Cussler, 2009), although reaction in upstream pores could affect the concentration profile at the inlet. COMSOL® simulations reveal worst-case error in mass-transfer of approximately 10%. A diffusion coefficient of 3.6×10^{-5} cm^2/sec, and fluid viscosity of 1×10^{-3} Pa-s were used, although all results are presented in dimensionless form.

$$\nabla \cdot [P + \mu(\nabla u + \nabla u')] = 0 \qquad (3.4)$$

$$\nabla \cdot (-D_e \nabla c) + u \cdot \nabla c = 0 \qquad (3.5)$$

$$P_{\text{inlet}} = \text{constant}; \quad 0 - 4000 Pa \qquad (3.6)$$

$$P_{\text{outlet}} = 0 \qquad (3.7)$$

$$c_{\text{inlet}} = 500 mol / m^3 \qquad (3.8)$$

$$c_{\text{outlet}} = 0 \qquad (3.9)$$

$$c_{\text{wall}} = 0 \qquad (3.10)$$

Simplified geometries, based on typical pore dimensions from the extracted networks, were used to generate mass transfer coefficients at different flow rates. Three axisymmetric pore geometries were considered. First, a pore based on the properties of the networks was used (Fig. 3.1). Zero-length throats and a finite cylinder (representing extremely large throats) were also modeled as extreme examples of anisotropy between the pore bodies and throats (Fig. 3.2).

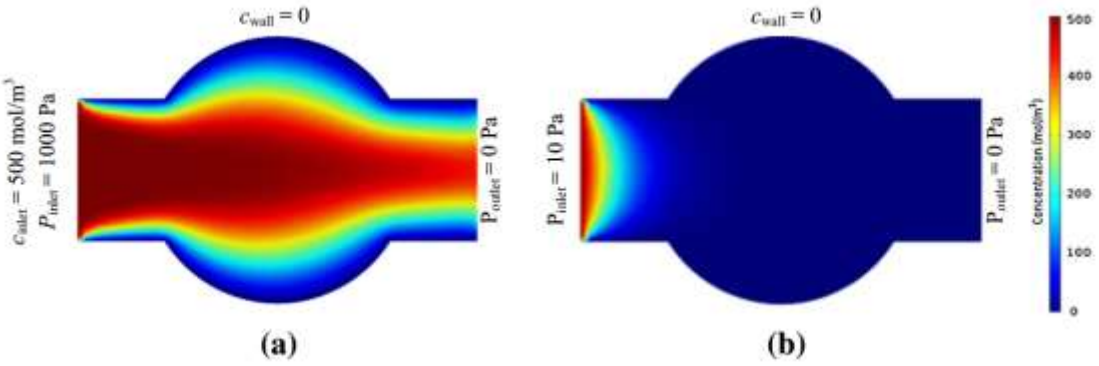

Figure 3.1: Aerial view of 3D COMSOL steady-state simulation for intermediate flow rate (A) and low flow rate (B). Color heat shows species concentration. Fluid is injected from the left inlet and allowed to reach steady state. Reacting species concentration at the faces is set to zero to mimic infinitely fast reaction (mass transfer-limited regime).

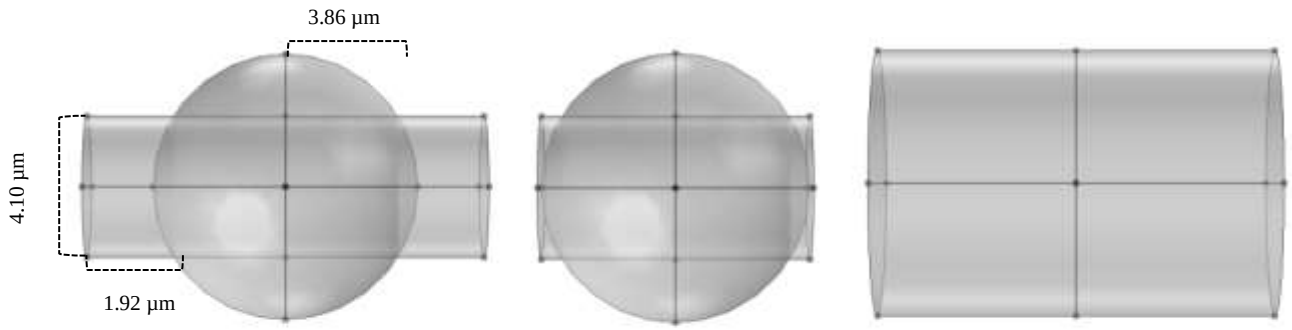

(a) (b) (c)

Figure 3.2: Pore geometries used in determination of pore-scale mass transfer coefficient. The "default" pore (A), based on network properties, is compressed into a spherical shape with zero-length throats (B). A cylindrical case (C) represents pores with extremely large throats.

The mass transfer coefficient (m/s) was back-calculated at each flow rate using the steady state solution and Eqn 3.11, where $\dot{n}$ is the molar flow rate, and SA_{pore} is the surface area of the walls. Δc is the defined as the difference between average pore concentration and wall concentration (zero) because average concentration is produced by the solution to advection-diffusion equations. At each steady state solution, the difference between the inlet and outlet molar flux can be used to compute the rate of molar consumption. Mass transfer relationships are presented as a dimensionless relationship between the Péclet number (Pe, ratio of advection to diffusion, Eqn 3.12) and Sherwood number (Sh, dimensionless mass transfer coefficient, Eqn 3.13) that also accounts for the effect of pore geometry, where L is the characteristic domain length (m).

$$K_{mt} = \frac{\dot{n}}{SA_{pore}\Delta c} \qquad (3.11)$$

$$\mathrm{Pe} = \frac{Lu}{D_e}, \qquad (3.12)$$

$$\mathrm{Sh} = \frac{K_{mt} L}{D_e} \qquad (3.13)$$

Inlet flow rates were varied across the range of pore-level pressure drops observed in network simulations. These span Péclet numbers of between 0 and 3000. At low Péclet numbers (<20), diffusion dominates, and the particular shape of the pore does not seem to have a large effect on mass transfer (Fig. 3.3). As a result, a single linear relationship between the Sherwood and low-end Péclet numbers is applied for all geometries (Eqn 3.14). It should be noted that the vast majority of pore-scale Péclet numbers along the dominant dissolution path tend to be well above this threshold. For example, at the intermediate injection rate of 0.2 mm^3/sec, the average Péclet number in pore throats is approximately 200.

At higher Péclet numbers, the Sherwood number becomes a much stronger function of pore geometry. It behaves logarithmically in the case of a finite cylinder (Eqn 3.15), and almost linearly when the pore is spherical (Eqn 3.16). In the spherical case, the flow field does not contact the diverging pore space, and therefore the rate of mass transfer in the spherical case is much lower due to a structurally thicker boundary layer. Interpolating based on the ratio of throat length to pore diameter provides a good approximation for intermediate cases (Eqn 3.17).

$$Sh = 1.18(Pe) + 0.00054, \quad \text{Pe} < 20, \qquad (3.14)$$

$$Sh = 0.0048(Pe) + 23.95, \quad \text{Pe} > 20, \text{ spherical geometry} \qquad (3.15)$$

$$Sh = 6.60\ln(Pe) + 7.70, \quad \text{Pe} > 20, \text{ cylindrical geometry} \qquad (3.16)$$

$$Sh = \left[\left(1 - \frac{L_{throat}}{2L_{pore}}\right)\left(0.0048\left(Pe\right) + 23.95\right)\right] + \left[\left(\frac{L_{throat}}{2L_{pore}}\right)\left(6.603\ln\left(Pe\right) + 7.691\right)\right],$$

Pe > 20, general geometry (3.17)

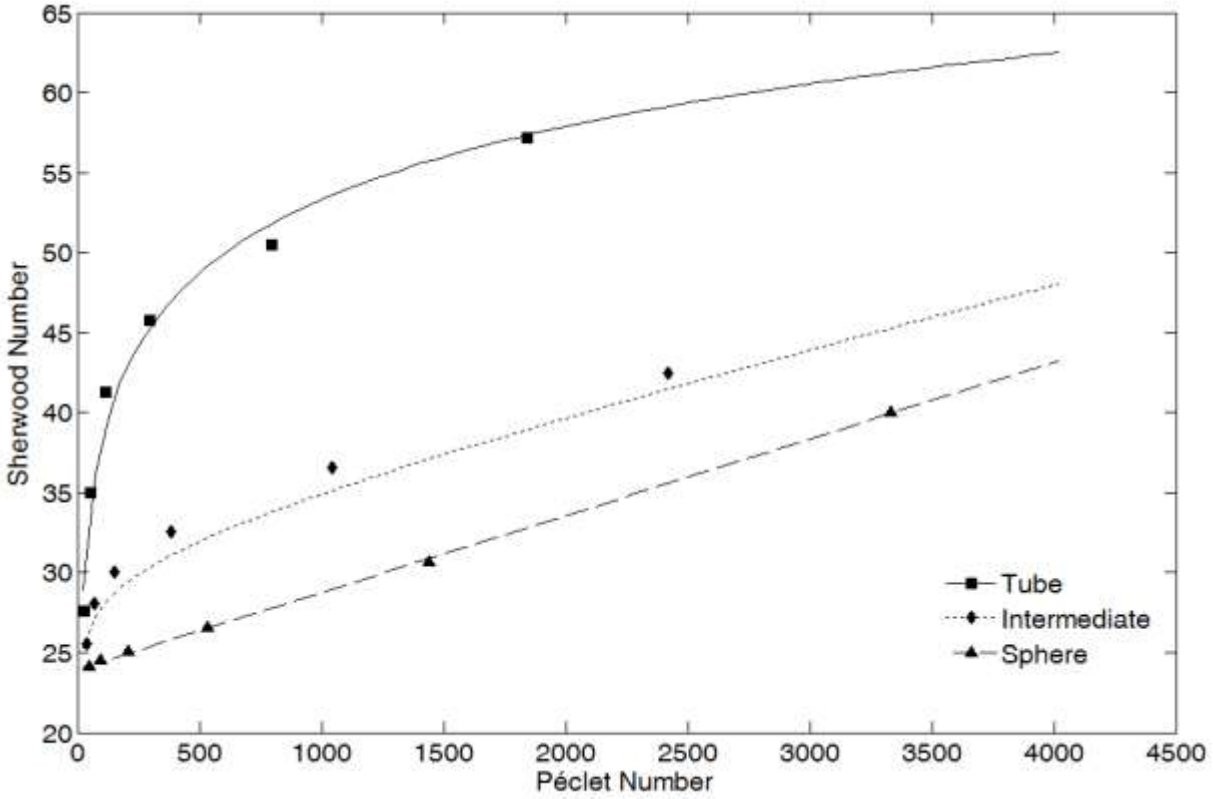

Figure 3.3: Curve fit of Sherwood number from Eqn 18. Data points represent simulation outcomes. The cylindrical tube and spherical cases are fit using a logarithmic and linear relationship, respectively. The median case is found to be well described via interpolation of the two, based on aspect ratio.

Mass and heat transfer coefficient correlations have been developed extensively in the literature for a variety of geometries. In the case of a finite cylinder, a commonly used correlation relates the Sherwood number to the one-third power of flow rate (Levich 1962; Cussler 2009). However, for our cylindrical case, a logarithmic relation was found to better capture the flattening tail at (extremely) high Péclet numbers, where velocity's compression of the boundary layer is the primary mediator of mass transfer increase.

For the noncylindrical cases, reference is made to Wang and Vanka (1995), who studied heat transfer in a converging/diverging duct similar to the prototypical pore geometry studied above. They find that whereas heat transfer is higher around the narrowing structure (throat), it does not contribute significantly to the overall heat transfer coefficient, which remains essentially invariant with flow rate. This supports our own finding that flow rate does not significantly affect mass transfer in the spherical case, although differences in geometry cause throats to play a more significant role in the overall mass (or heat) transfer.

The mass transfer coefficient relations developed above are for a simplified pore geometry with a straight flow path. COMSOL simulations were also performed to test the impact of angled throats on mass transfer. The pore geometry from Fig. 3.2a was modified to rotate the outlet by 90 degrees (Fig. 3.4). Overall mass transfer coefficient was compared to the original case across the range of studied Peclet numbers. Average relative error was found to be 1.47%, reaching a maximum of 5.24% at Pe = 2420. It is therefore concluded that Eqs. 3.15-3.18 are valid for a wide range of throat orientations in network models.

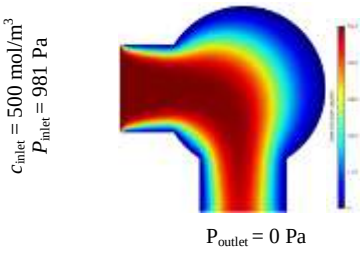

Figure 3.4: Aerial view of 3D COMSOL steady-state simulation for intermediate flow rate, as seen in Fig. 3a. Outlet throat now points downward to capture effect of throat angle on mass transfer. Difference in mass transfer coefficient is 0.56%.

The mass transfer correlations presented here are applied directly to the network model with one additional modification. In Lund et al. (1975), rotating disk experiments show a retardation in hydrochloric acid consumption as a function of steady-state hydrochloric acid concentration. They argue that calcium and chloride ions produced during reaction accumulate at the boundary layer and reduce the effective diffusion coefficient of hydrogen ions. Therefore, rather than using a constant molecular diffusion coefficient of $D_m = 3.6e^{-5}\ \mathrm{cm^2 s^{-1}}$, an expression for the diffusion coefficient (Eqn 3.18),

$$D_e = D_m e^{-(.428\,c)} \qquad (3.18)$$

is taken from the Lund (1975) experiments, where c is the bulk HCl concentration. This modification to the diffusion coefficient is applied at the pore scale in order to retard mass transfer as a function of increasing acid concentration. This is necessary due to the difficulty of developing a rigorous steady-state reaction/precipitation model with accurate multicomponent diffusion in COMSOL.

3.2.2.4. Matrix Dissolution

The rate of molar consumption in each pore is computed using the pore-scale mass transfer coefficient developed below (Eqn 3.19), where SA_{pore} is the surface area of the pore. This is translated into volume of dissolved grain (Eqn 3.20), where M is the molar mass of the grain material, and ρ its density. It is assumed a double displacement reaction (Eqn 3.21). In simulations, a 2:1 ratio of species to matrix moles is utilized to match the reaction between HCl and calcium carbonate (Eqn 3.22). Density of matrix is

assumed 2.71 g/cm^3. The surface area of each pore is computed during the initial network extraction from the number of grain voxels bordering each pore, and a dimensionless parameter referred to here as "compactness" (Ballard, 1982) is utilized to maintain the relation between surface area and volume as the pores grow (Eqn 3.23).

$$R = (K_{mt})(SA_{\text{pore}})(C_{\text{pore}}), \qquad (3.19)$$

$$V_{\text{dissolved}} = \frac{R(x)(dt)(M_{\text{CaCl}})}{2\rho_{\text{CaCl}}}, \qquad (3.20)$$

$$A + B \rightleftarrows C + D \qquad (3.21)$$

$$\text{CaCO}_{3(s)} + 2\text{H}^+ \rightleftarrows \text{Ca}^{2+} + \text{CO}_{2(aq)} + \text{H}_2\text{O}, \qquad (3.22)$$

$$\text{Compactness} = \frac{\left(SA_{\text{pore}}\right)^{1.5}}{V_{\text{pore}}}. \qquad (3.23)$$

This dissolved volume is translated into dissolved surface area using the static compactness ratio. This area is then distributed to each throat's cross-sectional area in proportion to its existing cross-sectional area (Eqn 3.24), where x_{throat} is the individual throat's fraction of total throat cross section for that pore. This allocation strategy is based on the assumption that the pore body dissolves primarily around the throats, a finding strongly supported by Wang and Vanka (1995). Throat conductivities are then updated using the new cross-sectional areas (Eqn 3.25), where *sf* is the shape factor mapping the throat shape onto a cylindrical tube. Since throats connect two pores, and can thus grow from both sides, conductivities are checked to ensure they match from both directions..

$$SA_{throat_{new}} = SA_{throat_{old}} + \Delta SA_{pore} x_{throat}, \qquad (3.24)$$

$$g = \frac{(sf)(SA_{throat}{}^{2})}{8\pi L}. \qquad (3.25)$$

3.2.2.5. Pore Merging Criterion

As pores grow in volume, they will eventually start to overlap. Since the default pore network model approach functions independently of pore location, unlimited pore growth will eventually create one of two nonphysical scenarios. First, pores that have grown to overlap will remain mathematically unconnected. The remedy here is relatively simple. Under the assumption of spherical pores, a new cylindrical throat is created to connect them; the radius of this cylindrical throat is equal to the length of the circular chord formed by the pore intersection. The throat length is equal to the lateral extent of overlap.

The second nonphysical result occurs when two pores that are already connected overlap and eclipse their connected throats (Fig. 3.5). Physically, the resistance is greatly reduced as the pore bodies join. However, the default network approach continues to divert flow through the throat, thereby artificially increasing flow resistance between pores.

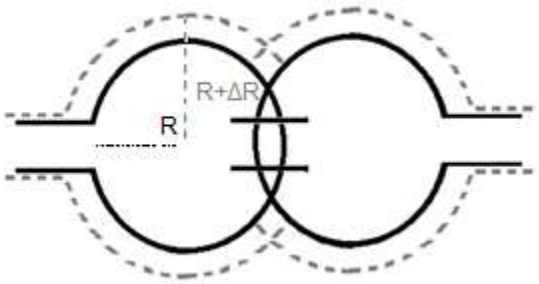

Figure 3.5: In an unspecialized pore network model, the throat continues to provide resistance between two pores regardless of how much they overlap. Physically, the throat is entirely dissolved, and pressure drop between the two pores is minimal. While this figure shows two pores of equal size overlapping, many different pore geometries are considered below.

Past network modeling attempts (Fredd and Fogler 1998b; Budek and Szymczak 2012), have attempted to model pore overlap by forcing pores to stop growing once they touch or reach some critical geometric limit. All pore nodes are preserved during simulation, with their conductivities calculated based on the initial tessellation geometry. Therefore, dissolved portions of the matrix continue to provide significant resistance to flow, and the result is less channeling and permeability response. This may explain why the authors do not show any simulated permeability increase by more than a factor of 80 (Fredd and Fogler 1998b), despite presumably attempting to simulate to their breakthrough criterion of 100. This approach hinders the network's ability to capture advanced stages of dissolution.

In resolution of this problem, it is argued that there is a critical point at which two pores are connected well enough to be modeled as a single pore. COMSOL simulations were run to test this hypothesis. The Stokes equation (Eqn 3.4) was solved using constant inlet flow rate. To represent the "true case" of pores naturally growing and overlapping,

flow through two 3D spherical pores connected by a single throat was considered (Fig. 3.6a). The pores were then grown in diameter using the pore-enlargement strategy outlined in 3.2.2.4., until they overlapped significantly (Figs. 3.6b, 3.6c). For each of these realizations, a "merged" case was also considered, whereby a single larger pore would attempt to represent flow in the "true case" (Fig. 3.8). The single pore's volume is equal to the combined volume of both original pores, with the same inlet and outlet throats. For the same inlet pressure, flow (Q) between these two cases can be compared to obtain the relative error (Eqn 3.26) that comes from "merging" pores in this fashion. The analysis presented here is dimensionless and depends only upon the aspect ratio of the pore throats and bodies and their separation distance.

$$\text{Error} = \frac{\left|Q_{\text{true}} - Q_{\text{merged}}\right|}{Q_{\text{true}}}. \tag{3.26}$$

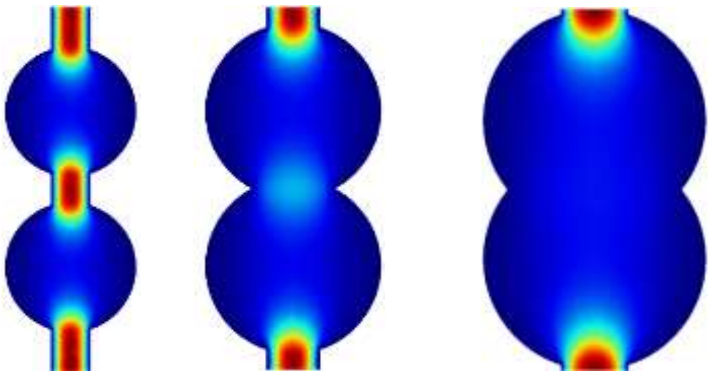

Figure 3.6: COMSOL velocity profiles of two pores growing and overlapping. Case (a) shows the initial idealized case where two pores are separated by a well-defined throat. As the pores grow in cases (b) and (c), the throat becomes engulfed by the pore bodies, and the acute pressure drop between pore centers diminishes. In this figure, equal sized pores are pictured. However, many anisotropic cases were also tested as summarized in Table 1.

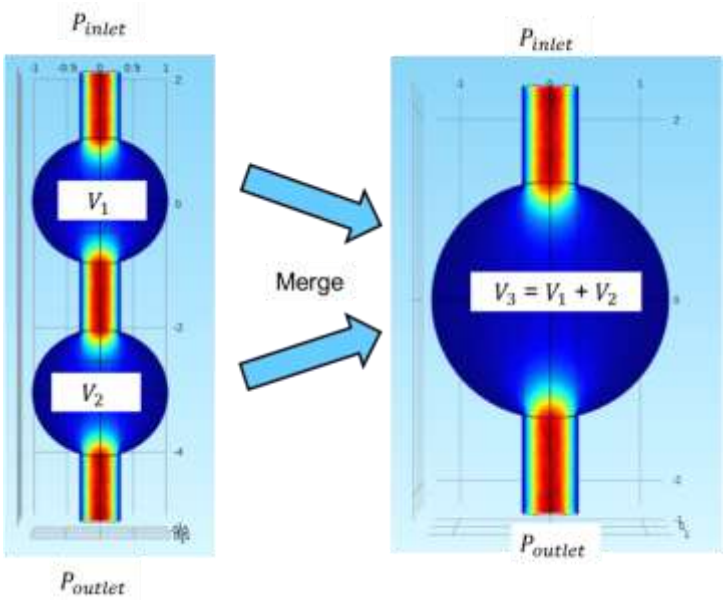

(a) (b)

Figure 3.7: COMSOL simulations comparing flow rates between separate and merged pores. Case (a) shows the flow field for separate pores. Case (b) shows the flow field if the two pores were "merged" by simply adding their volumes together and eliminating the connecting throat. Flow rate between the two cases is compared, the pores in case (a) are increased in size, and the comparison is repeated.

The "true" case (Fig. 3.7a) will always be more accurate than the merged case (Fig. 3.7b). To help supplement our heuristic, the error from the default pore network physics was also quantified in a third configuration, referred herein as the "network approach". In the network approach, the two pores are allowed to grow as in the "true case", but the constricting throat between them is not allowed to dissolve. Flow is always passed through this throat regardless of how much the pores overlap, analogous to pore growth in networks where unlimited pore growth is allowed (but without merging). The network approach is superior to the merged approach when the pores are relatively far apart, because the intermediate throat is still a good approximation when the pores are

just barely overlapping. However, there is a point at which merging the pores becomes more accurate. This is shown graphically in Figure 3.8. Our simulation strategy is to choose the method that has the least error, letting pores remain separate until some critical overlap criterion after which they are merged.

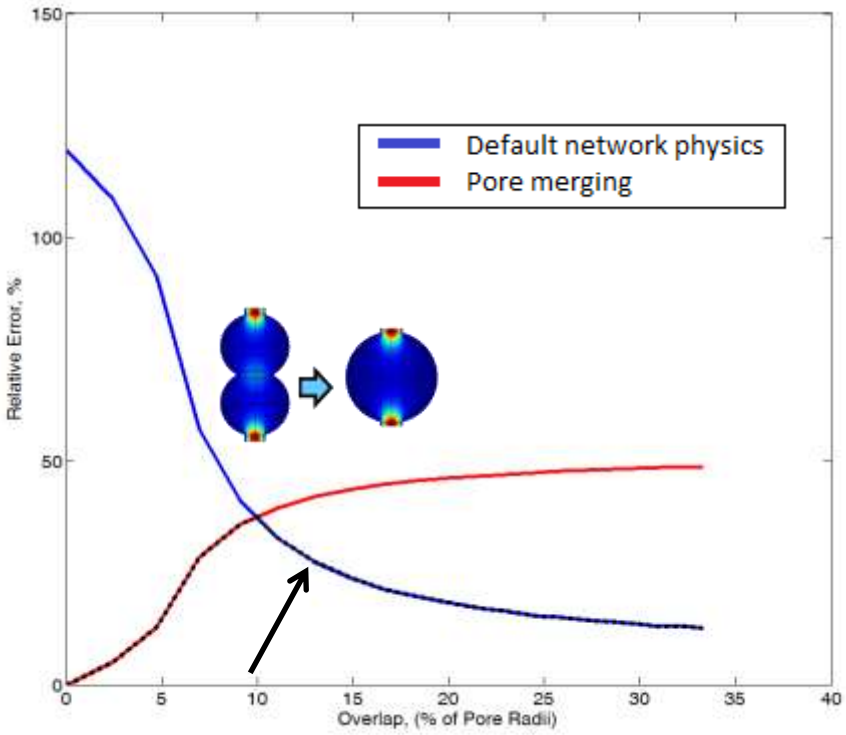

Figure 3.8: Comparison of error between default network physics and merging strategy. As pore overlap increases, the default network approach (red) produces increasingly more error compared to the "true" case. Conversely, the merged case becomes more accurate the more the pores overlap. The point at which the two curves cross is referred to as the "pore merging criterion". Below the pore merging criterion, the default network approach is used. Above this, the merged approach is used. The black dotted line traces this error-minimizing path.

The COMSOL simulations and error figures above are for a specific, simple case in which both pores are the same size and separated by a modest distance. In this case,

the critical overlap percentage is just under 10%. Comparative simulations were run for a wide array of different pore sizes, throat radii, and separation distances. Pores were grown uniformly and compared to the "merged" case and the "network case" such that the optimal merging point could be found. The final dimensions of pores just as merging becomes optimal are summarized in Table 3.1. A simple quadratic relationship (Eqn 3.27) gives a good fit between critical overlap percentages and the aspect ratio between the pore and throat radii, *r*, shown in Fig. 10. When pore throats become very large or very small compared to pore bodies, the criterion may fail, since the equation is a curve fit to simulations. Therefore, aspect ratio, $A = r_{\text{throat}} / \left(r_{\text{pore}_1} + r_{\text{pore}_2} \right)$ is bracketed by the limits simulated (0.025 to 0.168).

$$\text{Normalized Overlap} = 1 - \frac{L_{\text{merge}_{\text{optimal}}}}{r_{p1} + r_{p2}} = 3.27\left(A\right)^2 + 0.18\left(A\right) \qquad (3.27)$$

Table 3.1: Pore sizes and separation distances at optimal merging point.
Units are dimensionless length normalized by sphere radius

Pore 1 Radius (r_{p1}) [Length]	Pore 2 Radius (r_{p2}) [Length]	Throat Radius (r_{throat}) [Length]	Distance Between Pore Centers at Optimal Merging Size (L) [Length]
1.1	1.1	0.33	2
1.65	1.65	0.495	3
2.1	1.35	0.54	3
2.25	2.25	0.675	4
2.05	2.05	0.3075	4
2.75	2	0.8	4.25
2.8	2.8	0.84	5
2.6	2.6	0.39	5
3.35	3.35	1.05	6
3.1	3.1	0.465	6
3.9	3.9	1.17	7
4.45	4.45	1.335	8
4.1	4.1	0.3075	8
4.15	4.15	0.6255	8
4.55	4.55	0.3413	9
5.05	5.05	0.3788	10
5.15	5.15	0.775	10
6.05	6.05	0.4538	12
6.05	6.05	0.3025	12
6.4	6.4	1.495	12
9.65	2.65	0.795	12
6.85	6.85	1.5175	13
7.05	7.05	0.5288	14
7.35	7.35	1.5425	14

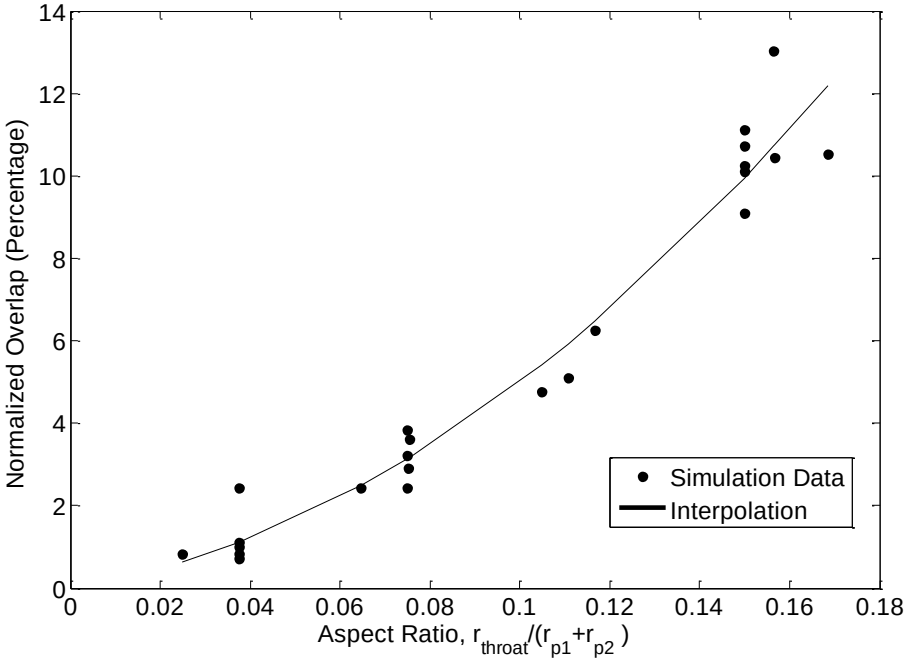

Figure 3.9: Optimal merging points as a function of pore geometries and separation distances as determined from COMSOL simulation. The "baseline" simulation compares pores of equal radius, with throat length equal to this radius, and throat radius equal to 30% of pore radius. Pore radii were varied to differ by up to a factor of 4. Throat radii were decreased down to 10% of pore radius. Separation distance between the pores was varied between zero and double the baseline case. These parameters are compressed into the dimensionless variables in Eqn 3.27.

3.3. Simulation Results and Discussion

3.3.1. Parameters and Definitions

Simulations were conducted on random close-pack arrangements of spheres with equal diameter. Their properties are summarized in Table 3.2. The smaller networks were all taken as subnetworks from the larger 1000-grain network to investigate domain size effects. Differences in permeability are attributable to heterogeneity in the randomness

of packing. All subsequent simulations are conducted on the 1000-grain network unless specified otherwise.

Table 3.2: Summary of Sphere Pack Properties

Grains	Pore Diameter (mm)	Pores	Porosity	Permeability (md)	Domain Length (mm)
100	0.02455	394	0.36	1696	0.22
400	0.02455	1626	0.37	1981	0.34
1000	0.02455	3991	0.38	2270	0.46

Defining "breakthrough" in a rigorous way is difficult. Fredd and Fogler (1998b) define breakthrough as an increase in permeability by a factor of 100, which is subjective and does not guarantee a particular dissolution pattern. For the relatively low-permeability (0.8 to 2 md, 7.9×10^{-12} to 1.97×10^{-12} cm^2) samples used in the Fredd and Fogler (1998b) experiments, a small wormhole channel would likely increase permeability by a factor of 100 or more. However, networks with high initial permeability must experience more advanced dissolution to magnify permeability by 100. Additionally, this definition may not be independent of domain size, as is implicitly assumed. Permeability is dimensional, and may require different levels of dissolution to reach a prescribed ratio for various domain sizes. Fortunately, in the current simulations, the optimal injection rate across a reasonable range of permeability ratios does not change significantly; therefore, a permeability increase of a factor of 10 is used to define "breakthrough".

The Damköhler number for the mass transfer-limited regime (Eqn 2.1) is defined as proposed by Fredd and Fogler (1999) to make a comparison to their experiments.

Likewise, a diffusion coefficient of 3.6×10^{-5} cm^2s^{-1} (HCl in water) is implemented in our simulations and definition of Damköhler number.

3.3.2. Results on 1000-Grain Network

Fifteen weight percent (4.4 M) hydrochloric acid was injected through one face of the domain at various injection rates until the different dissolution regimes were achieved. An aerial view of the simulation for the optimal case is pictured in Fig. 3.10. Initially, the acid is dispersed evenly along the face of the network. However, a strong flow path becomes enlarged and diverts almost all of the acid into it. This wormhole channeling is observed in all networks for intermediate injection rates. Figs. 3.11a and 3.11b show face and uniform dissolution from fast and slow injection, respectively.

An optimal injection rate of 0.2 mm^3/sec was observed, corresponding to an optimal Damköhler number of 0.26. This compares very favorably with the optimal Damköhler number of 0.29 that was found to describe a large range of rock/fluid systems in Fredd and Fogler (1999). The normalized permeability increase is shown in Fig. 3.12 for three characteristic flow rates. Permeability follows the expected trend with pore volumes injected, with an intermediate injection rate breaking through in fewer pore volumes injected. The full breakthrough curve is visualized in Fig. 3.13, with an optimal Damköhler number of 0.26 and 5.7 pore volumes to breakthrough.

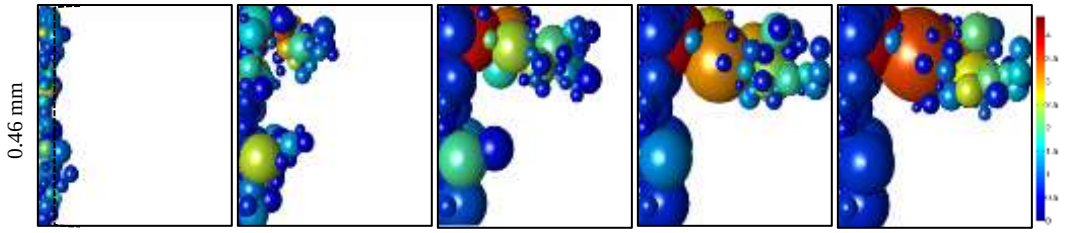

Figure 3.10: Overhead view of simulation progression (from left to right), with increasing pore volumes injected (PVI) at 0.2 mm^3/sec injection rate. Only pores with concentration > 0.5 mol/L are shown. Concentration is represented on a color scale from low (blue) to high (red). Fluid is initially distributed evenly in the pore space, but the acid quickly self-diverts to form a dominant channel that efficiently penetrates the network.

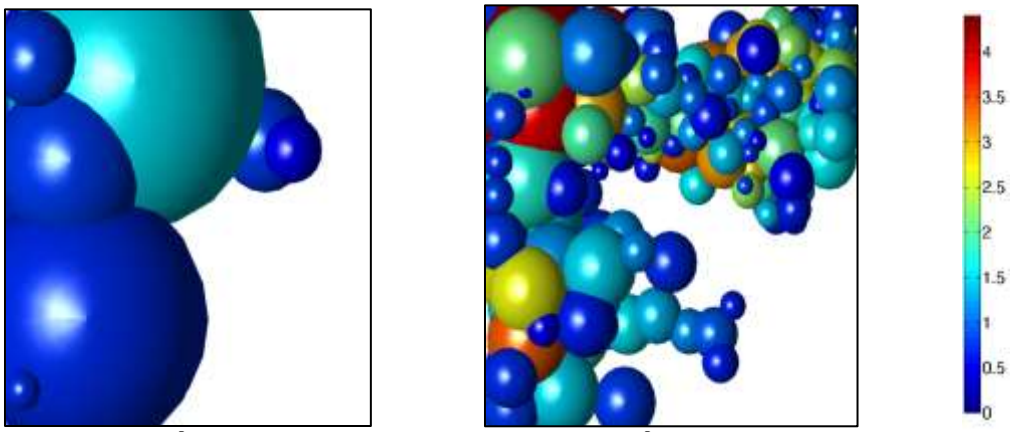

Q = 0.05 mm^3/sec, Da_{mt} = .66, PVI = 12.96 (a)

Q = 1 mm^3/sec, Da_{mt} = .09, PVI = 9.04 (b)

Figure 3.11: Slow injection (a) showing dissolution primarily at the face of the network. Fast injection (b) showing more scattered placement of acid around dominant path compared to the optimal case.

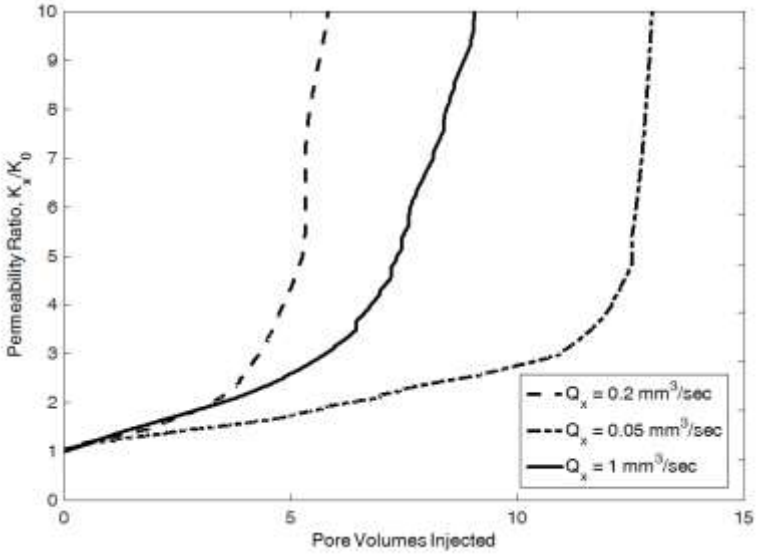

Figure 3.12: Ratio of permeability increase during injection until breakthrough. The leftmost evenly dashed curve shows permeability response during the optimal injection rate of 0.2 mm^3/sec. Inefficient conical dissolution is shown at the far right in staggered dashes at 0.05 mm^3/sec. Ramified wormholes appear at the faster injection rate of 1 mm^3/sec, shown in the middle solid line.

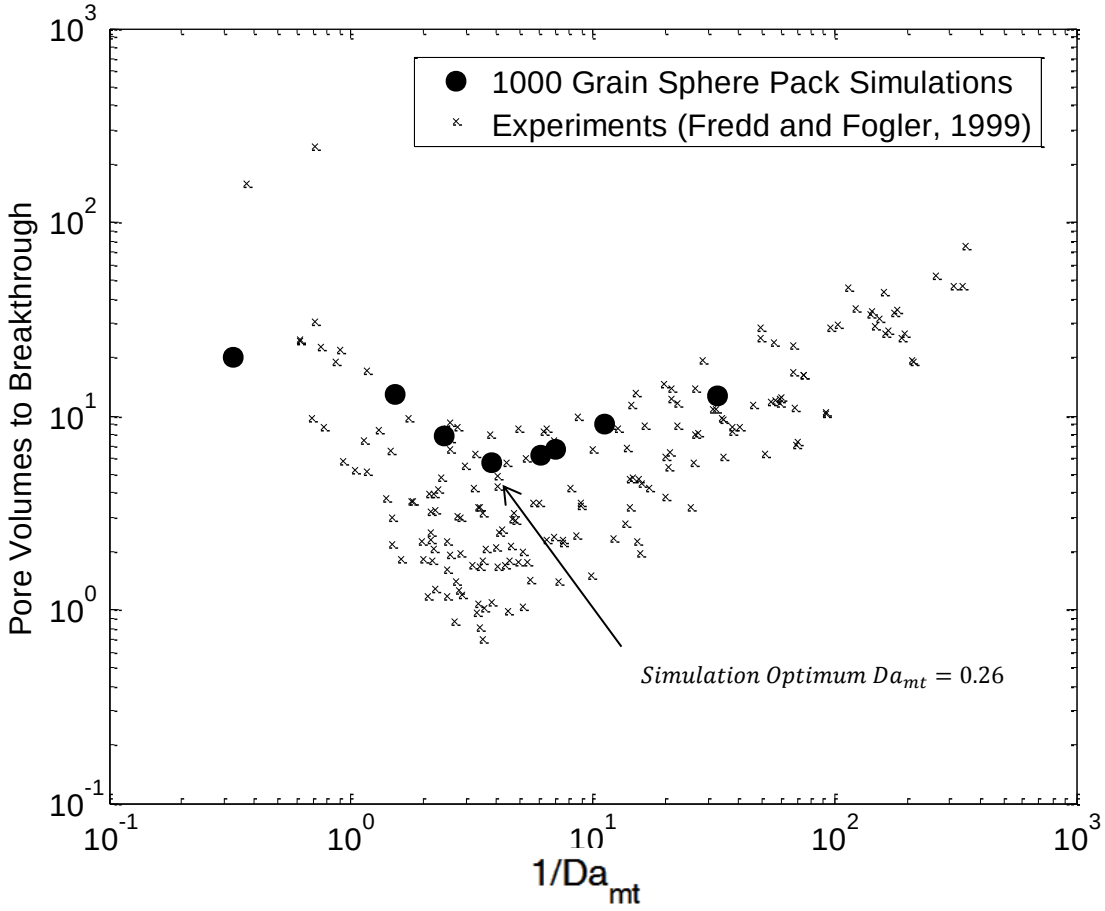

Figure 3.13: Pore volumes to breakthrough for a 1000-grain sphere pack. Simulations illustrate an optimum at $Da_{mt} = 0.26$. Experimental data points from Fredd and Fogler (1999) are an aggregate of many different rock/fluid systems.

For the optimal injection rate of 0.2 mm^3/sec, the final porosity reached 53% with 63% of pores remaining. Mean coordination number (number of bonds per pore) increased modestly from 4.6 to 5.3. Network topology was primarily altered along the dominant flow path, where pores with a coordination number of over 30 developed. The number of pore volumes to breakthrough is, at minimum, 5.7. This is significantly higher than those typically seen in experiments. However, most experiments are conducted on

much more heterogeneous rock samples, and the definition of “breakthrough” is not necessarily consistent with our own. Furthermore, Bazin et al. (2001) found that samples with higher initial permeability require more pore volumes to breakthrough. Experiments typically show a much steeper reduction in breakthrough efficiency at low injection rates (left tail). The small domain size and geometry may at least partially responsible for this effect. Although both simulation and experiments exhibit face dissolution, diffusion-dominated regimes are able to penetrate the smaller domain with consistent effectiveness without much effect from the flow rate.

One other limitation with simulation at low flow rates is that the assumption of uniform pore concentration is equivalent to assuming instantaneous transport of species across the pore node. In other words, the network cannot advance species by a partial pore, and therefore always propagates reactant a certain minimum distance. This leads to an artificial increase in species penetration and reduces the ability of networks to capture face dissolution at low injection rates. This is mathematically equivalent to amplifying the species diffusivity inversely with injection rate.

One possible solution to this problem is to increase the number of nodes that represent the pore space, effectively relaxing the assumption of uniform pore concentration. This approach has the disadvantage of increasing the number of pores (and therefore computation time). It would also require a specialized network extraction algorithm, since common technique is to locate pore nodes at local maxima in the void space. Alternatively, species transport could be deactivated below a certain Péclet number. This approach may also be nonphysical, but rounding dissolution down to zero

may be more accurate than rounding up to the arbitrary minimum imposed by the node spacing.

3.3.3. Model Sensitivity

3.3.3.1. Influence of Pore Merging Criterion

Our current network model largely differs from past descriptions of dissolution in the attempt to physically represent the merging of pores. Naturally, the choice to merge pores and represent them as a single node introduces the potential for large jumps in network conductivity. Although the results of these computational fluid dynamics (CFD) findings have arrived at a criterion that reproduces the optimal Damköhler number, it is worth investigating model sensitivity to this parameter.

First, permeability response is tested when merging is neglected. Instead, pores are allowed to grow until they touch, at which point the pore is flagged as nonreactive. This is analogous to the technique employed by Fredd and Fogler (1998b) in which in dissolved sections of the matrix, "the conductivities of the pore throats are still calculated based on the initial tessellation". The pore merging criterion is shown to be critically important to capturing matrix dissolution (Fig. 3.14). Without pore merging, the matrix's permeability cannot increase past a small fraction of its potential.

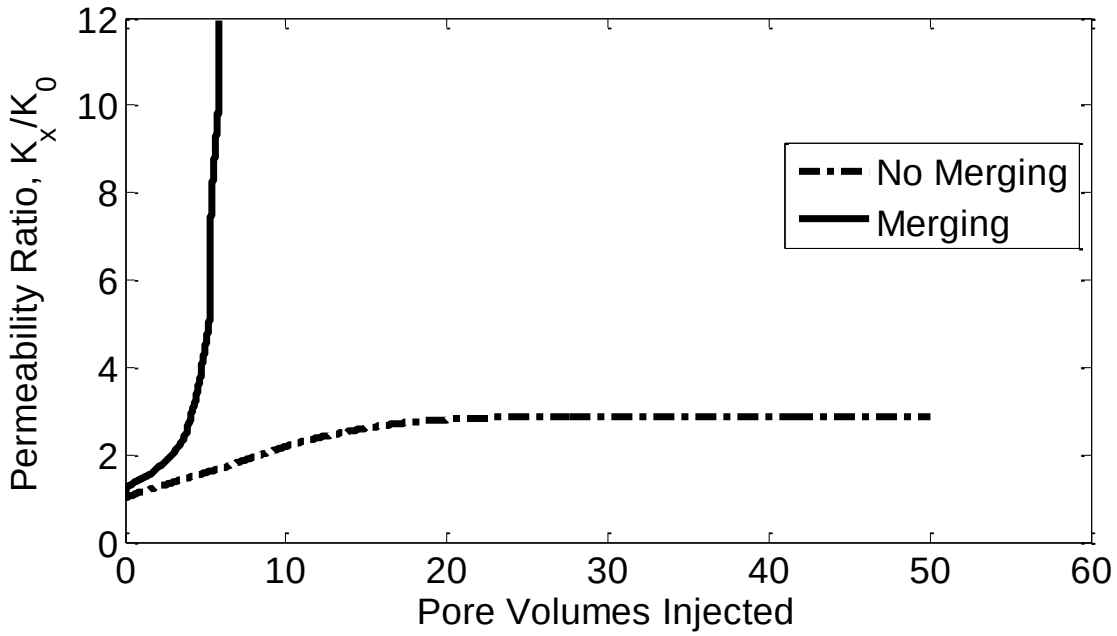

Figure 3.14: Impact of pore merging strategy on permeability increase at optimal injection rate. Without merging, permeability quickly plateaus just under a permeability ratio of 3 regardless of how many pore volumes of acid are injected.

Network models may fall short of describing macroscopic behavior at advanced stages of dissolution. Networks are inherently structured, and dissolution of the pore structure in real rocks often causes the matrix to collapse, a phenomenon for which network models are a poor representation. Additionally, dissolution pathways in experiments (such as wormholes) are many orders of magnitude larger than individual networks. The merging of thousands of pores is unlikely to produce an accurate depiction of void space, since each merging introduces many simplifying assumptions about the merged pore's geometry and location. Even though this approach is more accurate than the default network physics, the pore merging criterion presented herein is not meant to accurately extrapolate ad infinitum.

Therefore, to simulate advanced stages of dissolution (for example, much larger domain sizes) alternative physics ought to be implemented past a certain stage of dissolution. One possible solution is to take a union of highly dissolved space, assume it is essentially void, and construct a new network of much larger pores to replace it. Of course, as dissolution progresses, this region too will suffer the same limited ability to advance its own dissolution, but this re-initialization could theoretically continue indefinitely. This step could be considered a second type of "merging" that would allow networks to capture complete dissolution at any domain size.

Next, the effect of different pore merging criteria on prediction of optimal injection rate and pore volumes to breakthrough is examined. Merging aggressively at half the critical overlap length does not affect the simulation much (Fig. 3.15). The number of pore volumes to breakthrough increases slightly (5.6 vs. 5.7), although the optimal Damköhler number shifts less favorably to 0.14. Merging conservatively at double the amount of overlap results in extremely slow breakthrough (not pictured). Simulations very seldom achieved breakthrough, since the pores are allowed to overlap significantly without merging. This addition of nonphysical volume to the network allows for a degenerate amount of dissolution to occur at the inlet without advancing species into the network. It should be recognized that pore merging only makes sense in the context of overlapping pore space, and therefore cannot be used liberally as a history matching tool.

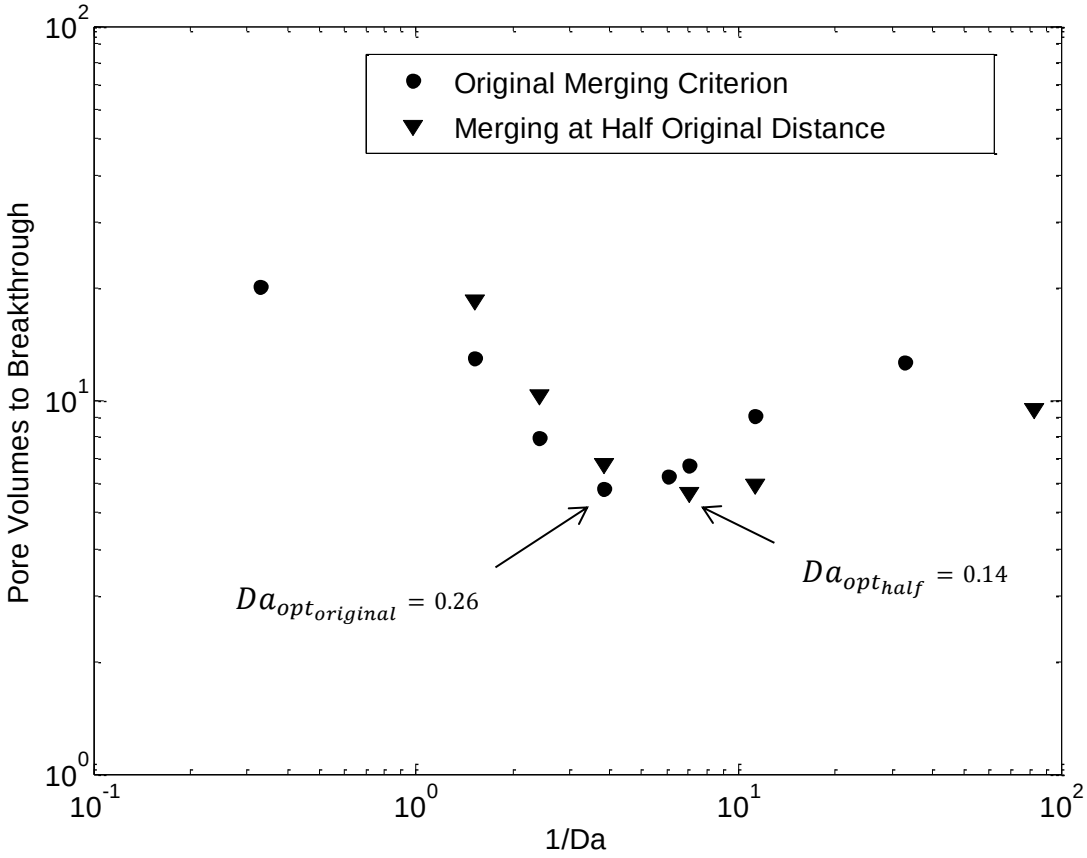

Figure 3.15: Merging criterion's influence on pore volumes to breakthrough. Merging quickly (at half the overlap length produced by our merging criterion) affects the optimal Damköhler number modestly. Merging slowly at double the overlap length (not pictured) allows pores to overlap in a way that adds excessive nonphysical volume to the network.

3.3.3.2 Influence of Mass Transfer Coefficient

The mass transfer correlation (Eqn 3.17) was used as an interpolation of two idealized cases. As can be seen in Fig. 3.5, the interpolation does not exactly match the intermediate data points. To test model sensitivity to this decision, simulations in the 1000 grain sphere pack were rerun at the optimal injection rate of 0.2 mm^3/sec. The mass

transfer coefficient correlation (Eqn 3.17) was replaced with a low and upper bound (Eqs. 3.15, 3.16 respectively), which respectively correspond to a 20% decrease and 50% increase in mass transfer at a Péclet number of 1000. Pore volumes to breakthrough increased to 6.7 in both cases, indicating small sensitivity to the mass transfer relation. Optimal injection rate was not significantly affected.

3.3.3.3 Influence of Domain Size

It was originally speculated by Fredd and Fogler (1998b) that typical network simulations were below the representative elementary volume (REV) of wormholing. To test this hypothesis, the three random close-pack arrangements of 100, 400, and 1000 grains described in Table 3.2 were investigated. Simulations were carried out across a range of injection rates such that an optimal injection rate could be found.

The number of pore volumes to breakthrough is compared in Fig. 3.16. Although the curves do not collapse on top of one another, the minimum pore volumes to breakthrough were 7.6, 5.0, and 5.8 (in ascending order of grains). This suggests that the simulation results are not significantly impacted by domain size, and the slight shifting of the curves can be explained by small changes in network properties and randomness introduced by the pore merging step.

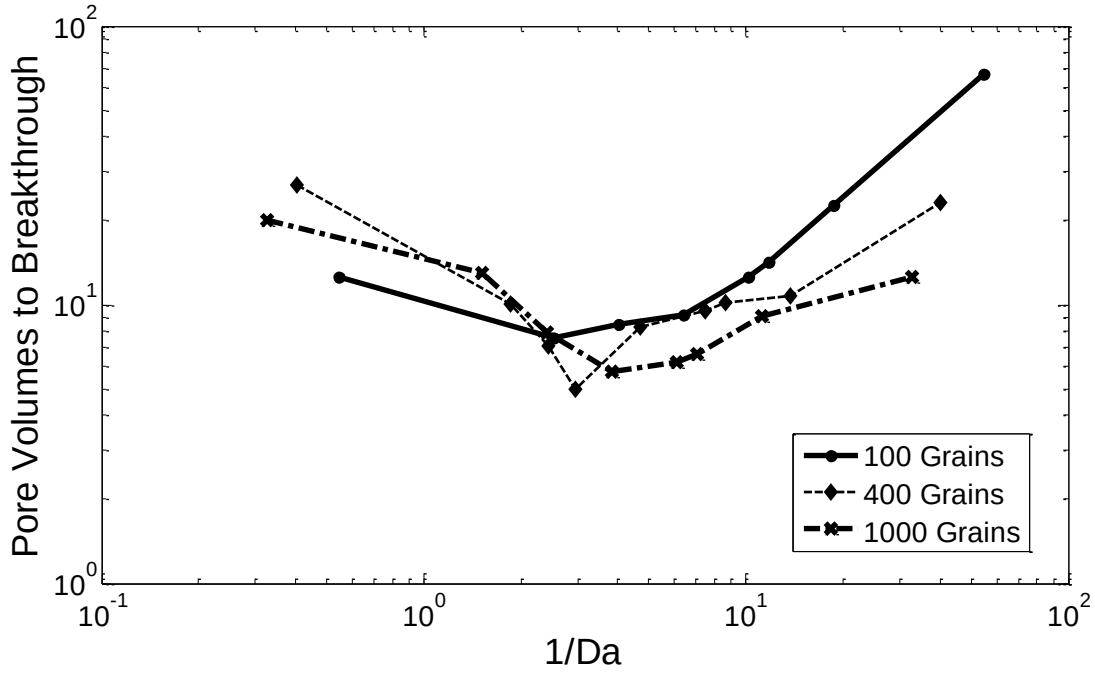

Figure 3.16: Comparison of breakthrough curves for networks of different sizes. Although there is some perturbation of the optimal injection rate and the number of pore volumes to breakthrough, all curves exhibit approximately the same behavior.

The networks investigated here are all on the order of 1 mm, much smaller than the diameter of most mature core-scale wormholes. Therefore, it is possible that different trends could emerge with much larger domain sizes that approach those seen at core or field scales. However, given the model's consistent generation of Damköhler numbers near the experimentally optimum value of 0.29, the most likely change is a reduction in the number of pore volumes to breakthrough. As domain size increases, the relative volumetric proportion of wormhole/channeling may decrease.

Direct upscaling of macroscopic parameters from pore network models can be challenging given, in part, the small domain size. The core-scale experiments studied in

Fredd and Fogler (1999) purported to show a universal optimum Damköhler number of 0.29. This work's Damköhler numbers obtained from sphere packs appear to closely match this constant, despite being several orders of magnitude smaller than typical rock cores. Core-scale permeability is moderately well-predicted by pore network models (Dong and Blunt, 2009) (Okabe and Blunt, 2005). Sheng et al. (2011) constructed networks from microCT images of a sandstone, showing excellent agreement with experimental permeability and porosity above 3mm domain length. For reactive transport, Li et al. (2006) observe that there is no simple way to accurately upscale results from either pore network models or experiments to the reservoir scale. They proposed that pore-scale models could produce valid reaction rates as a function of local heterogeneity during larger scale simulation.

It is prohibitive to simulate dissolution of more than a few thousand pores on a single processor. Coupling hundreds of pore-networks together using mortar coupling techniques might allow for simulation at larger scales (Sun et al., 2012). Mortar coupling is a domain decomposition technique that uses finite element spaces to ensure that variable fluxes match weakly across interfaces (Arbogast et al. 2000). The problem can be solved efficiently in a parallel computing environment (Mehmani et al. 2012). Using mortars to couple many networks together to reach the size of a core could theoretically allow a direct comparison of a large number of pore network models with experiments.

3.4. DISCUSSION

The two primary innovations in this chapter are the pore-scale mass transfer coefficient, and the pore merging algorithm. The pore-scale mass transfer coefficient is very similar to ones utilized in previous pore network models of acidization (Fredd and Fogler, 1998b; Budek and Szymczak 2012). Sensitivity analysis showed this to be extremely robust, as large variations in the expression did not change simulations results dramatically.

The pore merging algorithm is the most important module in the chapter. Without it, pores either grow indefinitely and overlap in a non-physical way, or pores are forced to stop growing (Fredd and Fogler, 1998b) and continue to provide artificial resistance to flow. Pore merging is necessary to capture the self-reinforcing nature of wormholing in matrix acidizing, as the pore space naturally dissolves completely along the dominant flow path, diverting acid from less-conductive regions.

Domain size is found to be mostly irrelevant, at least for small-scale simulations. However, there is still ample room to investigate emergent phenomena at significantly larger domain sizes. The effect of domain size is the primary impetus for chapter 5.

While simulations return an optimal Damköhler number close to the expected value (Da_{mt} = 0.26 vs. 0.29), the predictive value of network models is still unclear. First, it is unclear whether pore network models can predict variation within the optimal Damköhler number for specific rock types, rather than merely returning a static value that happens to be close to the average (Figure 3.13). Second, the number of pore volumes to breakthrough is significantly lower than seen in most experiments. This could be due to

the use of relatively homogeneous sphere packs, which may exhibit less channeling than heterogeneous carbonates. Chapter 4 tests the modules developed in this chapter on networks constructed from real carbonate rocks, and makes comparison with the appropriate core-scale experiments.

Chapter 4: Pore Network Modeling of Matrix Acidizing in Carbonate Cores

4.1. INTRODUCTION

In this chapter, the modeling techniques developed in chapter 3 are used to investigate dissolution of networks constructed from computerized tomography (CT) scans of real carbonate rocks. Networks from five rock types are dissolved at varying Damköhler numbers in order to obtain optimal injection conditions and full pore-volumes-to-breakthrough curves. Results are compared with experimental values obtained on 1" × 6" cores of the corresponding rock type. Comparisons against core acidization experiments find that the pore network model adequately captures matrix acidization, predicting an optimal Damköhler number close to the experimentally-observed values. Additionally, emulsified acid (a shear-thinning non-Newtonian fluid) is simulated using a power law relationship for the flow rheology. Fluid diversion is found to play a minimal role in the improved efficiency of power law fluids. Instead, the dynamic effect of viscosity on local mass transfer is able to account for experimental observations of insensitivity to injection rate.

4.2. OVERVIEW OF EXPERIMENTS

Basic petrophysical properties of each rock type are displayed in Table 4.1. All cores were approximately the same size (2.2 inches length, 1.5 inch diameter). Air

permeability for samples ranged between 8.83 and 668 mD. Helium porosity measurements ranged between 10.4 and 31.6.

Table 4.1: Summary of basic petrophysical properties for each rock type

Rock Type	Length (cm)	Diameter (mm)	Grain Density (g/cm3)	Helium Porosity (%)	Air Permeability (mD)	Klinkenberg Permeability (mD)
Pink Desert	5.67	3.7	2.71	30.4	122	119
Indiana L.S.	5.714	3.8	2.69	14.6	668	661
Edwards White	5.73	3.7	2.71	31.6	8.83	8.11
Edwards Yellow	5.706	3.7	2.63	10.4	52.5	50.5
Austin Chalk	5.623	3.8	2.71	26.2	19.4	18.3

Acidization experiments were conducted on a set of larger carbonate cores (6 inch length, 1.5 inch diameter) by Schlumberger. Pink Desert, Indiana Limestone, Edwards Yellow, Edwards White, and Austin Chalk, are studied here for comparison with network simulations. For four of the five rock types, 15 wt. % HCl was injected on one face of the domain at various rates in order to determine the optimal injection rate (Figure 4.1). Core acidizing experiments were unavailable for the Austin Chalk. All experiments confirm an optimal Damköhler number close to the value (0.29) reported by Fredd and Fogler (1999). Most values fall between $Da_{mt} = 0.2$ and 0.4.

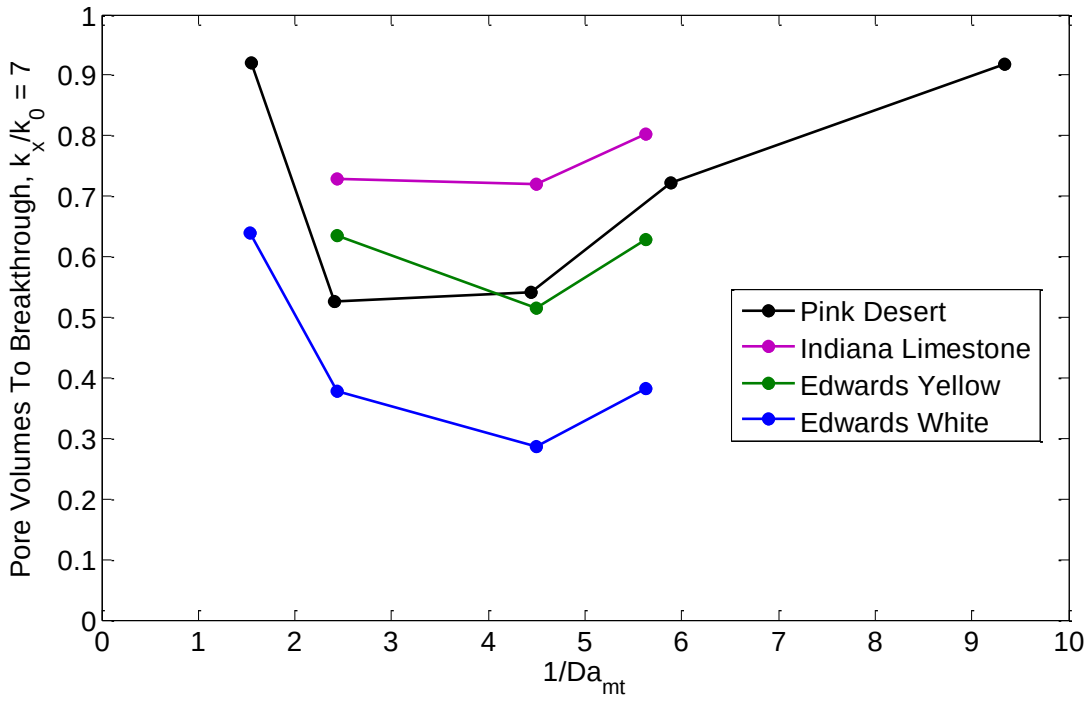

Figure 4.1: Experimentally obtained pore volumes to breakthrough for studied rock types using 15 wt. % HCl (Schlumberger, unsolicited communication)

Experiments on the five rock types using the same core dimensions and acid strength with emulsified acid were also conducted by Zakaria et al. (2015). The non-Newtonian emulsified acid's viscosity, μ, was found to be well-described using a power law relation (Eqn 2.4) with consistency index k =98.13 gm/cm-s^{n-2} and shear-thinning index n= 0.641. The definition of the Damköhler number (Eqn 2.2) cannot be rigorously applied to emulsified acid, since the exact value of the diffusion coefficient is ambiguous (discussed in Section 4.3.3). However, it remains a useful way to normalize length scales between experiments and network simulations.

Compared to the Newtonian acid, the emulsified acid is significantly less sensitive to injection rate (Figure 4.2). This insensitivity to injection rate is common in emulsified acids (Bazin and Abdulahad, 1999; Sayed et al., 2012). Additionally, the number of pore volumes to breakthrough for emulsified acid is lower at every injection rate. The optimal injection rate is also slightly decreased, although still very close to the Newtonian case.

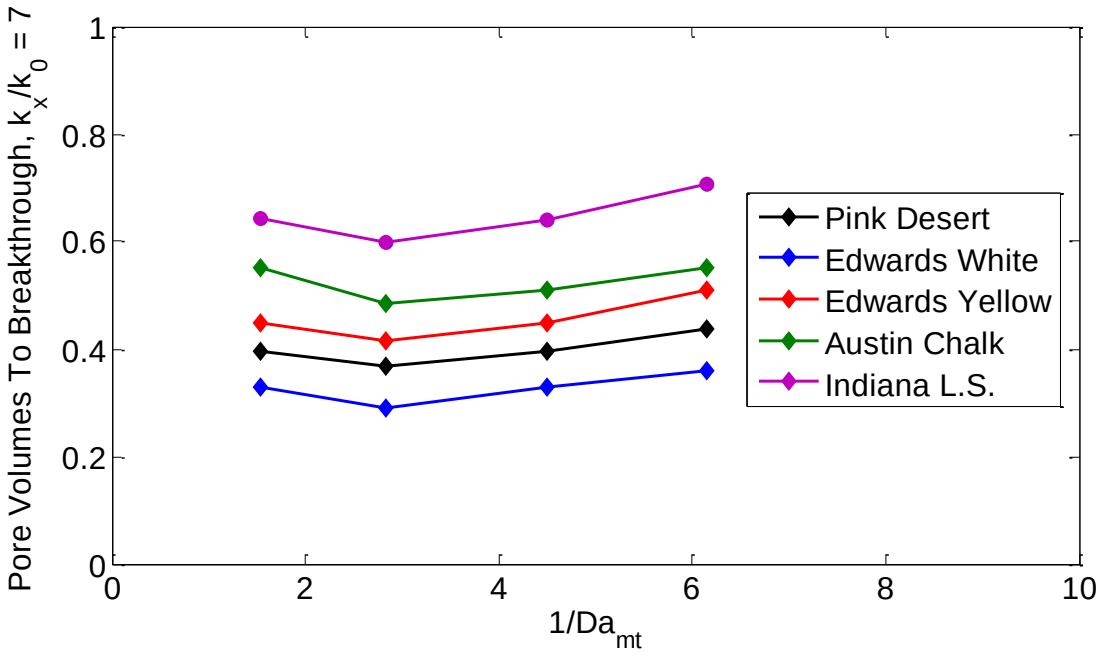

Figure 4.2: Experimentally obtained pore volumes to breakthrough curves for emulsified acid on different rock types (Zakaria et al. 2015).

For the non-reactive tracers, a polymer solution was mixed to match the viscosity-shear rate behavior of emulsified acid. The tracer tests show that effluent concentration lags below unity compared to the Newtonian tracers (Figure 4.3). This trailing phenomenon is sometimes identified as “capacitance”, although it is noted by authors Zakaria et al. (2015) that the Newtonian tracers exhibit no capacitance and therefore no

dead-end pores. Salter and Mohanty (1982a) observe similar tailing in two-phase flow tracer experiments. A capacitance-dispersion model was shown to match experiments well, conceptually dividing the pore space into flowing, dendritic (dead-end pores), and isolated fractions. The authors observe that multi-phase flow can create dead end flow paths and isolated pockets via phase flowpath morphology. Therefore, in absence of an obvious explanation, it is hypothesized that differences in tracer tests between Newtonian and power law fluids are attributable to increased proportion of dendritic flow space induced by the shear-thinning fluid. Unfortunately, the Péclet number in the both the Newtonian and emulsified tracer tests, defined as $(Lu)/D_e$, is at least over 3000 (depending on the value of diffusion coefficient used). This suggests either that the tracer tests are unlikely to be explained via capacitance effects, or that diffusion in non-Newtonian fluids is much more significant at the pore scale than can be inferred from macroscopic experiments.

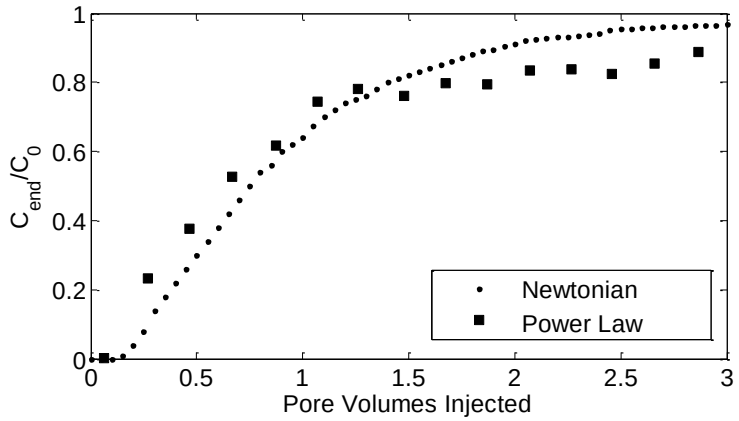

Figure 4.3: Experimentally obtained tracer test for Pink Desert carbonate core, Newtonian (Schlumberger, unsolicited communication) and power law (Zakaria et al., 2015) tracer. Q_{inject} = 5 ml/min for both experiments.

4.3. MODEL DEVELOPMENT

A physically-representative pore-network model is used to qualitatively study and quantitatively predict matrix acidization in carbonates using water-based (Newtonian) and emulsified (power-law) hydrochloric acid.

4.3.1. Network Properties

CT scans from different rock types were performed by Schlumberger (Figure 4.4A). Scans are approximately cubic of 2.2-2.4 micron voxel resolution and 1-12 mm^3 in bulk volume. Pore networks were extracted utilizing the algorithm described in Section 3.2.1. The resultant network for the Pink Desert carbonate is shown in Figure 4.4B. The remaining rock types are shown in the appendix: Pore network models of carbonate rocks.

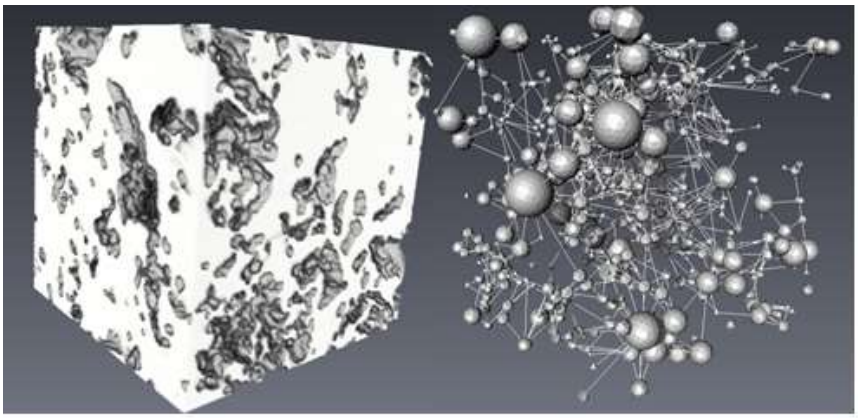

(A) (B)

Figure 4.4: Binary voxel space of Pink Desert carbonate (A). Network extracted from voxel space (B)

First, networks are extracted from all CT scans. Permeability matches reasonably well for the Pink Desert and Indiana Limestone networks (Table 4.2). The high Edwards White network permeability is plausibly explained by selection bias (omitting non-conductive portions of the CT scan), however the Edwards Yellow and Austin Chalk network permeabilities are much higher than seen in experiments, from which it can only be concluded that the CT scans are below a representative elementary volume.

Table 4.2: Comparison of core experiment and extracted network properties. * Indicates network was taken from the corner of a larger CT scan

Rock Type	Experimental Porosity	Experimental Permeability (mD)	Network Length (mm)	Network Porosity	Network Permeability (mD)
Pink Desert	30.4	119	1.15	23.0	144
Indiana L.S.	14.6	661	2.30	9.53	591
Edwards White*	31.6	8.11	1.15	22.6	15.7
Edwards Yellow	10.4	50.5	2.30	22.9	119
Austin Chalk*	26.2	18.3	1.50	20.0	139

However, the Edwards White network (and CT scan pore space) were found unconnected. A corner of the domain (1/2 length, $1/8^{th}$ volume) was found to be connected, and used in the simulations. This corner has much higher permeability than the core scale sample, which is expected given that unconnected volume was excluded from the network. Additionally, a corner of the Austin Chalk was also used in simulation (1/2 length, $1/8^{th}$ volume), because the original Austin Chalk contained a large number of pores (>100,000) and was computationally inefficient for a simulations on a single processor. Permeability was overpredicted for the Austin Chalk by approximately an

order of magnitude, suggesting that the sample was substantially unrepresentative of the macroscopic core.

Porosity is systematically underpredicted in networks, however network porosity nearly exactly matches CT scan porosity (binary voxel space). This implies that the CT scans are either not representative of the rock type, or that microporosity represents a large portion of the "missing" pore space. However, since acidization preferentially enlarges dominant flow paths, the omission of the smallest channels is not likely to affect acidization simulations.

4.3.2. Newtonian Matrix Acidization Model

Mathematical development of the reactive transport network model is summarized in Chapter 3, and in Tansey and Balhoff, (2016). The simulation approach can be broken down into 5 steps: (1) Solve pressure field to obtain flow between each pore, (2) Advance species via advection and diffusion, (3) Simulate reaction in each pore, (4) Grow pores and throats in response to reaction, and (5) merge pores that overlap beyond a certain threshold. These steps are repeated until the simulation reaches "breakthrough", defined as a permeability ratio depending on the rock type (Table 4.6).

4.3.3 Emulsified Acid Consumption and Diffusion Coefficient

The diffusion coefficient (and therefore rate of mass transfer) of HCl in emulsified gel is expected to be different than in water for several reasons. First, the gel has a larger radius of gyration and is less homogenous; second, the viscosity of the gel is

much larger than water. Lastly, the viscosity of the gel is shear-rate dependent. Macroscopic experiments suggest retarding the diffusion coefficient by a factor of 10 to 100 (de Rozieres et al., 1994, Navarrete et al., 1998). This option is investigated, but it does not account for shear-dependency of the viscosity and its impact on local diffusion.

A more fundamental approach to modeling diffusion involves a direct relationship between the diffusion coefficient and shear-dependent fluid viscosity. The Stokes-Einstein equation (Eqn 2.3) is the simplest theoretical model, although it is only intended to describe drag force on a particle in a medium with homogeneous viscosity rather than suspension of species in emulsified oil droplets. Nonetheless, it predicts an inverse relationship between viscosity and the diffusion coefficient. Hansford and Litt (1968), and De Rozieres et al. (1994) present a semi-empirical correlation that relates the diffusion coefficient to velocity by the power of 1/(1+n) (Eqn 2.4). However, this equation describes mass transfer as a function of rotation speed for a spinning disc, and is therefore difficult to apply directly to pore scale models. Nonetheless, these analyses suggest that the diffusion coefficient for emulsified acids is related to the shear rate (or viscosity) according to the semi-empirical relation in eqn 4.1. The coefficient *a* can be obtained from experimental studies, or history matched as necessary.

$$D_e = a\gamma^{1/(1+n)} \tag{4.1}$$

4.4. Simulation Results and Discussion

4.4.1. Non-Reactive Tracers and Flow Field Analysis

Non-reactive tracers were simulated on the each rock type using a Newtonian (μ = 8.9×10^{-3} gm/cm·s) fluid model. Experiments were conducted at sufficiently high Péclet number ($Pe = Lu / D_e$ >10,000) such that it was advection-dominated. Figure 4.5 shows the tracers for both simulations and experiments conducted by Schlumberger. Table 4.3 shows the flowing fraction of each rock type, defined as the number of pore volumes required to reach C_{end}/C_0 = 0.5. Zakaria et al., (2015) identified this metric as important in capturing medium heterogeneity and fluid residence time in the context of matrix acidization.

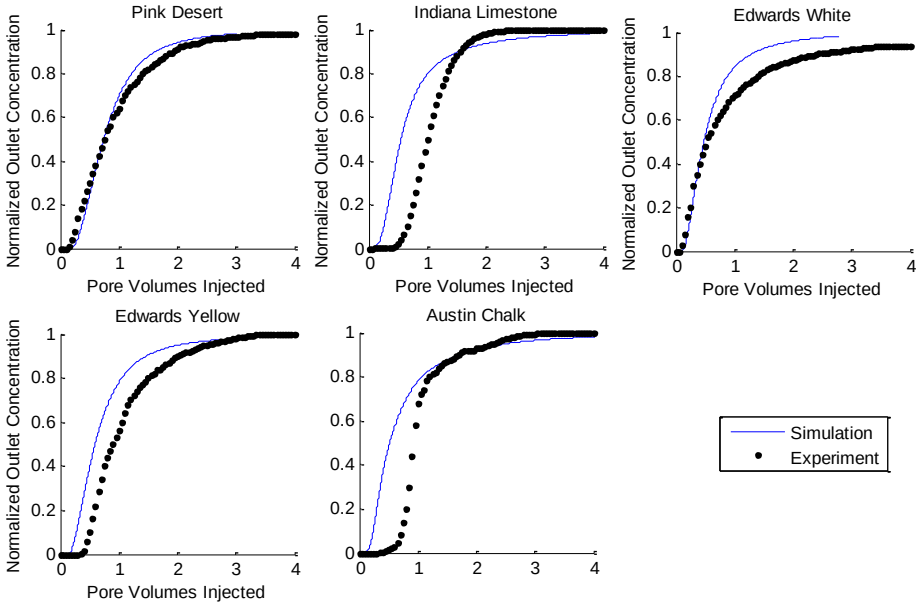

Figure 4.5: Nonreactive tracer tests for studied carbonate rock types.

Table 4.3: Summary of flowing fractions for carbonate rock types

Rock Type	Experimental Flowing Fraction ($C_{end}/C_0 = 0.5$)	Simulation Flowing Fraction ($C_{end}/C_0 = 0.5$)
Pink Desert	0.75	0.75
Indiana Limestone	1	0.55
Edwards White	0.53	0.48
Edwards Yellow	0.90	0.60
Austin Chalk	0.93	0.52

Of the five rock types, the Pink Desert sample matches the experimental tracer curve and flowing fraction closely. The Edwards White sample matches the flowing fraction well, but fails to capture the trailing breakthrough found in experiments. One possible cause of the discrepancy is the presence of microporosity below the resolution of the CT scan. Flow through microporosity could affect dispersion and medium capacitance more than is shown in network simulations.

For the remaining three rock types, the extracted networks appear to channel flow much more strongly than core floods, with tracer breaking through to the outlet almost immediately. Several possible explanations for the poor match were hypothesized. The Indiana Limestone was investigated in very close detail in the following subsections.

4.4.1.1. Experimental error

The first possibility to rule out is experimental error. Tracers on a similar Indiana Limestone core were conducted by Zakaria et al. (2015) and match very closely with the tracer provided by Schlumberger (Figure 4.6). In particular, breakthrough occurs at very

similar points in both experiments at a value of approximately 0.5. Therefore, the Indiana Limestone tracers are likely robust, and variations in sampling or other experimental errors are extremely unlikely to reduce tracer breakthrough by an order of magnitude.

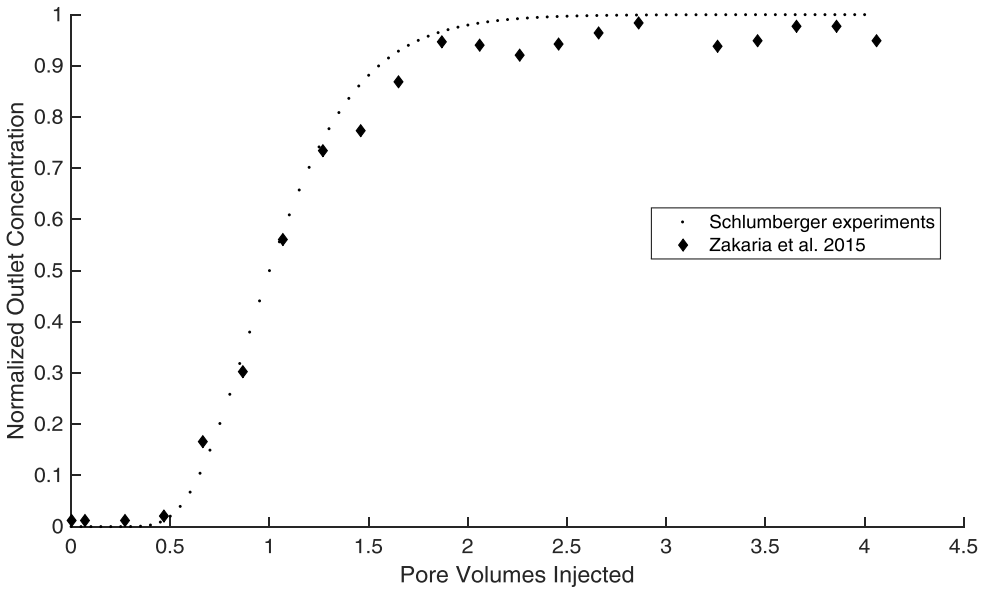

Figure 4.6: Comparison of nonreactive tracers conducted on Indiana Limestone

4.4.1.2. Network extraction method flawed

Another possibility is that the network extraction algorithm overestimates the heterogeneity of these carbonate networks, either by incorrectly assigning conductivity, or failing to identify all possible flow paths. However, the Indiana limestone is composed of definitive grains (Figure 4.7), and the network extraction algorithm was developed and tested extensively on granular media (Thompson et al., 2008).

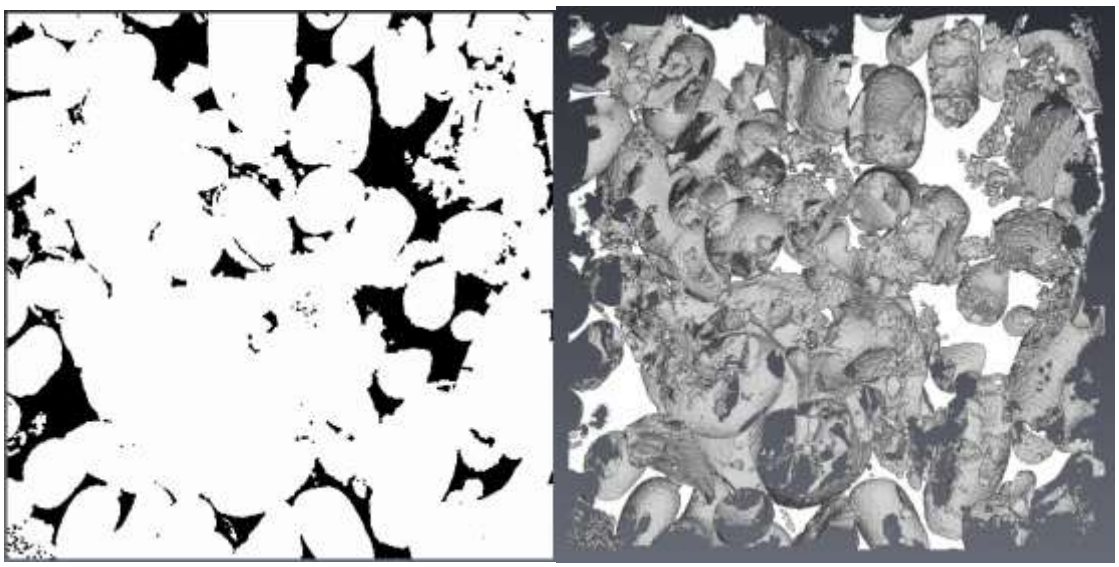

Figure 4.7: Binary slice of Indiana Limestone (left). Grain is shown in white, pore space in black. 3D voxelized image shows corresponding pore structure (right)

Nonetheless, a different network extraction algorithm was employed for comparative purposes. 3DMA-Rock's algorithm was used for this purpose. A comparison of network properties for the Indiana Limestone are shown below for both network extraction methods in Table 4.4. It utilizes a similar medial-axis path construction algorithm (Lee et al., 1994). Throat properties and cross-sectional surfaces are determined by local minima (Lindquist et al., 2000; Shin, 2002). Unfortunately, conductivity is not directly estimated by the algorithm. Here, the Hagen- Poiseuille relation (Eqn 2.4) is used to estimate throat conductivity using throat surface area to determine an effective radius. This is likely the reason that the 3dma network's permeability is significantly elevated. This assumption is not likely to affect relative flow rates in the matrix, and therefore tracer response. The 3dma algorithm also appears to divide the media into fewer, but more connected Pores, whereas the Thompson et al. (2008) appears to utilize more nodes to describe the pore space. Nonetheless, nonreactive

tracer simulations between the two networks match closely (Figure 4.8), indicating a high degree of similarity in flow paths. The fact that two different network extraction algorithms produced very similar networks supports the robustness of this step of the simulation.

Table 4.4: Comparison of network extraction algorithms for Indiana Limestone

	3dma	Thompson et al.
Permeability (mD)	1306.6	590.9
Porosity	0.0953	0.0953
Number of pores	4182	7500
Mean connectivity	4.577	3.8845
Number of throats	9823	15104

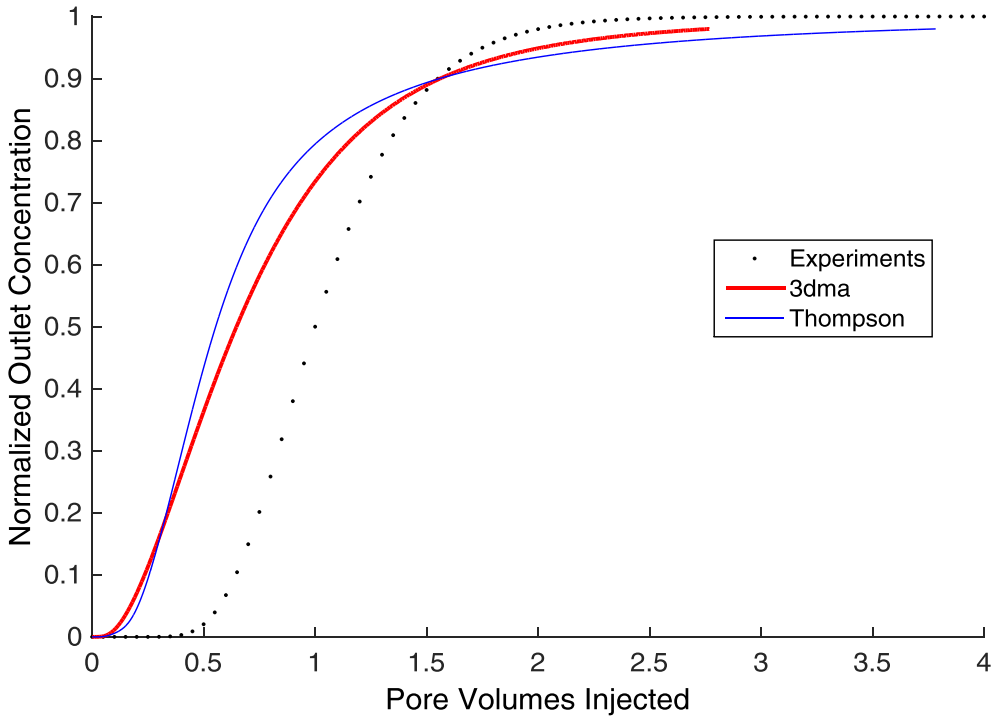

Figure 4.8: Comparison of nonreactive tracers for Indiana Limestone using different network extraction techniques

4.4.1.2. CT image quality insufficient

The second possibility is that the initial CT scan provided by Schlumberger was in some way defective. Image segmentation or sampling of an unrepresentative region are the primary sources of discrepancy. Therefore, an additional CT scan was taken from a different Indiana Limestone core at the University of Texas High-Resolution X-ray CT (UTCT) Facility.

A 1 inch diameter × 1 inch height core was provided by Schlumberger, and cut down to 2mm diameter 1 mm height for ease of scanning at 2 micron resolution (1000 voxels in each direction). The raw greyscale voxel space is shown in Figure 4.9A. Segmentation of the greyscale voxel space was achieved by using the indicator Kriging module in 3DMA-Rock (Oh and Lindquist, 1999). Erosion and dilation techniques were also employed post-segmentation in order to better resolve pore-spaces. Since networks are typically rectangular, an inscribed square cross-section of the CT scan was taken. The resultant binary voxel space is shown as an overlay in Figure 4.9B.

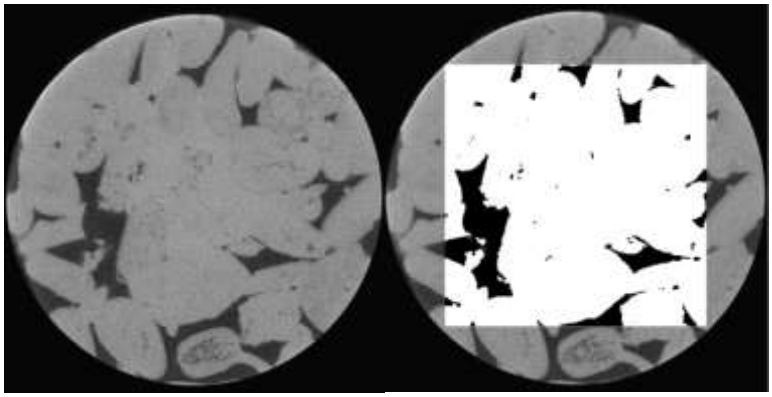

(A) (B)

Figure 4.9: Greyscale image of CT scan for second Indiana Limestone core (1mm diameter) (A). Binary image overlay after segmentation and post-processing (B).

A network model was extracted from the binary voxel space. Basic petrophysical properties are compared in Table 4.5. Porosity in the UTCT scan is approximately 25% higher while permeability is ~50% lower. Voxel resolution remains the same 2.2 microns as provided by Schlumberger, but domain size is smaller on the recommendation of UTCT technicians. Nonreactive tracers were simulated and compared with the original Schlumberger network (Figure 4.10). While the tracers between the two networks are perturbed slightly, the major trends remain the same. Breakthrough occurs significantly earlier, and the networks exhibit more channeling and tailing of the tracer compared to experiments. It is possible that both CT scans share the same flaw in quality, but obtaining the same result twice from two different Indiana cores suggests that sampling is unlikely to contribute to the significant amount of observed discrepancy.

Table 4.5: Comparison of Indiana Limestone CT scans

	UTCT	Schlumberger
Permeability (mD)	279.1	590.9
Porosity	0.1202	0.0953
Number of pores	2826	7500
Mean connectivity	3.029	3.8845
Number of throats	4480	15104
Domain length (mm)	0.6762	2.3

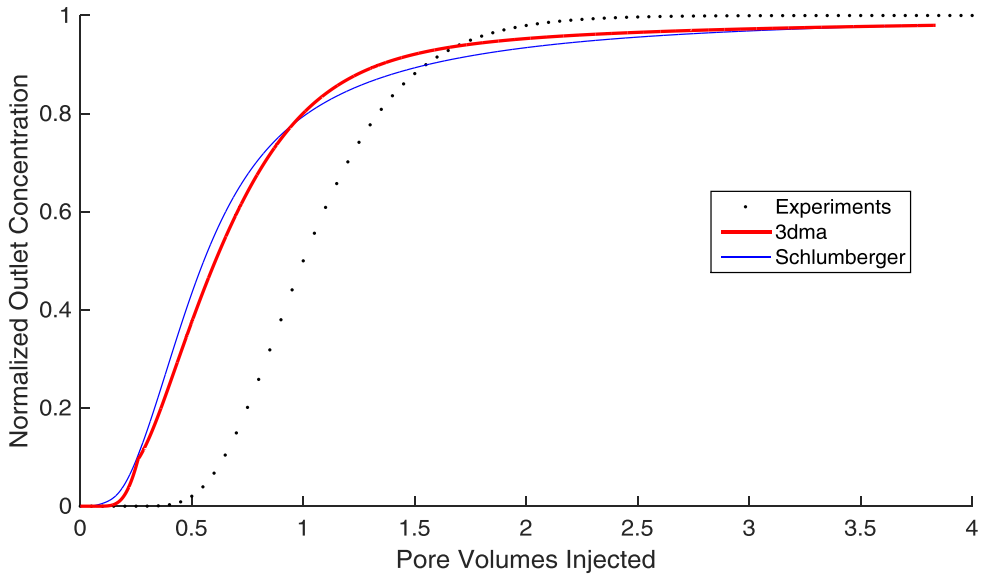

Figure 4.10: Comparison of nonreactive tracers for two Indiana Limestone samples

While the two image extraction techniques produce similar results, it is still possible that network extraction techniques are intrinsically flawed. Comparison with NMR data shows good agreement with the greyscale CT image obtained from UTCT (Figure 4.11). Unfortunately, the resultant network does not show a comparable bimodal distribution of incremental porosity or volume:surface area ratio (Figure 4.12). A very poor match between the network NMR data is likely due to the pore partitioning method. It is possible for several pores to be merged during network extraction, and it is also possible that real "pores" are actually represented by several nodes in a pore network model. The latter case is particularly likely in carbonates, as irregular pore geometry is likely to be sufficiently ambiguous as to produce inconsistent results with any rule-based network extraction algorithm. However, this does not mean that the resultant pore network model is necessarily inaccurate, as void-space volume is conserved (Table 4.2), and node conductivities can still be accurately assigned.

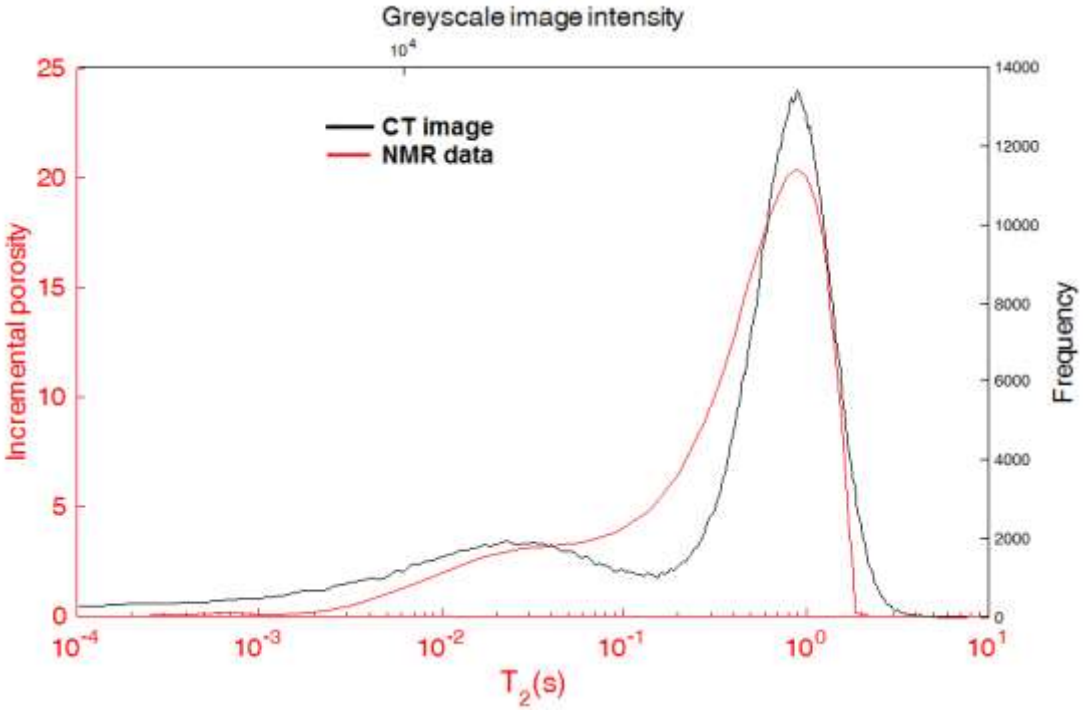

Figure 4.11: Comparison of incremental porosity from NMR and CT scan greyscale image

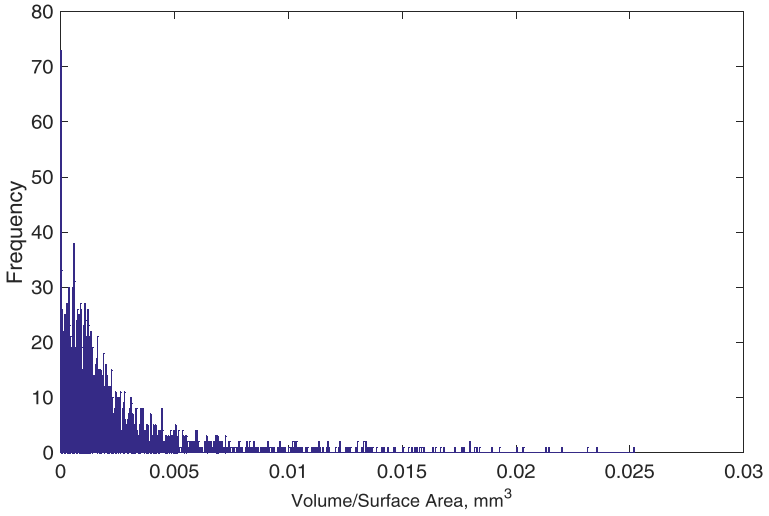

Figure 4.12: Histogram of volume:surface area ratio for network extracted from UTCT Indiana Limestone

4.4.1.4. Intrinsic deficiency in pore network modeling

In addition to manipulating network model inputs, other pore-scale models of nonreactive transport can be used for comparison. A particle tracking method (Bijeljic et al., 2004; Bijeljic and Blunt, 2007) performed by colleague Hongtao Yang confirms this finding, as strong channeling is shown along a dominant flow path (Figure 4.13), allowing particles to be delivered to the outlet extremely quickly. This indicates that the extracted networks are unusually non-dispersive. Figure 4.14 shows the comparison made with tracer tests, where the pore network and particle tracking method track closely together ahead of the core-scale experiments.

Figure 4.13: Particle tracking method for nonreactive tracer. At 0.13 pore volumes, a few particles have already reached the outlet.

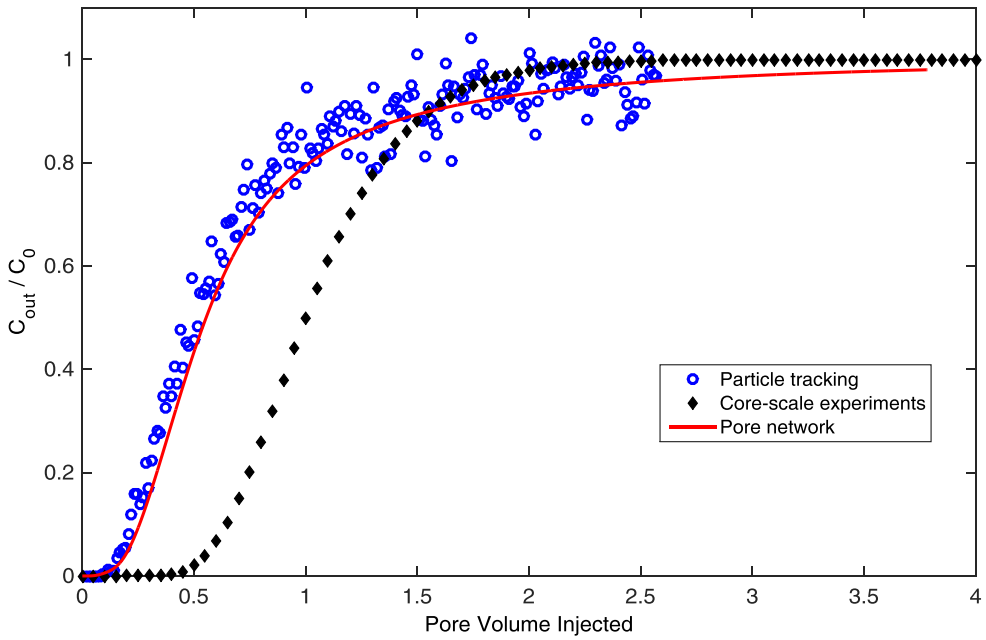

Figure 4.14: Comparison of nonreactive tracers in Indiana Limestone for particle tracking method, pore-network model, and core-scale experiments. Both simulations match each other closely and lag behind experimental values.

Furthermore, tracers for all simulations in the studied rock types break through extremely early. For example, for Indiana Limestone, simulated tracer breaks through at 0.05 pore volumes versus 0.5 pore volumes in the experiment. A third simulation technique is used to verify this early breakthrough. Colleague Dr. Yashar Mehmani utilized the CFD method in OpenFOAM © on the 3d segmented voxel space (Figure 4.15A) of our original Indiana Limestone. Solution for the flow field highlights an extremely conductive pathway (Figure 4.13B) that was implied by the particle tracking method in Figure 4.14.

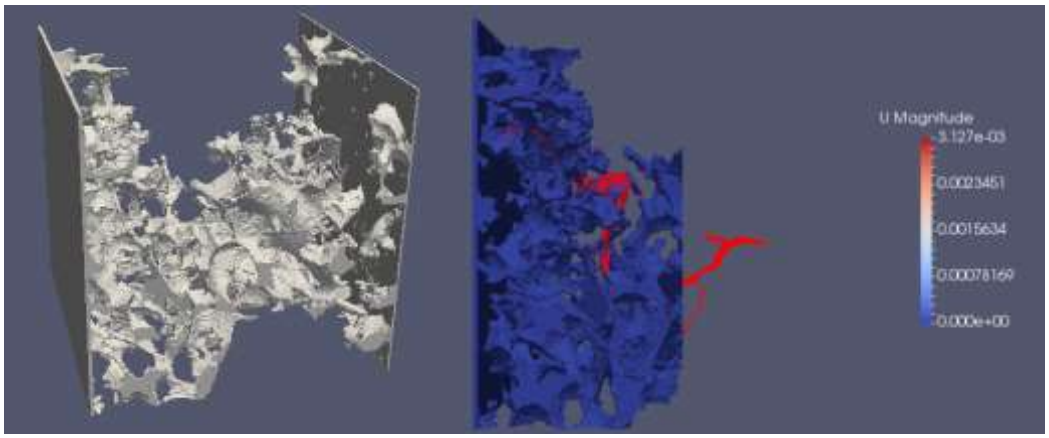

Figure 4.15: Fine-scale meshing of Indiana Limestone (A). Meshing (blue) and velocity streamlines (red) show extreme flow channeling (B)

Tracer tests were run sufficiently long enough to capture breakthrough of species (Figure 4.16), however computational constraints prohibited obtaining a full breakthrough curve. Breakthrough occurs at approximately 0.06 pore volumes, which is in good agreement with both previous simulation methods. However, CFD effluent tracer trends quickly upwards, indicating that network models may still underestimate channeling. Unfortunately, all results are still an order of magnitude lower than the experimental value for breakthrough. However, the agreement of early breakthrough between the three methods leads to a high level of confidence in the precision of our result.

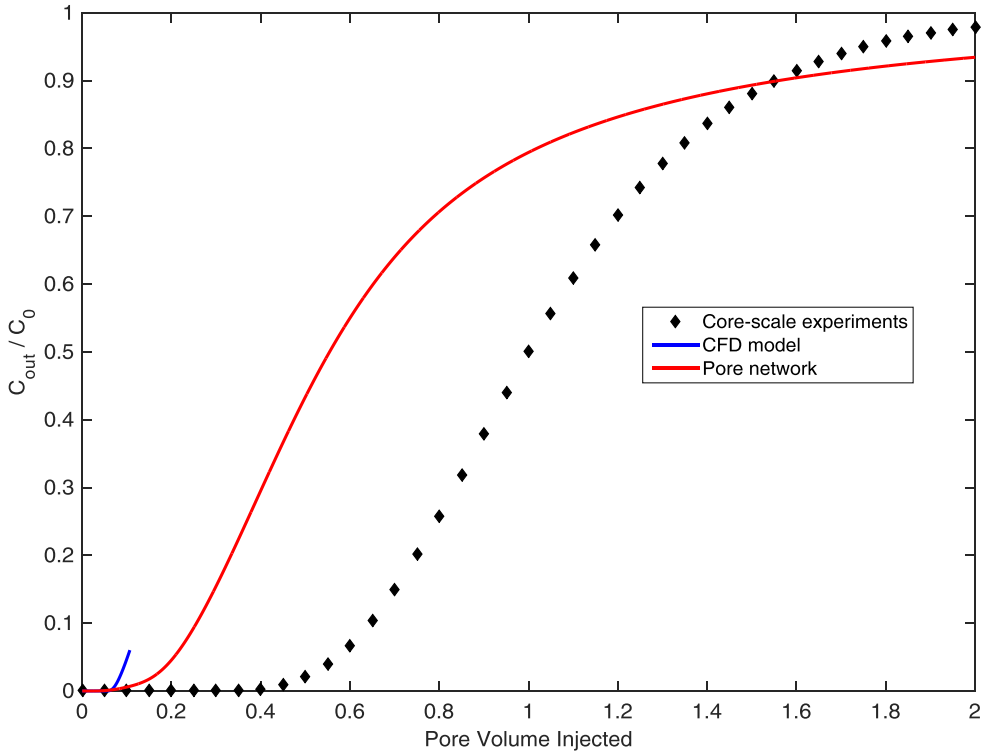

Figure 4.16: Nonreactive tracer profile for first 0.1 pore volumes of fluid injected. Tracer breaks through at approximately 0.06 pore volumes, while experimental outlet concentrations remain approximately zero.

4.4.1.5. Domain size below representative elementary volume

The final possibility discussed is that the CT scans are below the REV. This seems plausible, as visually the Indiana Limestone CT scan appears to have large very large grains relative to the domain size studied (Figure 4.7). A visual inspection reveals that the domain length is roughly 6 medium-sized grains (~200 grains total), significantly below the 1,000-40,000 grains typically used to model homogeneous sphere packs in the literature (Bryant et al., 1993; Balhoff and Thompson, 2008; Mehmani et al., 2012).

Additionally, all of the tracers for each rock type appear to break through an order-of-magnitude early compared to their corresponding core-scale experiments. Therefore, we hypothesize that the rock types are sampled below a representative elementary volume.

There are two primary methods by which this could be rectified. First, all of the rock types were sampled at approximately 2 micron resolution without regard to grain size. Current CT scanning methods operate in a tight window relating resolution and sample size. Finer resolution usually necessitates proportionately small sample sizes, and vice versa. Given how large the Indiana Limestone grains are relative to the domain size, it is likely that a coarser (and therefore larger) image of Indiana Limestone would yield a more realistic breakthrough time without losing significant petrophysical texture in the dominant pore spaces.

A second possibility is to scan a larger domain size at the same fine resolution. This would prove expensive and time consuming, but there is no theoretical reason why adjacent sections of a core could not be scanned sequentially at fine resolution. A composite image could be constructed from the resultant data. Depending on the domain size desired, a single pore network model could be created. More likely, however, is that simulation on a network 10^5-10^7 pores is computationally prohibitive (particularly for species transport and acidizing modules). Mortar coupling and hybrid modeling techniques provide a method by which large domains of network models can be

decomposed and solved in a parallel computing environment. These methods are explored and developed in chapter 6.

4.4.1.5. Omission of microporosity

Image CT scan porosity matches network porosity almost exactly, but systematically falls short of predicting experimental helium porosity values (Table 4.2). One hypothesized cause is the omission of microporosity, however it is also hypothesized that microporosity does not play a large role during matrix acidization, as acid channels preferentially through high-conductivity flow paths. This assumption is tested by introducing artificial microporosity into network models.

Finer resolution CT scans are not currently available, however techniques employed by Mehmani and Prodanović (2014) provide insight into the effects of microporous structures in sphere packs. Uniform sphere packs both with and without microporosity are compared. Microporous networks are inserted as part of the larger network in grains, representing partially dissolved grain space. Due to the large number of pores introduced by microporous structures, the total domain size is approximately 100 large pores representing 20% porosity and 2000 micropores adding 2% porosity. This is expected to be below the representative elementary volume for most network modeling applications, but nonetheless allows for equitable comparison between the two networks.

Minimum pore volumes to breakthrough are reduced with the introduction of microporosity, and the optimal Damköhler number is increased (corresponding to a slower optimal injection rate) (Figure 4.17). Microporosity plays a small but significant role during dissolution, accelerating the growth of pores adjacent to the microporosity (Figure 4.18). This is primarily mediated by the existence of additional pore volume that can be added to large pores along the dominant flow path, and not due to the very small

amount of flow diverted through microporosity itself. The addition of microporosity to the carbonate rock networks is therefore not likely to rectify the nonreactive tracer tests, although could have notable effects on acidization.

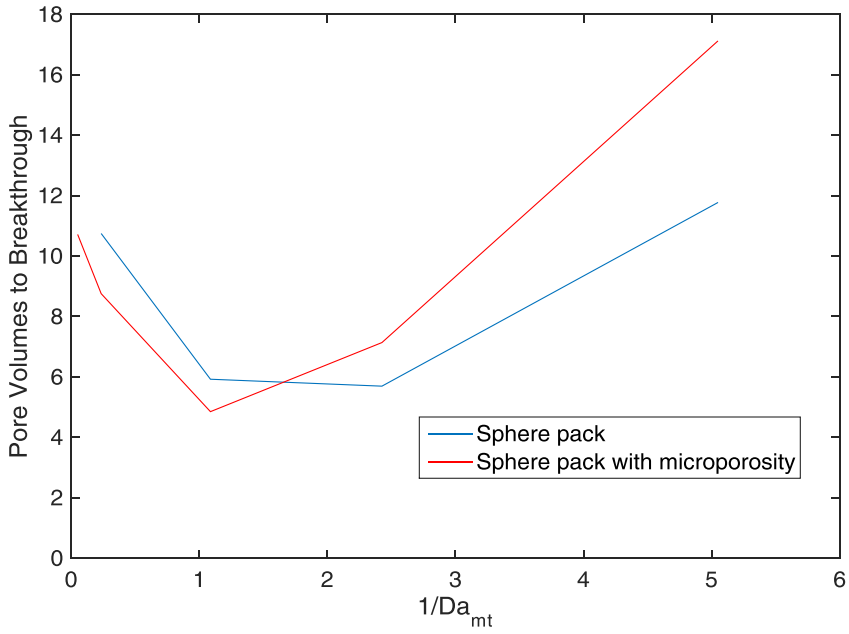

Figure 4.17: Comparison of pore volumes to breakthrough in sphere pack with and without microporosity

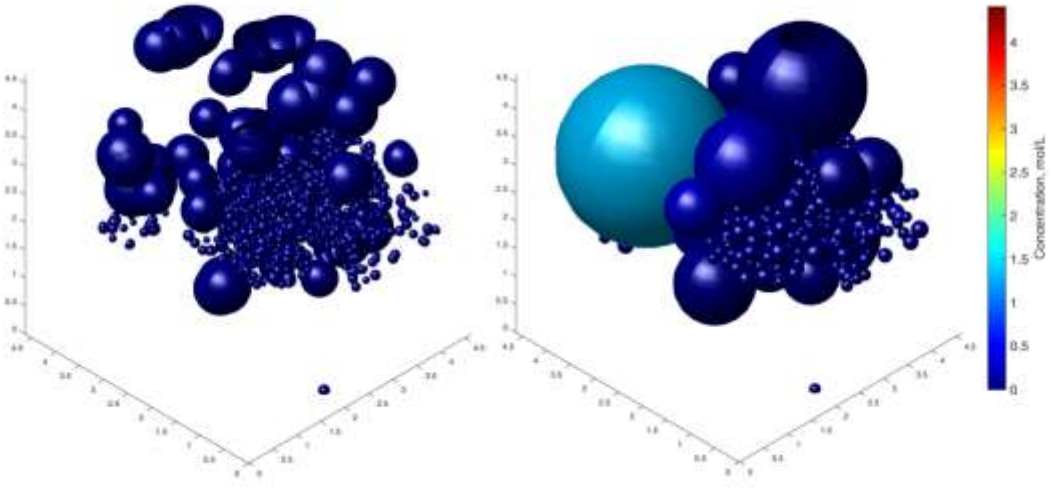

(A) (B)

Figure 4.18: Initial microporous network (left) and final dissolved network at optimal injection rate (right)

4.4.2. Dissolution with Newtonian HCl

Despite the poor tracer match for some rock types, full acidizing simulations were conducted. 15 weight percent (4.4 M) hydrochloric acid was injected through one face of the domain across a range of injection rates until breakthrough (Table 4.6) was achieved. Qualitatively, an overhead view of the Pink Desert simulation at breakthrough for different injection rates representative of the three dissolution regimes is shown in Figure 4.19 below. The growth in permeability ratios for the same three characteristic injection rates are plotted in Figure 4.20.

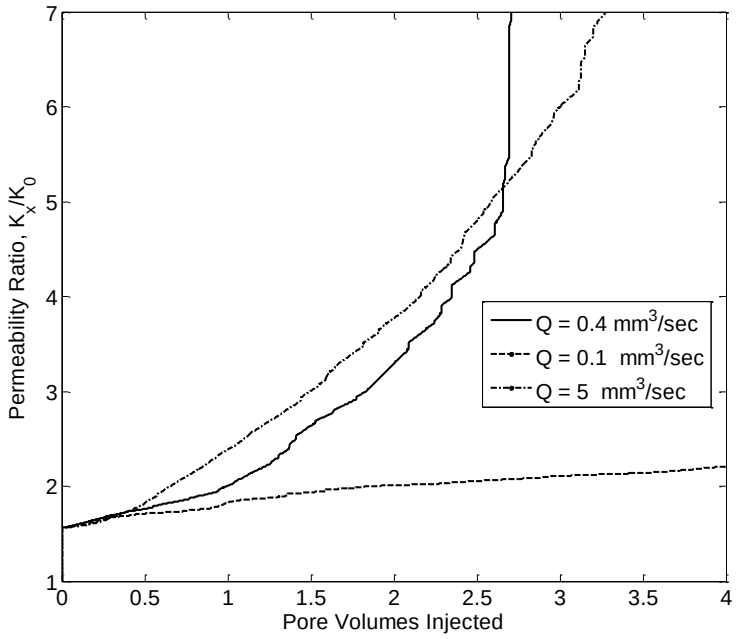

Figure 4.19: Permeability increase for three characteristic injection rates. Injecting above the optimal injection rate is verified to be preferable to injecting too slowly.

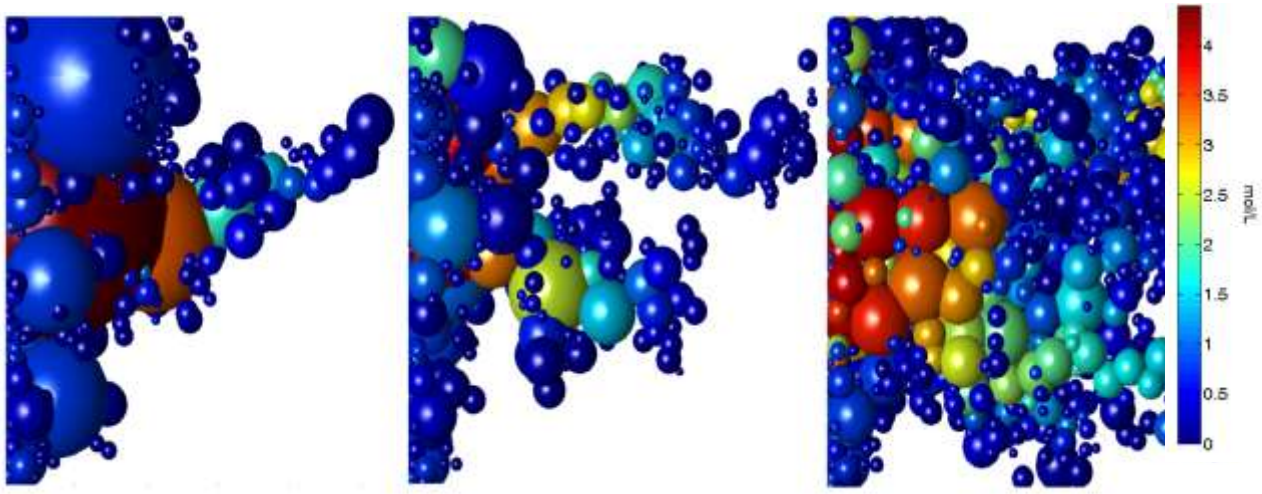

Q = 0.1 mm^3/sec	Q = 0.4 mm^3/sec	Q = 5 mm^3/sec
PVBT = 9.2	PVBT = 2.7	PVBT = 3.3
(A)	(B)	(C)

Figure 4.20: Overhead view of Pink Desert simulation. Heat shows acid concentration (mol/L). Only pores whose concentration falls above 0.1 mol/L are shown. Figure (A) shows face dissolution at 0.1 mm^3/sec, Da_{mt} = 3.52. Figure (B) shows the optimal injection rate of 0.4 mm^3/sec, Da_{mt} = .478. Figure (C) shows uniform dissolution at 5 mm^3/sec, Da_{mt} = 0.102.

The pore volumes to breakthrough (PVBT) at each injection rate for all rock types is shown in in Figure 4.21. Damköhler number is defined for the mass transfer limited regime (Eqn 2.2) as proposed by Fredd and Fogler (1999). Likewise, a diffusion coefficient of 3.6×10^{-5} cm^2s^{-1} (HCl in water) is implemented. Breakthrough was defined as a specified ratio of permeability increase (Table 4.6). The final permeability ratio comes from the experiments conducted by Schlumberger, and is different for each rock type. For the Austin Chalk, no experimental data was available, and therefore the default value of "10" was used from Chapter 3. However, the optimal Damköhler number was

found to be almost insensitive to any breakthrough criterion above a permeability ratio of 5.0, as permeability increases steeply after this threshold.

Table 4.6: Experimental permeability ratios by rock type

Rock Type	Average Experimental "Breakthrough" Ratio (K_x/K_0)
Pink Desert	7
Indiana Limestone	16
Edwards White	30
Edwards Yellow	8
Austin Chalk	N/A

The optimal Damköhler number compares favorably with most experiments (Table 4.7), predicting the experimental optimal injection conditions within a factor of 2. However, it is worth noting that the experimental data point resolution is approximately 0.1 Da, and that the experiments do not show much sensitivity in pore volumes to breakthrough within the studied range. For example, at Da_{mt} = 0.23 and 0.42, the experimental PVBT for Pink Desert was 0.54 and 0.53 respectively, while the simulation optimal Da_{mt} was 0.30. Thus, it may be more accurate to perceive acidizing experiments as confirming a range of efficient Damköhler numbers, rather than identifying a strict optimal value. The simulation-predicted optimal Damköhler number falls in this range for all rock types except for the Austin Chalk.

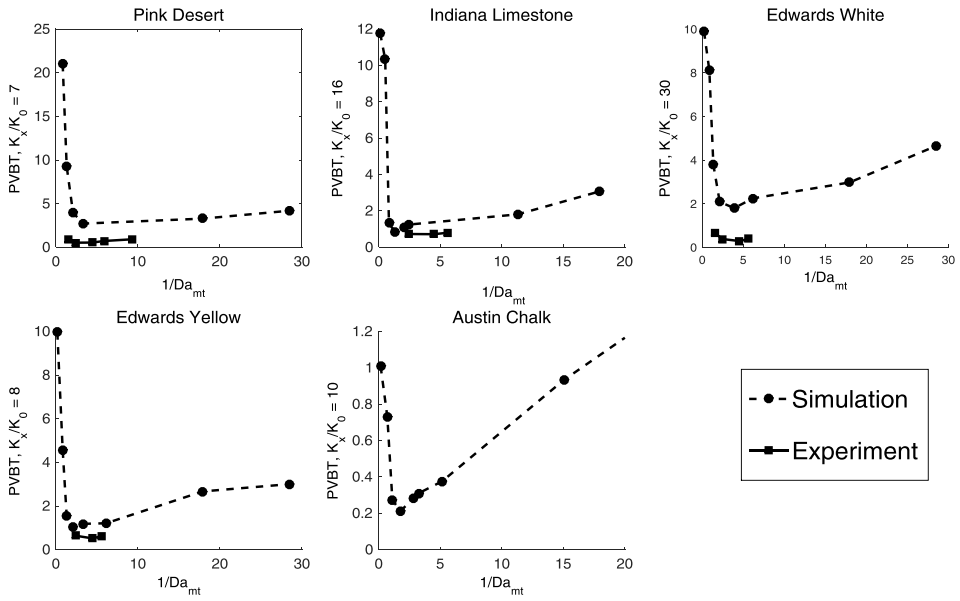

Figure 4.21: Pore Volumes to Breakthrough for each rock type

Table 4.7: Comparison of experimental and simulation acidizing results

Rock Type	Experimental Da_{opt}	Simulation Da_{opt}	Experimental PVBT	Simulation PVBT
Pink Desert	0.42	0.30	0.53	2.71
Indiana LS.	0.22	0.76	0.60	0.84
Edwards White	0.22	0.25	0.28	1.79
Edwards Yellow	0.22	0.48	0.43	1.06
Austin Chalk	N/A	0.56	N/A	0.21

Outside of the optimal injection rate, the simulations find that injecting too quickly usually results in only modest decrease in breakthrough efficiency. This is supported by the experimental data points, which have a similar slope above the optimal injection rate. Furthermore, the simulations predict that injecting at slow rates (Da_{mt} = 0.75 and above) leads to extremely inefficient face dissolution. This is commonly observed in acidizing experiments (Fredd and Fogler, 1999), but data points on the rock types here do not extend past Da_{mt} = 0.65.

The major discrepancy between experiments and simulations is the number of pore volumes to breakthrough (at any injection rate). For all rock types except the Austin Chalk, the number of pore volumes to breakthrough predicted by the model was significantly higher than found in experiments. Fredd and Fogler (1998b) also reported higher pore volumes to breakthrough and speculated that domain size was likely to be the primary cause. However, the variation in PVBT (0.21-2.71) of networks indicates that networks are capable of breaking through very quickly, and that domain size cannot be the sole reason for delay. Nonetheless, simulations at larger domain sizes using mortar coupling and hybrid modeling techniques are explored in chapter 6.

Simulations with more aggressive pore merging and throat enlargement were attempted, but did not yield significant reduction in PVBT. Increasing the acid-capacity (or injected concentration) decreased the pore volumes to breakthrough, although this is strictly a history matching technique. One other possibility is the assumption of uniform pore growth, which may overestimate the thickness of wormholes while retarding their

propagation throughout the network. Anisotropic elongation of pores is not supported by the current network modeling method, which if implemented rigorously, it is speculated could more accurately capture the pore volumes to breakthrough in most rock types.

4.4.3. Dissolution with Emulsified Acid

4.4.3.1. Basic Power Law Model

Acidizing experiments using an acid-in-diesel emulsion were conducted by Zakaria et al. (2015) on the aforementioned rock types. Power law rheology was simulated according to Eqn 2.5, with k = 98.13 gm/cm-s^{n-2} and index n = 0.64. Computation of the power law pressure field is much more computationally expensive than the Newtonian case. Therefore, simulations were conducted on a corner (subset) of the original Pink Desert network to allow more rigorous investigation of different emulsified acid models. The network properties are summarized below (Table 4.8).

Table 4.8: Summary of Pink Desert sub-network properties

Rock Type	Length	Porosity (PU)	Permeability (mD)
Pink Desert	0.575	31.4	560

15 weight percent (4.4 M) hydrochloric, emulsified acid was injected through one face of the domain across a range of injection rates until a permeability increase of a factor of 7 was achieved (breakthrough). For the purposes of investigating only the influence of power law rheology on breakthrough patterns, the diffusion coefficient was

left at the Newtonian value of 3.6×10^{-5} cm^2s^{-1}. The minimum number of pore volumes to breakthrough (Figure 4.18) occurs at a 0.83, a reduction of only 12% compared to the Newtonian simulation. This decrease is due to some diversion of fluid into large pores along the dominant flow path, since the relative viscosity in low-shear regions is increased by the power law rheology. However, analysis of the flow field showed only small changes from the Newtonian simulations and the direct effect of rheology does not appear strong enough to capture the significant and universal decrease in pore volumes to breakthrough observed in emulsified acid experiments. Experimental data (Figure 4.2) shows that the emulsified acid resulted in (1) a lower pore volumes to breakthrough and (2) a very flat PVTB vs. 1/Da curve. Furthermore, both Newtonian and power-law PVBT curves (Figure 4.22) have a very similar shape at all injection rates. This is inconsistent with the experimental data which show a flatter curve for the emulsion. It is concluded that the improved dissolution efficiency and insensitivity to injection rate of emulsions cannot be explained by an altered flow field alone, if at all.

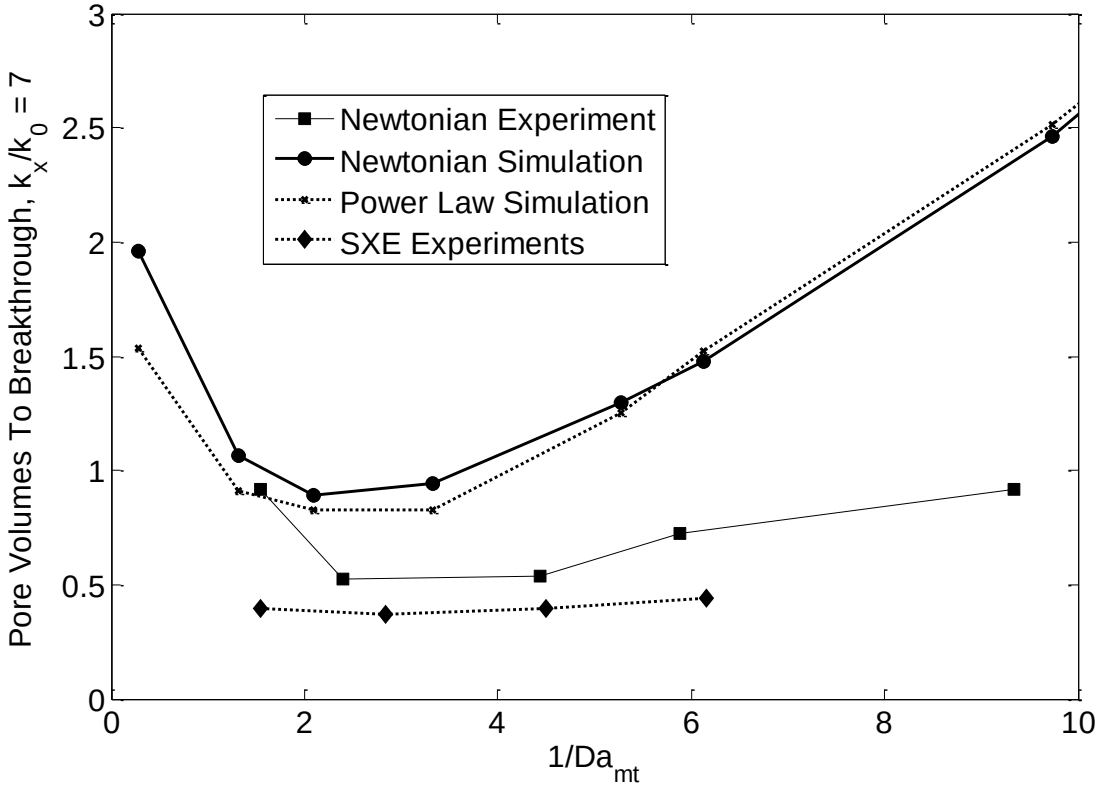

Figure 4.22: Simulation with only power law flow field implemented. The power law fluid shows slightly reduced pore volumes to breakthrough at all injection rates, but maintains sensitivity to injection rate.

4.4.3.2. Scalar Reduction in Rate of Diffusion

It is commonly claimed that emulsions retard reaction of HCl by a factor of 10 to 100. These observations are typically based on macroscopic experiments, such as a rotating disk apparatus (de Rozieres et al., 1998). This change is implemented using the same simulation parameters as above, except the mass transfer coefficient is scaled by a factor of 10.

The primary impact of scaling the rate of reaction is to shift the curve leftwards without changing the number of pore volumes to breakthrough. This is expected, as slowing the reaction rate should improve performance at “low” injection rates, while becoming less efficient at higher rates. It does not, however, change the fundamental physics and provide a mathematical means by which emulsified acid can be more efficient across a large range of injection rates.

4.4.3.3. Shear-Dependent Diffusion Coefficient

In section 2.4, it was hypothesized that the dynamic relationship between shear rate and viscosity in power law fluids implies a dynamic diffusion coefficient. Therefore, the dynamic diffusion coefficient proposed in Eqn 2.5 is employed. The coefficient a is history matched to the experimental data and found to have a value of $3.62 \times 10^{-5}\ mm^2$.

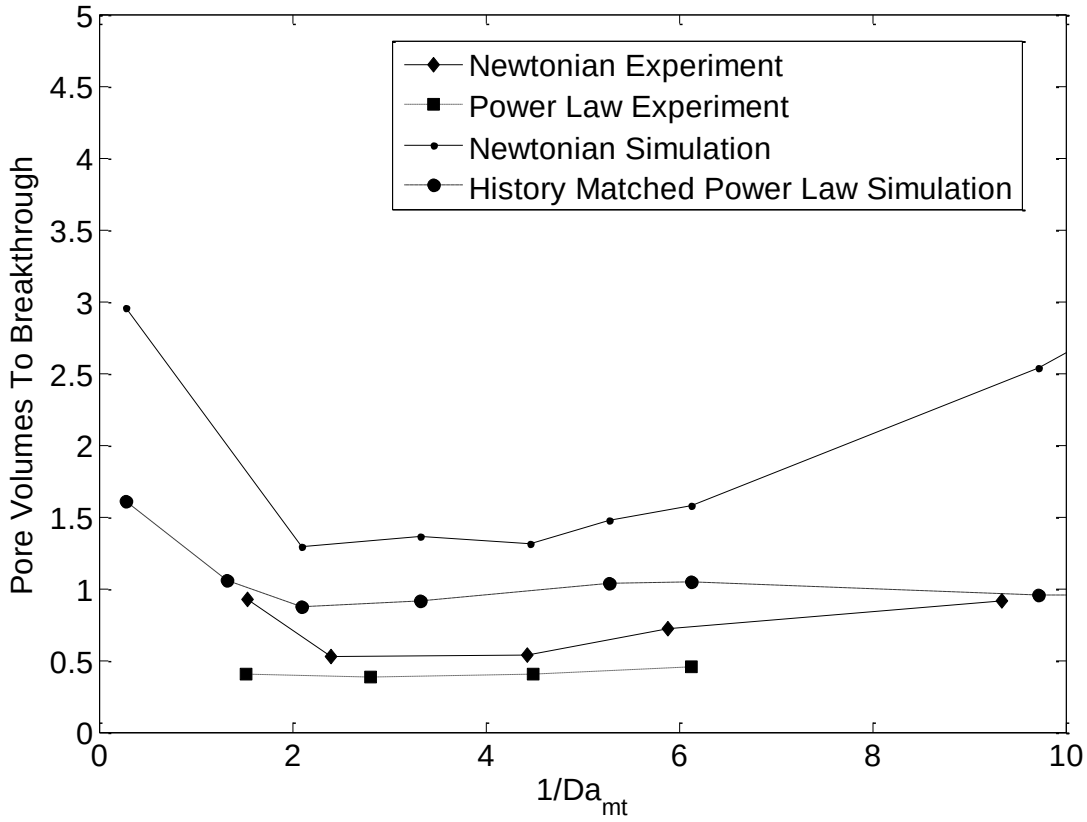

Figure 4.23: Simulation with history matched diffusion coefficient for power law fluid. The power law fluid shows less sensitivity to injection rate at low values.

The number of pore volumes to breakthrough decreases considerably (Figure 4.23), and the curve remains flat across intermediate and high injection rates. The core still exhibits face dissolution at low injection rates, although remains more efficient than Newtonian acid. Figure 4.24 shows a comparison between pore-scale mass transfer coefficients for the Newtonian and emulsified acid simulations. While very little difference in bulk flow rate exists between the two, a large difference in mass transfer coefficient exists. The reduced viscosity along the dominant flow path amplifies mass

transfer along the dominant flow path, while retarding it elsewhere. This is proposed to be the primary method by which emulsified acid improves treatment efficiency.

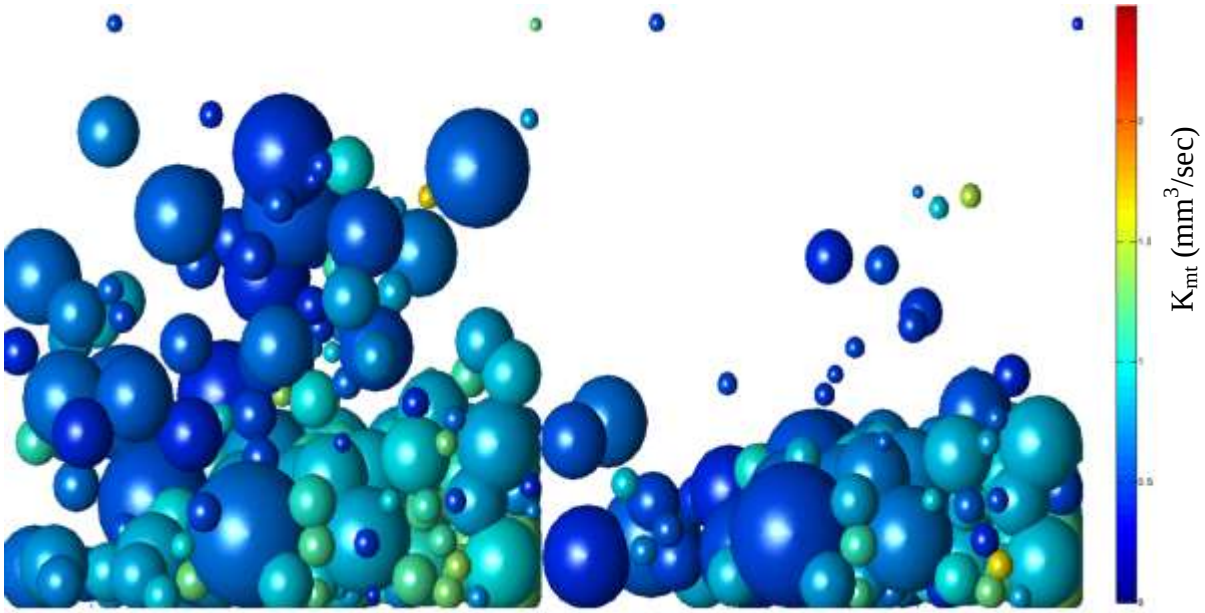

Figure 4.24: Mass transfer coefficient for Newtonian case (left) compared to emulsified acid (right). While the emulsified acid does not alter the flow field appreciably, the mass transfer coefficient of acid is much more concentrated along the dominant flow path.

4.5. CONCLUSIONS

One major goal of this research has been the construction of a pore network model that is quantitatively predictive of acidizing experiments. However, the approach taken here falls short of this even before advanced physics are tested. Porosity and permeability are generally poorly matched by networks extracted from 1-2 mm length CT scans of carbonate rocks. Tracers also consistently exhibit breakthrough far earlier than their corresponding experiments, indicating severe flow channeling in networks.

Numerous hypotheses for these discrepancies were evaluated. Intrinsic deficiency of pore network models was ruled out by comparison with alternative pore-scale methods performed using the same inputs. Sampling bias was also investigated with an alternative scan of the Indiana Limestone and shown not to significantly affect tracer results.

While pore network models have not been shown here to reliably offer predictive values for basic petrophysical properties, the results strongly suggest that simulations are below an REV. All rock types were scanned using the same 2 micron resolution. Future work should include a study investigating REV and property quality as they relate resolution fineness. Grain and pore size can likely be related to optimal scanning resolution size. REV can likely be related to specific rock types, depending on their unique spatial correlation of geologic features.

Despite the difficulty in capturing nonreactive tracer response accurately, acidization simulations were usually close to experimental values. However it is difficult to tell how accurate simulations are, as most experiments only contain 3-4 data points, and simulations often predict an optimal Damköhler number not investigated experimentally. Network models and the experiments studied here also tend to return optimal Damköhler numbers close to the global average of 0.29. To determine whether network models are capable of predicting an optimal Damköhler number significantly outside this range, a specific porous medium whose Damköhler number (or acidizing behavior) does not follow the familiar pattern would provide better verification.

Finally, most simulations returned a significantly higher number of pore volumes to breakthrough than seen in experiments. Pore volumes to breakthough is hypothesized

to be a strong function of domain size. This is investigated in chapter 6 using mortar coupling and hybrid modeling techniques.

Simulations on non-Newtonian acids are also performed with moderate success. History matched parameters reveal that there must be a positive relationship between local shear rate and local mass transfer in order to explain the flattened shape of the "pore volumes to breakthrough" curve (Figure 4.19). The enhanced dissolution along dominant flow paths increases the efficiency of injected acid, lowering pore volumes to breakthrough. However because rheological properties are shear-dependent, simulations (and experiments) are not domain size independent, and a history matched parameter for the network models is not likely to match experiments conducted at different scales. Numerous experiments conducted on different length cores are necessary to study the domain size effect on non-Newtonian acidizing behavior.

Chapter 5: Development of Mortar Methods for Matrix Acidizing with Pore Network Models

5.1. INTRODUCTION:

In the previous chapters, an accurate method was developed by which the optimal injection conditions can be obtained using a single pore scale network model. In chapter 6, domain size effects using larger domains composed of multiple networks will be investigated. Mortar coupling techniques are used to join networks together at the interface. They are shown to be accurate in a series of test cases comparing the single-network solution to the same network partitioned into subdomains using mortars. Accuracy is verified for each physical module (flow, species transport, reaction, pore merging), verified sequentially. The pore volumes to breakthrough curve are also reproduced using mortars.

5.2. MODEL DEVELOPMENT:

Mortar coupling techniques have been used to couple network models together accurately (Balhoff et al., 2008; Mehmani et al., 2012a). Pressure and concentration fields have been shown to match accurately at the interface in the context of reactive transport with shrinking pores (Mehmani et al., 2012b). Their specific method of mortar coupling is employed here, solving implicitly for pressure at the interface. For full details of the *Global Jacobian Schur* (GJS) method, see Mehmani et al. (2012a). GJS is a simplified version of the method presented by Ganis et al. (2012) in that GJS solves only

for pressure at the interface as opposed to both pressures and velocities. Here, a brief outline is presented outline.

First, the domain is decomposed into nonoverlapping components. For the simulations performed in this chapter, this amounts to cutting a single network in half (for verification purposes). It could also involve coupling many full networks to one another. Mortar spaces are placed between subdomains with guess-values for interface conditions (Lagrange multipliers) representing pressure and concentration. Pores are divided into bundles at the interface using the raw-grid-based interface pore partitioning (RGIPP) method (Mehmani et al., 2012). The algorithm ensures that an equitable number of pores belong to each bundle from both sides of the mortar space. The number of bundles is a user input, with fewer bundles corresponding to coarser mortar resolution.

Subdomains are solved independently using their local boundary conditions. The fluxes on both sides of the mortar faces are compared. The Jacobian of partial derivatives is calculated for each grid-space on the mortar, and the Lagrange multipliers are updated with a new guess value. This iterative process is repeated until fluxes match within a specified tolerance.

One important difference in this work is the way in which mortar spaces project flux onto boundary pores. In Mehmani et al. (2012a), pressures are projected onto pores based on their location near the boundary. Therefore, if a network is cut in half, boundary projections will not necessarily associate neighboring pores, depending on grid positions (Figure 5.1A). This phenomenon is relatively unimportant in prediction of macroscopic permeability, but becomes significant when the exact pore-level solution of the flow field

is desired. An alternative projection method is proposed, whereby the boundary pressures are projected onto pores based on the location at which their throats intersect the boundary, preserving pore-connectivity even at infinitely fine mortar resolution (Figure 5.1B). This modification results in an extremely high level of accuracy for solution of the flow field for each individual pore. A 45 degree plot of flow rates for the mortar solution and single-network solution is shown in (Figure 5.2), where points above or below the red line of equality indicate error. While the projection method may matter less at coarser mortar resolutions, it is particularly useful in order to test and demonstrate of the exact accuracy of more complex modules (reactive transport, acidization) in section 5.3.

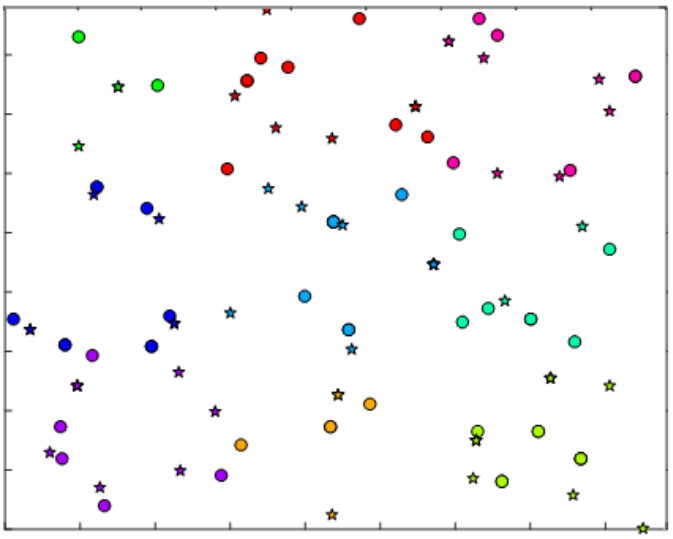

(A)

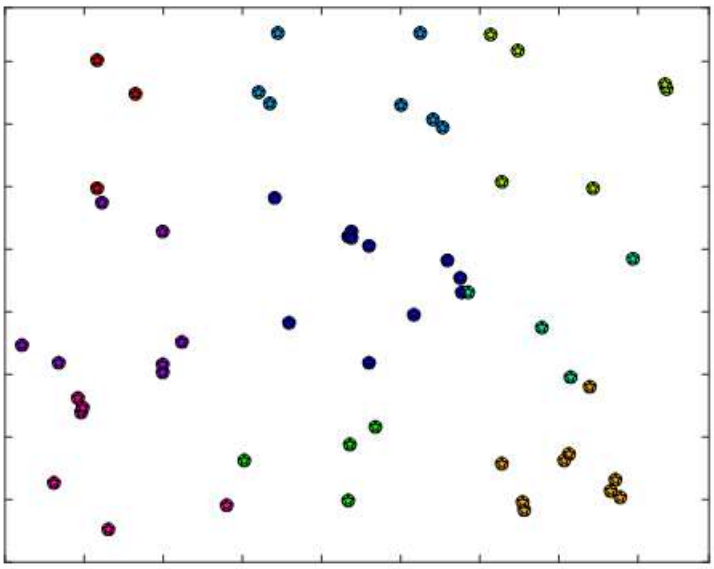

(B)

Figure 5.1: Projection points from mortars from both sides. Network A shown as circles. Network B shown as stars. Color indicates (irregular) RGBIPP bundle affiliation. Original method using pore-locations (A) shows ambiguous grouping of pore bundles. Throat-based projection method (B) shows exact match of previously-connected pores.

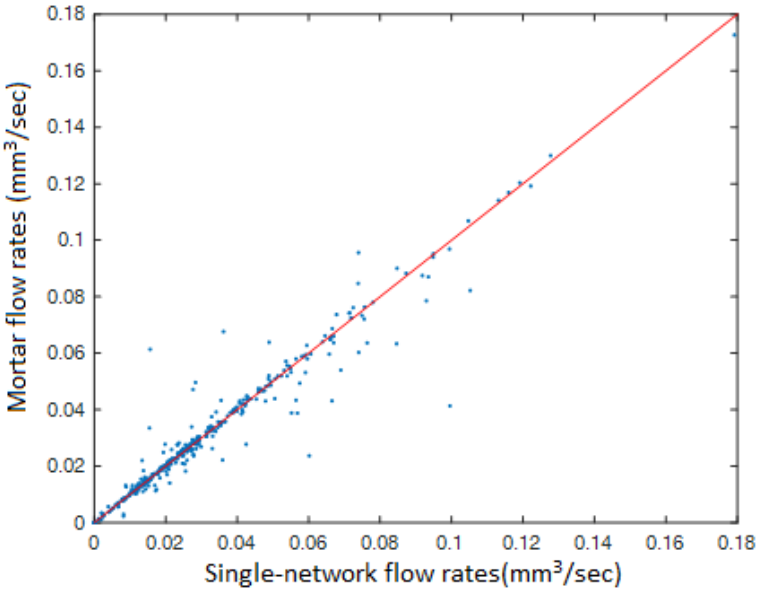

(A)

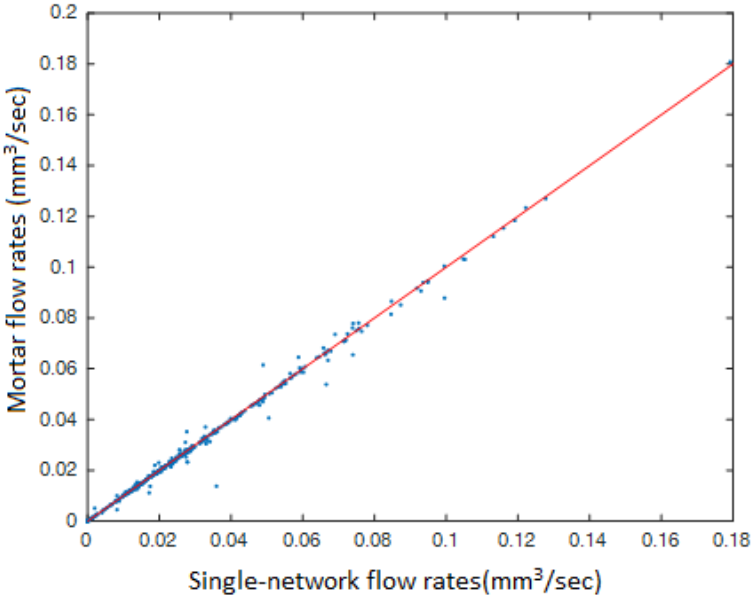

(B)

Figure 5.2: 45 degree plot of pore flow rates between mortars and single-network solution using infinite mortar resolution. Despite producing nearly-identical macroscopic permeabilities, Pore-based projection method (A) shows 33% average relative error in pore body flow rates. Throat-based projection method (B) shows 0.14% average relative error in pore body flow rates.

In this work, most simulations are at sufficiently high Péclet number (>1000) such that inter-pore diffusion is neglected. Species transport can be modeled without the need for interface coupling. The boundary conditions from one domain are simply projected as boundary conditions to adjacent networks. This method is tested to be accurate in section 5.3.

For the single network solution developed in chapter 3, reaction was modeled at each individual pore node (Eqn 3.3). Therefore, knowledge of the pressure field and interface boundary conditions is sufficient to solve for reactive transport in our pore network model. For our expressions, species consumption is not an intrinsically coupled problem.

Conversely, pore merging is an inter-pore physical module. A major appeal of mortar coupling techniques is the ability to solve subdomains independently on different computational nodes. However, growing pores at the mortar interfaces will eventually "overlap" significantly in real space. While they would be merged according to the original algorithm solving a single-network, a subroutine to check if boundary pores need to be merged across subdomains is required to capture pore merging with complete accuracy during the coupled problem. Furthermore, after a pore has been merged, both sub-networks need to be restructured to ensure correct pore-to-pore connections both intrinsically and across the interface. Due to the complexity of this task and the desire to preserve the ability to efficiently parallelize the problem, it was chosen to ignore pore merging across mortar interfaces. This decision is shown to preserve a high degree of accuracy in section 3.

5.3. VERIFICATION WITH PINK DESERT CARBONATE NETWORKS

Mehmani et al. (2012a) established the accuracy of the GJS method for homogeneous sphere packs. Here, a similar approach shows accurate network physics in a Pink Desert carbonate sample. The Pink Desert carbonate is taken as a $1/4^{th}$ subset of the full sample investigated in chapter 4 for two reasons. Firstly, to improve computation time in order to run many comparison simulations. A second advantage is to increase the numerical effects of mortars for observation, since a smaller domain volume means the number of pores split on the boundary is proportionately higher compared to the number of internal pores.

Results from the full solution on a single network are used as the basis of comparison. A single mortar is placed normal to the flow direction (Figure 5.3) using first-order (linear) basis functions. Mortars of varying grid resolution are used in order to assess tradeoffs between computational load and solution accuracy. The most accurate mortars have "infinite" resolution, where at the mortar boundary, every pore remains connected to its previous neighbor. Coarser mortar spaces necessarily relax this restriction, bundling several pores together in a single grid.

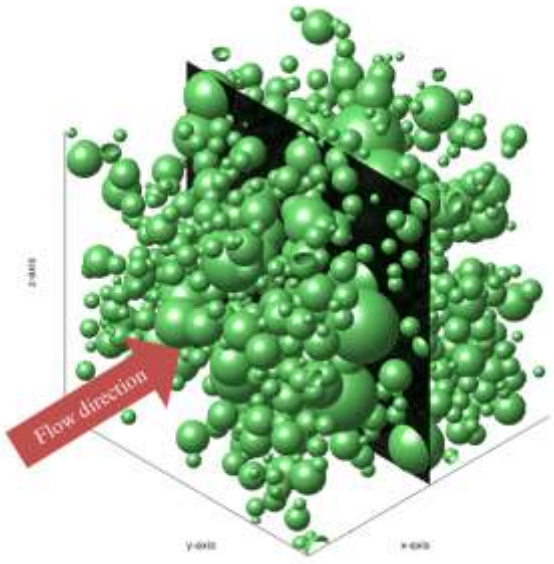

Figure 5.3: Network with mortar placed at the center, normal to the flow (positive x) direction.

Beginning with the solution of the pressure field, physics are added sequentially, verifying accuracy of each solution. For the purposes of testing numerical accuracy, a faster-than-optimal injection rate of 1 mm^3/sec is used in order to propagate a significant amount of species past the mortar during reactive transport (Figure 5.4). Table 5.1 contains a description of each step and records the absolute relative error $err = \left| \frac{v_{single} - v_{mortars}}{v_{single}} \right|$ in macroscopic properties using the finest mortars. The macroscopic error is very low for all cases, although pore merging is the least-accurate module.

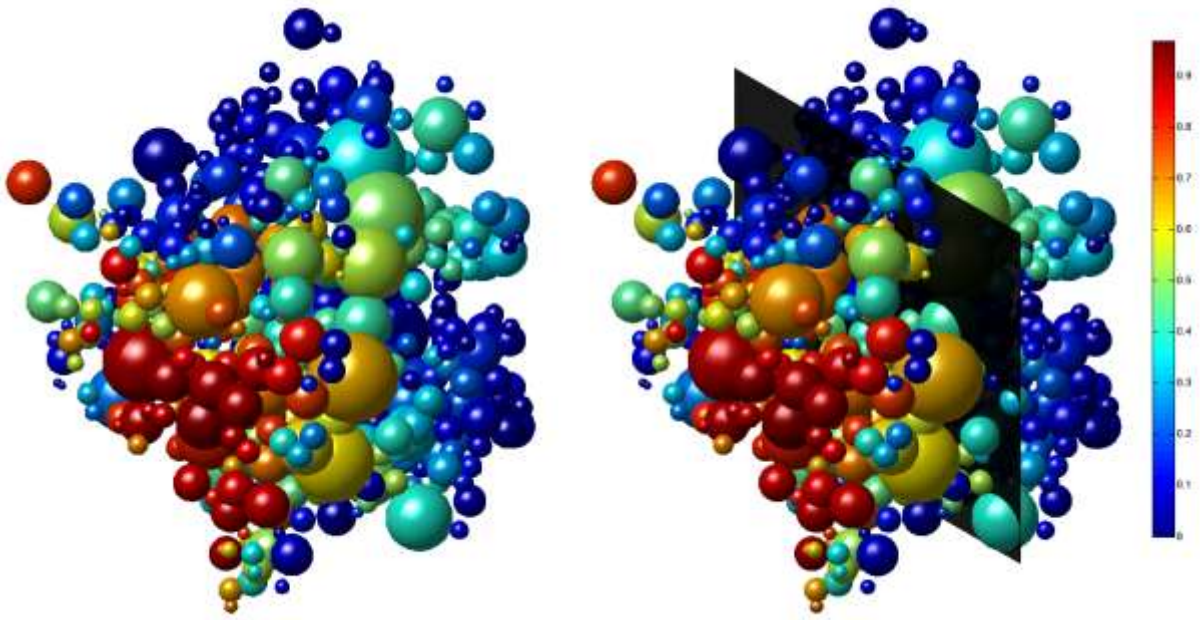

(A) (B)

Figure 5.4: Results for simulations on Pink Desert network with reaction and pore merging enabled after one pore volume injected using infinite mortar resolution. Single Pink Desert (A) and 2×1 mortar solution (B) pore concentrations shown to match accurately across the mortar interface. Image is thresholded to only show pores with c >0.1.

Table 5.1: Comparison of Macroscopic Properties at Infinite Mortar Resolution

Trial description	Macroscopic property	Absolute relative error
1) Pressure and flow field only	Permeability, mD	1.70e-05
2) Nonreactive species transport	Flowing fraction ($PV\ when\ \frac{c_{outlet}}{c_0} = 0.5$)	7.29e-05
3) Reactive species transport	Permeability at 1 PV injected, mD	2.10e-03
4) Pore merging (full simulation)	Pore volumes to breakthrough	6.82e-02

Furthermore, since acidization patterns depend strongly on specific high-permeability channels within the network, the solution accuracy for each trial is also

compared using individual pores as nodes (Figure 5.5). This is to ensure that our mortar technique captures the exact solution at every point and not merely the macroscopic results. Near-perfect agreement is found in every pore for trials 1-3. However, the pore merging algorithm introduces some discrepancy with a few pores. Small deviations in permeability occur along the mortar interface, but the vast majority of pores merge at the expected times.

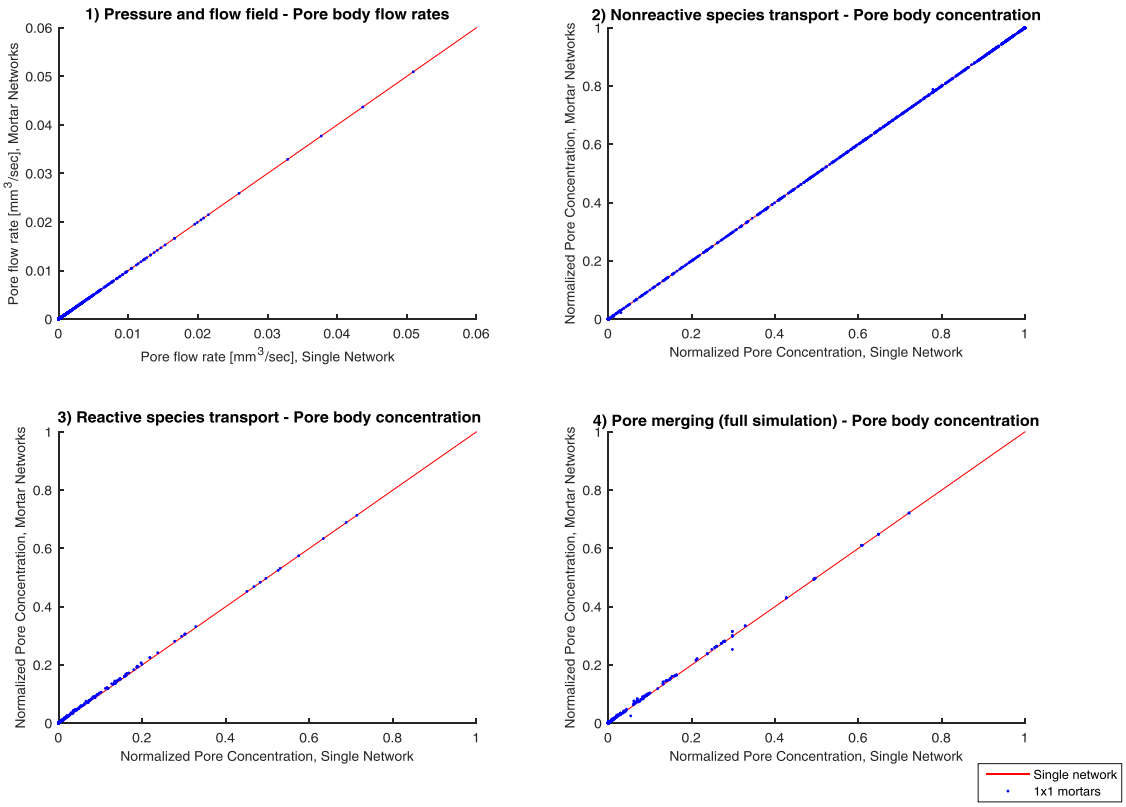

Figure 5.5: Comparison of pore body properties after 1 pore volume injected using infinite mortar resolutions for all four trials at 1 mm^3/sec. Trial 1 compares the pore-body flow rates for solution of the pressure field. Trial 2 compares bore-body concentrations during nonreactive tracers after 1 pore volumes of fluid have been injected. Trial 3 compares pore-body concentrations for advective and reactive transport, but with the pore-merging module disabled. Trial 4 compares pore-body concentrations for the full acidizing simulation, including pore-merging.

Finally, Figure 5.6 compares the full curve of pore volumes to breakthrough versus the inverse Damköhler number. Excellent agreement is found at intermediate and high injection rates, although there is some deviation at slow injection rates where face dissolution occurs. Figure 5.7 provides a visual representation of face dissolution, with a much larger pore in the inlet subdomain. Because this pore cannot "cross" the mortar,

more dissolution is concentrated at the front end of the network, magnifying the face dissolution pattern. A possible remedy is to disable reaction and growth in sufficiently large pores to allow species to penetrate through the network, but error in predicted pore volumes to breakthrough is low and capturing face dissolution regimes accurately is of low importance to prediction of the optimal injection rate. At higher-than-optimal injection rates, discrepancies between the mortars and single networks are attributable to more uniform dissolution. Specifically, acid saturates the entire network quickly and a significant amount of pore growth and merging occurs along the mortar boundary where the most error is expected. Nonetheless, prediction of permeability response for intermediate rates (wormholing regime) is almost perfect.

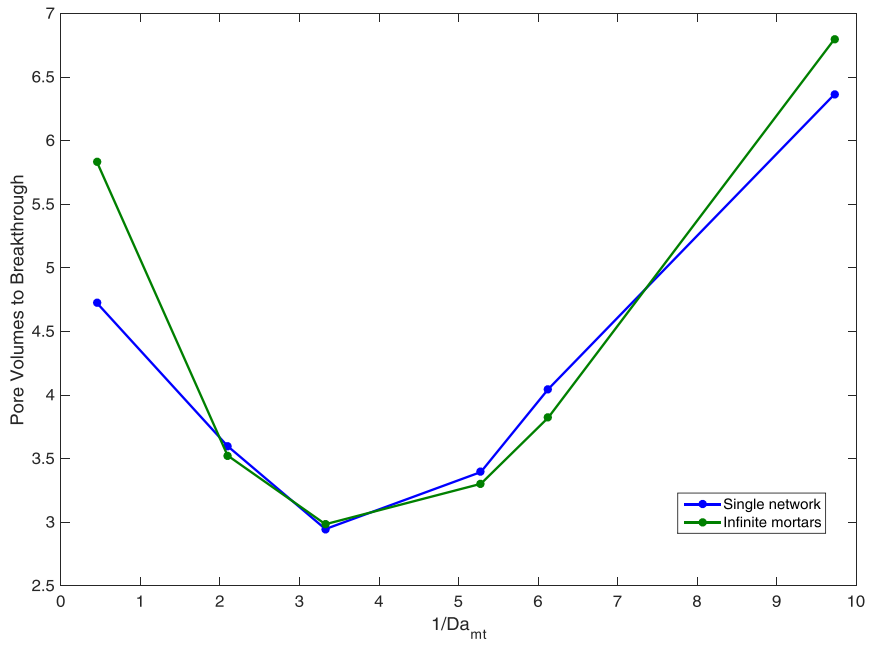

Figure 5.6: Pore volumes to breakthrough comparison for single network and mortar solution.

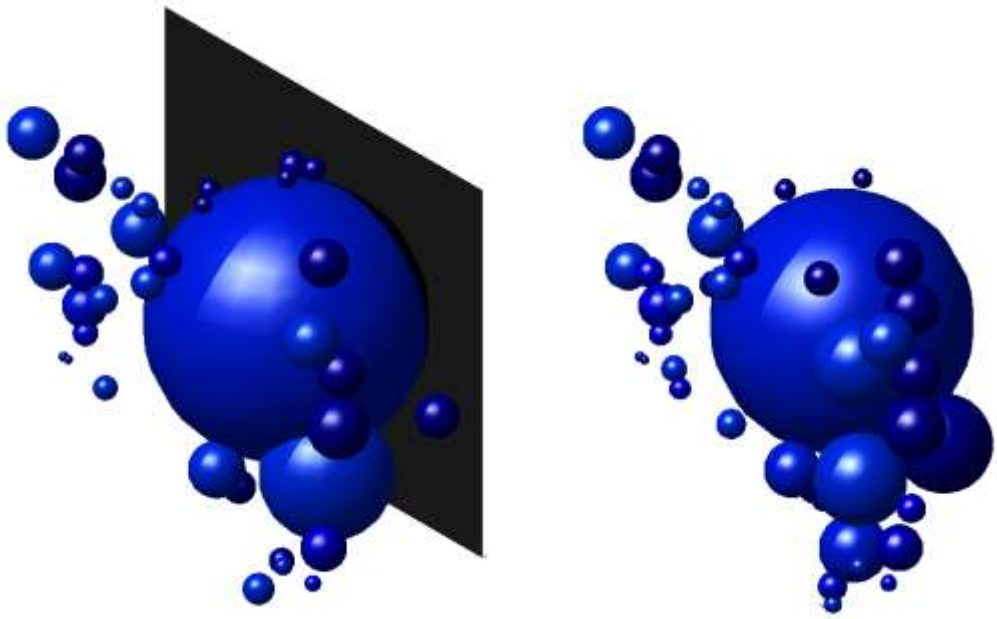

(A) (B)

Figure 5.7: Thresholded concentration plot showing pores with $c > 0.1$ at "breakthrough". Injection at q = 0.01 mm^3/sec. The mortar solution (A) contains more extreme face dissolution because large inlet pores are not allowed to extend past the mortar boundary.

5.4. EFFECT OF MORTAR RESOLUTION

Qualitatively, increasing mortar resolution "loosens" the network connections at the mortar interface, increasing permeability and allowing species from one throat outlet to access many pores. Table 5.2 shows the effect on initial permeability and flowing fraction for different mortar resolutions. Figure 5.8 shows a tracer comparison using different mortar resolutions, showing significantly increased flowing fraction and tailing.

Table 5.2: Comparison of initial permeability and flowing fraction between for varying degrees of mortar coarseness

Simulation type	Initial permeability (mD)	Flowing fraction
Single network	385	0.69
Infinitely fine mortars	385	0.69
9×9 mortars	390	0.68
3×3 mortars	438	0.72
1×1 mortars	451	0.86

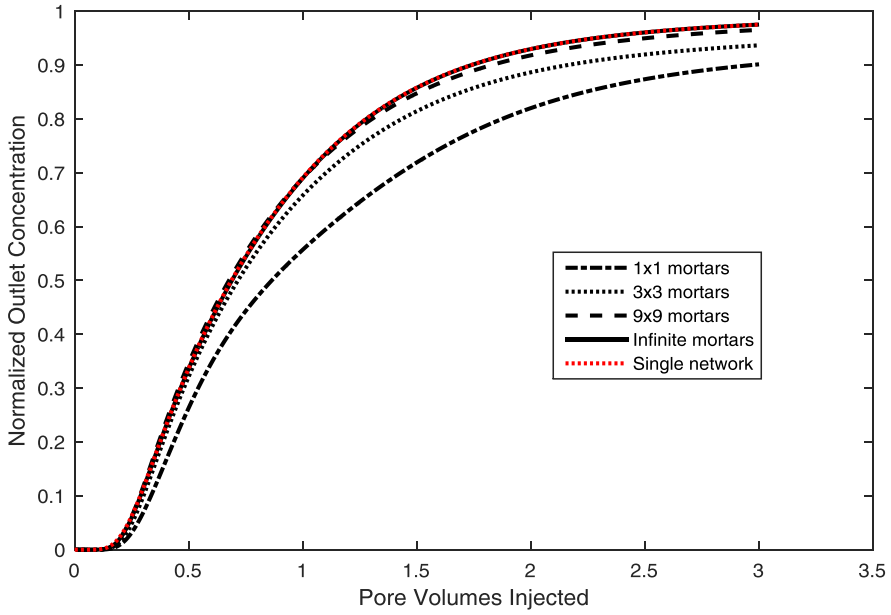

Figure 5.8: Tracer comparison between simulation as a single network and using mortars on Pink Desert Carbonate. Lines intersect one another almost perfectly.

Similarly, when reactive transport is enabled (without merging), the permeability values are shifted upwards by an approximately constant amount (Figure 5.9) as seen in the original permeability measurements (Table 5.2). The error seems to be entirely described by increases in permeability, indicating that species consumption somewhat corrects the errors in advective transport introduced by mortars.

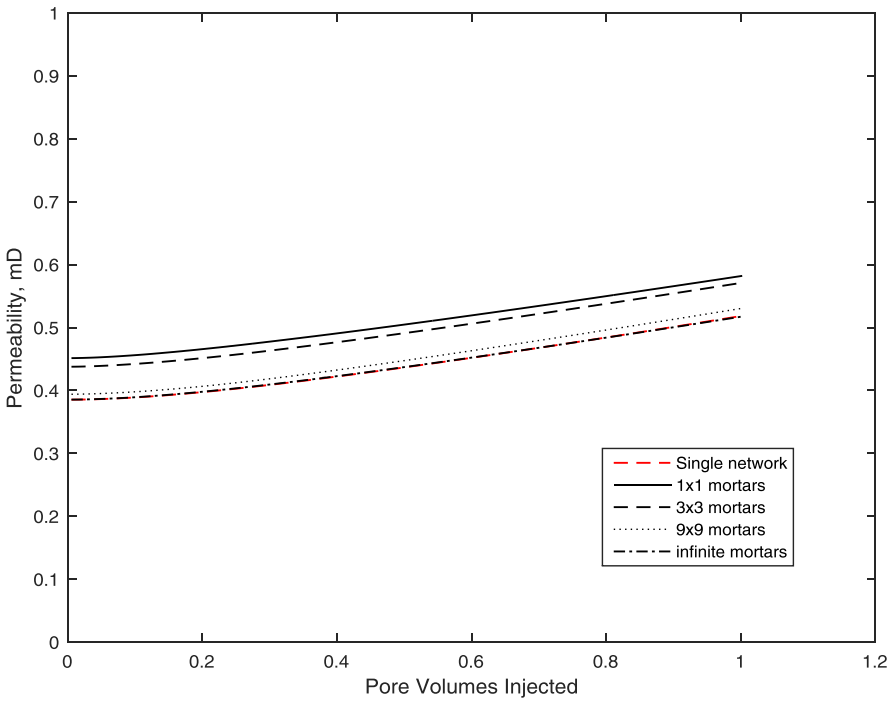

Figure 5.9: Permeability response for reactive transport with pore merging disabled. Qualitative trends remain the same, although coarsening mortars increase permeability as expected.

Finally, in Figure 5.10, the full acidization simulation shows a tendency to increase the number of pore volumes to breakthrough as the mortars are coarsened. In the most extreme case for a 1×1 grid, 5.1 pore volumes are needed to breakthrough compared to 4.5 for the single-network case. Simulations tend to be very accurate regardless of mortar size at early stages of injection, but trend steadily apart as the simulation progresses. The primary cause of error seems to be delay in pore merging. Permeability is a very strong function of pore-merging, often creating steep jumps in permeability. Pore-merging is entirely a function of pore-size, which depends mostly on species transport.

The large errors seen in the nonreactive tracers (Figure 5.7) are likely the primary contributor to inaccuracy using coarse mortars.

However, finer mortar resolutions are very accurate compared to the single-network solution. There is no appreciable difference between infinite resolution and 9×9 resolution. The 3×3 and 1×1 cases are also very accurate for the first 4 pore volumes, indicating a high degree of reliability for all mortar methods. While the deviations at 5+ pore volumes become significant, it is important to remember that the current injection rate ($1mm^3/sec$) was chosen specifically to maximize errors. Most simulations and intermediate rates will "breakthrough" long before this point.

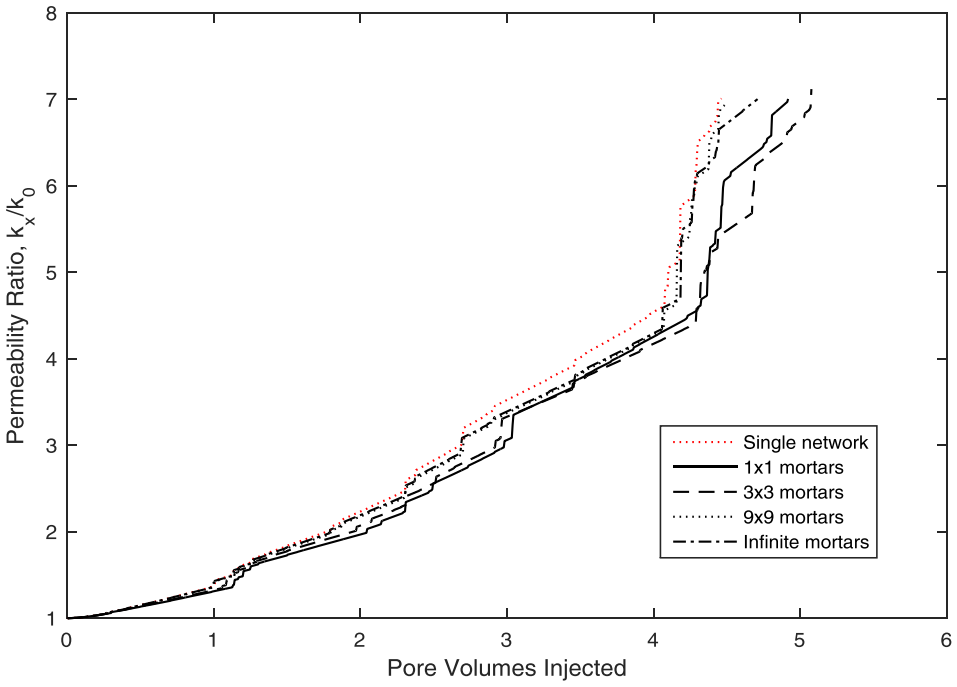

Figure 5.10: Permeability response for full acidization simulation with pore merging.

5.5. DISCUSSION

Mortar coupling is an effective method to decompose networks into subdomains, even at coarse mortar resolutions. Acidization simulations are shown to be accurate across a large range of injection rates, particularly in the intermediate wormholing regime. Errors become magnified at very fast or very slow injection rates.

More accurate description of the face dissolution regime would be possible if pore merging across boundaries were implemented. Very large pores are currently not allowed to cross boundaries, thereby limiting species propagation and permeability-increases through the mortar space. However, pore merging across boundaries was not included due to concerns about retaining parallelizability and efficient scaling of code. Merging across boundaries requires complicated communication between subdomains, as well as iterated internal restructuring. A better solution to this problem of advanced network dissolution is presented in chapter 6, whereby networks can be replaced by Darcy scale grid blocks under certain conditions.

Similarly, errors at fast injection rates are due to disallowance of pore merging across boundaries. Fast injection increases concentration (and therefore dissolution/merging) at the boundary. However, the level of error created at fast injection rates is smaller than seen at slow injection rates. Additionally, since interface concentration approaches a homogeneous maximum at sufficiently fast flow rates, the error ought to remain static above this threshold.

Chapter 6: Hybrid modeling and two-scale continuum modeling of matrix acidization

6.1 INTRODUCTION

In chapters 3 and 4, it was hypothesized that some shortcomings of pore network models could be attributed to their small domain size relative to core-scale experiments. Here, we test this hypothesis using the mortar coupling technique developed and verified in chapter 5. Multiple networks are coupled together to compose a larger domain. However in large-scale simulations, significant parts of the domain remain unreactive, and computation in these regions is largely wasted. Therefore, a hybrid modeling technique is developed to replace the relatively complex network model physics with a more compact continuum scale blocks in nonreactive regions. The hybrid model is shown to significantly decrease computation time in acidizing simulations while maintaining excellent quantitative accuracy when compared to the networks-only solution.

Furthermore, a two-scale continuum model is developed and generalized with novel permeability-porosity relationship and mass transfer coefficient obtained from a single network model. This approach is shown to have poor levels of accuracy under intermediate local injection conditions, and is therefore unsuitable to entirely replace pore network models when the local Damköhler number is greater than 0.06. However, two-scale continuum models perform well outside of this criterion, and large scale simulations of acidization are conducted. The key result is that pore volumes to breakthrough are lowered while preserving the optimal macroscopic Damköhler number of injection. The two-scale continuum model is also used to model acidization in radial flow, and the pore

volumes to breakthrough curve is shown to be relatively insensitive to fast injection rates, lending support to the field practice of matrix acidizing using maximal rates.

6.2. MODEL DEVELOPMENT

6.2.1. Darcy block hybrid model verification

The goal of this chapter is to develop techniques to simulate matrix acidization at large scales using pore network models. The mortar coupling technique developed in chapter 5 is sufficient to couple a theoretically unlimited number of network models together (Figure 6.1).

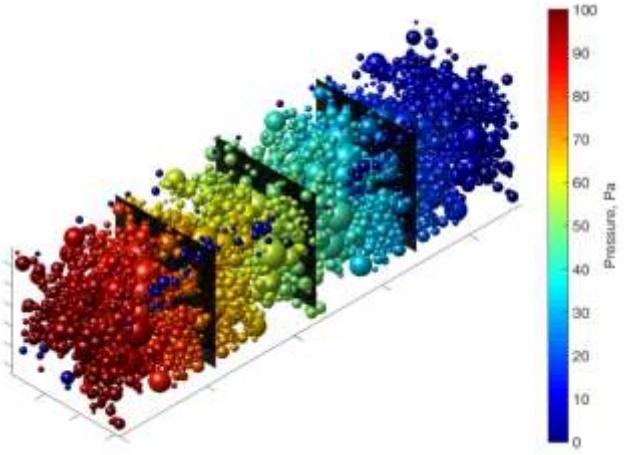

(A)

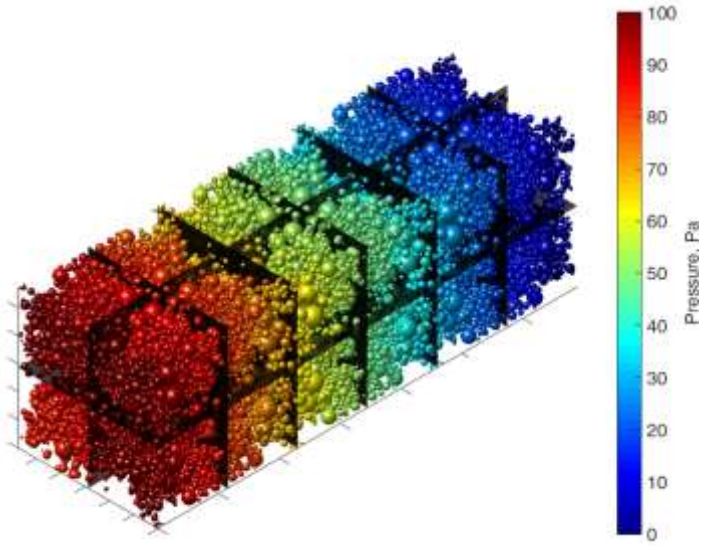

(B)

Figure 6.1: Pressure fields for 4 networks (4×1) (A) and 24 networks (6×2×2) (B) networks joined together using mortar coupling.

At first appealing for its simplicity, this method has the drawback of simulating computationally costly physics in many static subdomains. At early time and during slow

injection rates, acid is consumed before it can penetrate deeply into the core. Therefore, large-scale simulations of acidization are likely to contain significant non-reactive regions.

Mortar coupling techniques allow different physics and solvers to be utilized on each subdomain. A hybrid method is proposed, whereby network models describe regions of complex dissolution, while a simplified Darcy scale model is used in regions far from areas of active dissolution. For example, in the case of 4×1 networks above, networks far from the inlet could be initially "turned off" and modeled as Darcy blocks whose macroscopic permeability matches the network permeability (Figure 6.2). As the simulation progresses, the remaining blocks are turned on sequentially once their concentration exceeds a small threshold (Figure 6.3). Because simulations are carried out in the intermediate wormholing regime (Da_{mt} = 0. 30), most subdomains are eventually modeled as active networks. Total-domain permeability response is recorded in Figure 6.4, and the method shows excellent agreement with the network-only simulation.

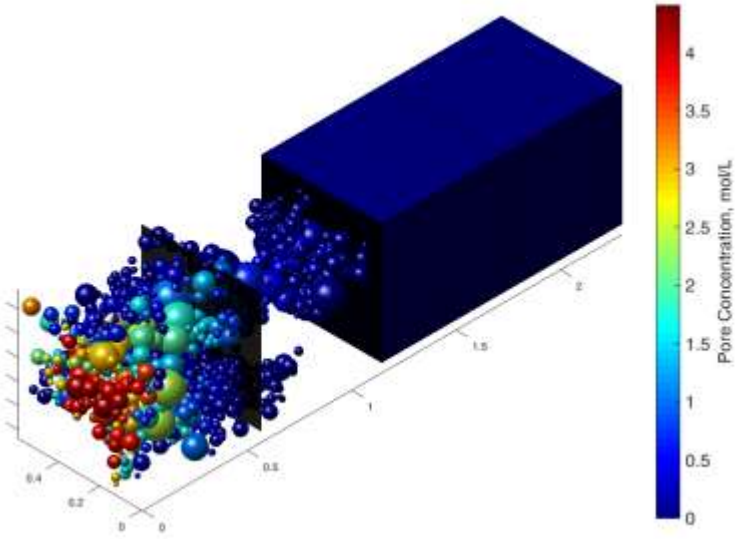

Figure 6.2: Hybrid simulation at intermediate time for 4×1 configuration. First two inlet blocks are represented by network models. Last two blocks are represented by Darcy-scale blocks where the concentration is below threshold.

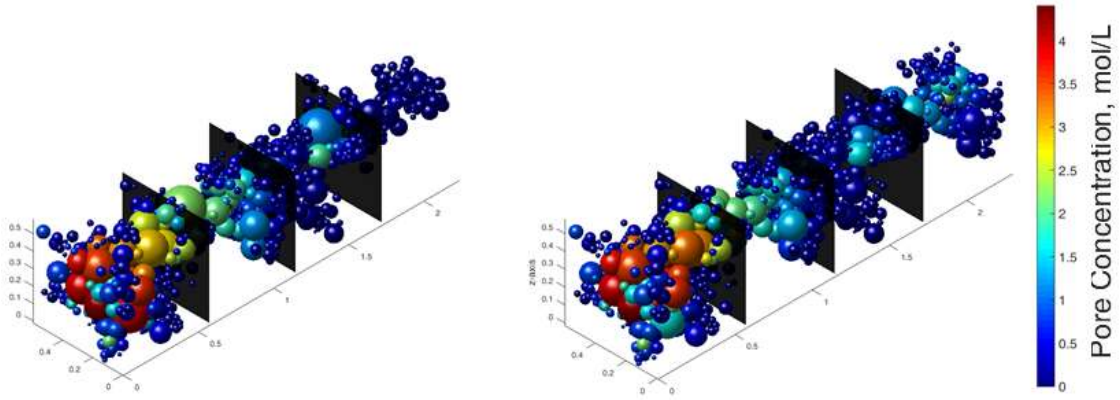

Figure 6.3: Comparison of networks-only simulation (A) to hybrid method using Darcy-scale blocks in nonreactive regions (B). Node heat shows pore concentration. Both simulations visualized at breakthrough for $Da_{mt} = 0.30$ (optimum).

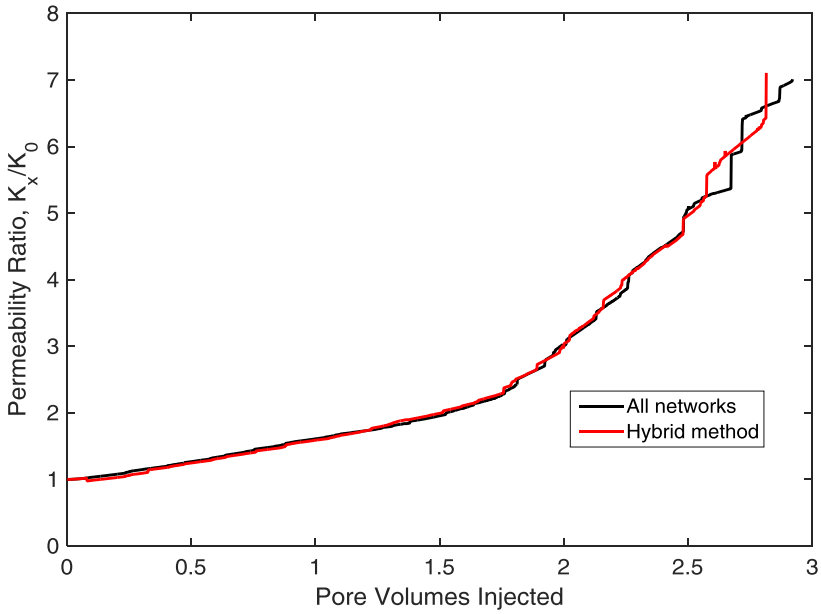

Figure 6.4: Comparison of permeability vs. pore volumes injected for 4×1 networks-only and hybrid model using Darcy-scale blocks in nonreactive regions.

With the current method, there is little advantage gained in simulating rapid injection rates, as acid will saturate the networks very quickly and the current hybrid method with collapse into a networks-only simulation. Therefore, there is a narrow range of utility gained by the introduction of Darcy-scale blocks in nonreactive regions. Only slow and intermediate injection rates are efficient. Figure 6.5 shows acidization simulation for 6×2×2 subdomains at $Da_{mt} = 0.30$. Pore volumes to breakthrough are 4.83, slightly higher than seen in the single-network case. In section 2.7.1, it was hypothesized that larger domain sizes would reduce the number of pore volumes to breakthrough. Here, a very similar result is found with 24 networks compared to a single network at the

optimal injection rate, and is therefore likely still below a representative elementary volume.

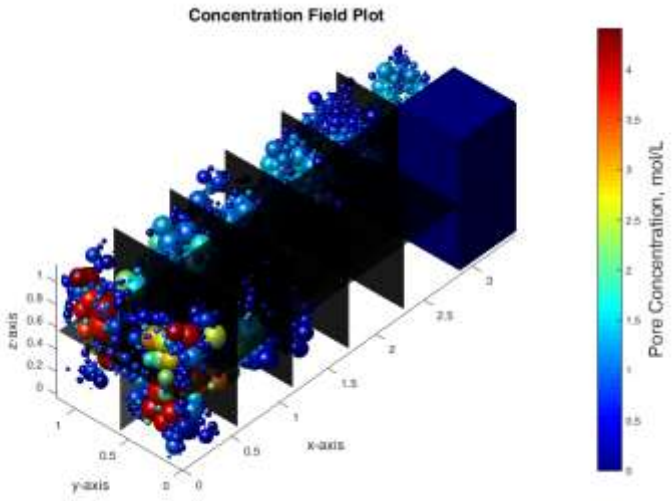

Figure 6.5: Hybrid model for 6×2×2 subdomains at Da_{mt} = 0.30 (Q = 1.2 mm^3/sec), visualized at breakthrough. Two completely nonreactive subdomains remain, and are modeled as Darcy scale blocks.

Figure 6.6 shows acidization at a much slower injection rate (Da_{mt} = 2.22). Simulations were conducted out to 8 pore volumes injected, achieving a permeability increase of 20%. Breakthrough is likely delayed substantially by the inability of pores to merge across boundaries.

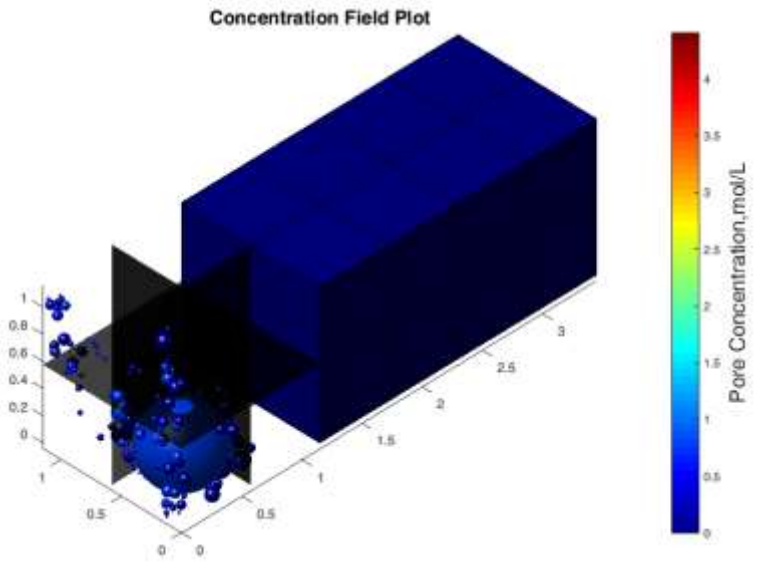

Figure 6.6: Hybrid model for 6×2×2 subdomains at Da_{mt} = 2.22 (Q = 0.12 mm_3/sec), visualized at breakthrough. Most blocks remain nonreactive Darcy scale block. However, pores at inlet are unable to merge across boundaries, leading to over-exaggerated face dissolution.

6.2.2. Hybrid method with two-scale continuum model

The strategy above in 6.2.1 does not require description of reaction in continuum scale blocks, as only solution of the pressure field (Eqn 2.8) is required. Here the hybrid method is extended to become a true "two-scale continuum" (TSC) model, including physics describing mass transfer and permeability evolution.

Modeling rapid injection rates at large scales is very inefficient with pore network models, as expensive pore network physics must be modeled in virtually all of the domain. Fortunately, because rapid injection rates saturate networks homogeneously, it is hypothesized that network models are not required to provide a fine-scale description of species distribution and matrix dissolution.

Two-scale continuum models have been shown to be quantitatively accurate at capturing acidizing experiments (Panga et al., 2005; Maheshwari et al., 2013). Maheshwari et al. (2013) utilized a dimensionless mass transfer coefficient developed for ducts by Balakotaiah and West (2002),

$$Sh = Sh_{\infty} + 0.7\,\mathrm{Re}_p^{1/2}\,Sc^{1/3} \qquad (6.1)$$

where Sh_{∞} is the asymptotic Sherwood number, Re_p is the pore scale Reynolds number, and Sc is the Schmidt number. This mass transfer coefficient is coupled with assumptions about pore geometry and surface area available to flow. They also utilized a semi-empirical permeability/porosity relationship based loosely on the Kozeny-Carman relationships (Eqns 2.10, 2.11). This assumption is particularly problematic, as we have shown in chapter 3 that permeability response depends strongly on flow rate and is not a static function of porosity. Therefore, a two-scale continuum model whose input parameters are a function of local Damköhler number is both useful for our current application and a novel way of addressing the key weaknesses of past two-scale continuum models.

Here, correlations for the mass transfer coefficient, permeability-porosity relationship, and surface area are developed. These parameters, which must normally be approximated or inferred from experimental data, are obtained *a priori* from a Pink Desert network. The underlying philosophy is to assemble a large amount of information from a pore network model into compact upscaled correlations. Simulations are performed on a Pink Desert network at multiple characteristic Damköhler numbers

(corresponding to 0.01-10 mm^3/sec) to obtain inputs as ongoing functions of local flow rates and dissolution levels. The permeability-porosity relationship is described by:

$$\frac{k}{k_0} = e^{(c_1(\phi-\phi_i))}, \phi < \phi_{bt} \quad (6.2)$$

$$\frac{k}{k_0} = (e^{(c_1(\phi-\phi_i))} - 1) + e^{(c_1(\phi-\phi_{bt}))}, \phi \geq \phi_{bt} \quad (6.3)$$

where ϕ_i is initial porosity, while c_1, c_2 and ϕ_{bt} are fitted functions of local network Damköhler numbers (Table 6.1) (Figure 6.7). The need for a piecewise continuous function arises from the abrupt increase of speed in permeability growth that occurs after "breakthrough". Note that ϕ_{bt} occurs at a similar point to the breakthrough as defined in previous chapters, but differs slightly here as a fitting parameter.

Comparison is made to the permeability-porosity relationship (Eqn 2.11) employed by Panga et al (2013) and Maheshwari et al. (2013), who assumed $\gamma = \beta = 1$. This modified Kozeny-Carman model predicts permeability to be significantly less than what is observed in the Pink Desert carbonate network simulation. As a function of porosity and rock type alone, it also does not predict the extreme variations in permeability growth for different Damköhler numbers.

Table 6.1: Fitted coefficients for permeability-porosity relationship for Pink Desert

Da_{mt}	c_1	c_2	ϕ_{bt}
2.22	8.10	47.51	0.41
0.48	29.24	183.43	0.27
0.10	39.37	284.79	0.30
0.02	26.03	497.46	0.34

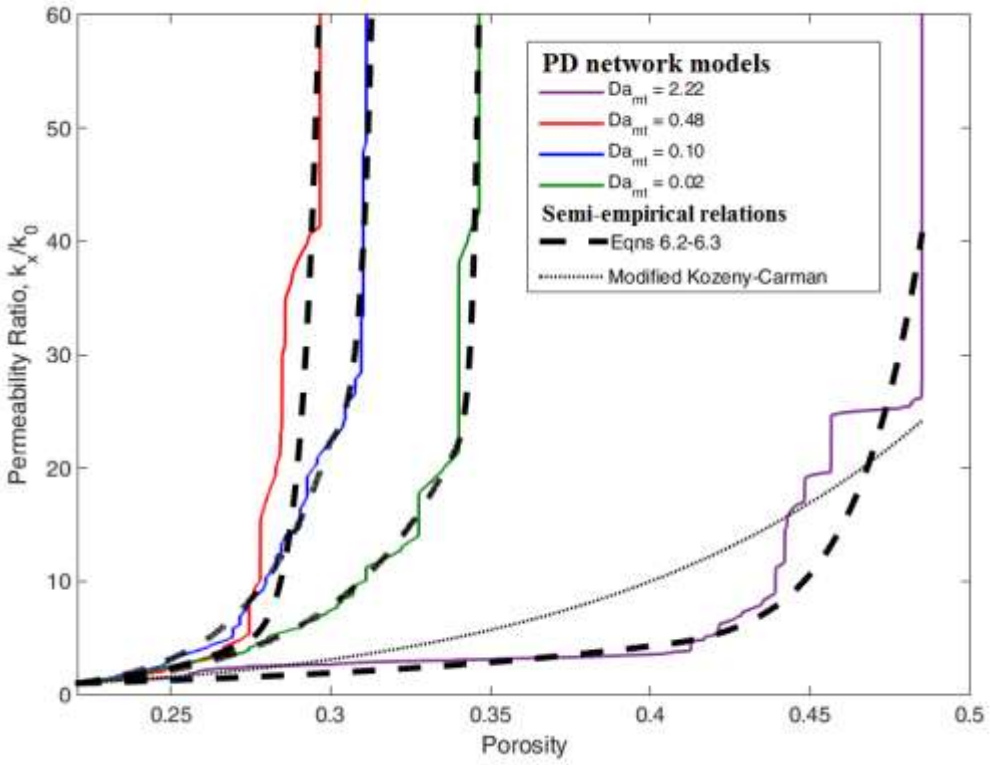

Figure 6.7: Permeability increase as a function of porosity for different dissolution regimes. Curves fit from Eqns 6.2-6.3 using parameters in Table 6.1 are shown as black dashed lines. Modified Kozeny-Carman equation used by Panga et al (2013) and Maheshwari et al. (2013) shown as fine black dots.

The mass transfer coefficient (defined in Eqn 3.11) tends to decrease with increasing porosity (dissolution). Initial values for mass transfer are heightened because the bulk concentration of the network is very low at early times. Oscillations in calculated mass transfer coefficient occur because pore merging does not preserve surface area. A simple exponential expression is used to describe mass transfer (Eqn 6.4),

$$K_{mt} = c_3 e^{c_4 \phi} \qquad (6.4)$$

where c_3 and c_4 are fitted parameters given in Table 6.2. The comparison with network values is shown in Figure 6.8. The expressions tend to underestimate mass transfer at early porosity values for very fast and very slow injection rates. More complicated expressions could capture these windows better, but simpler expressions are preferred in order to avoid over-fitting.

Table 6.2: Fitted coefficients for macroscopic mass-transfer coefficient for Pink Desert

Da_{mt}	c_3	c_4
2.22E+00	1.29E-06	-1.32E+01
4.77E-01	2.81E-05	-2.17E+00
1.03E-01	2.54E-06	-9.50E+00
2.22E-02	2.88E-07	-1.63E-01

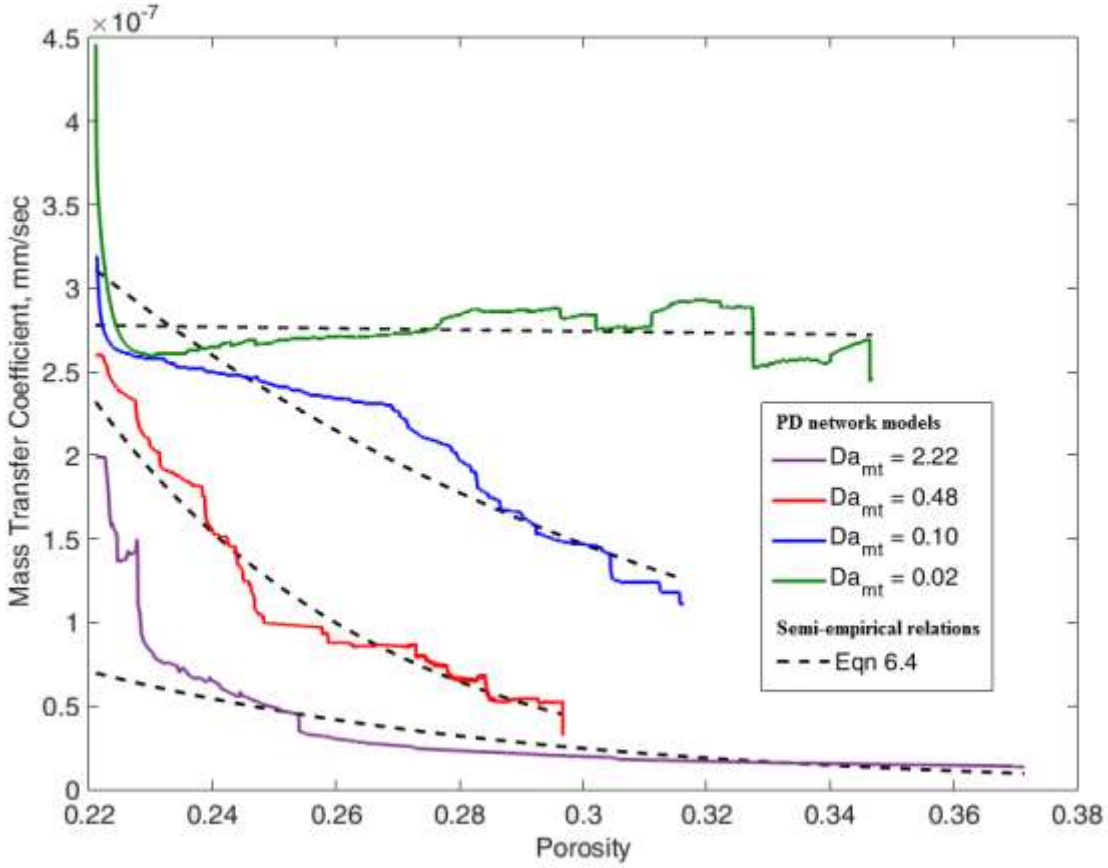

Figure 6.8: Mass transfer coefficient versus porosity for different Damköhler numbers. Curves fit from Eqn 6.4 using coefficients in Table 6.2 are shown in black dashed lines.

Finally, the change in reactive surface area is recorded during network simulation. It tends to increase almost linearly with porosity, which is expected since surface area grows linearly with pore volume in the network model (see section 3.2.2.4) assuming constant pore compactness (Eqn 3.2.3). Therefore, a linear relationship is used to relate surface area, a_v, and porosity change (Eqn 6.5),

$$a_v = c_5\phi + c_6 \quad (6.5)$$

where c_5 and c_6 are fitted parameters given in Table 6.3. There are significant differences in how total surface area changes at different Damköhler numbers (Figure 6.9). Surface area grows at fast and intermediate injection rates, since many pores are contacted with acid and grow at similar rates. Conversely, surface area is slowly lost in the face dissolution regime, as pore-merging of a few large pores at the inlet are the primary aspects of dissolution. In all cases, oscillations are due to pore merging, which conserves volume but not surface area.

Table 6.3: Fitted coefficients for change in surface area for Pink Desert

Da	c5	c6
2.22E+00	-1.08E+00	8.39E+00
4.77E-01	1.44E+01	4.90E+00
1.03E-01	2.11E+01	3.44E+00
2.22E-02	2.29E+01	3.00E+00

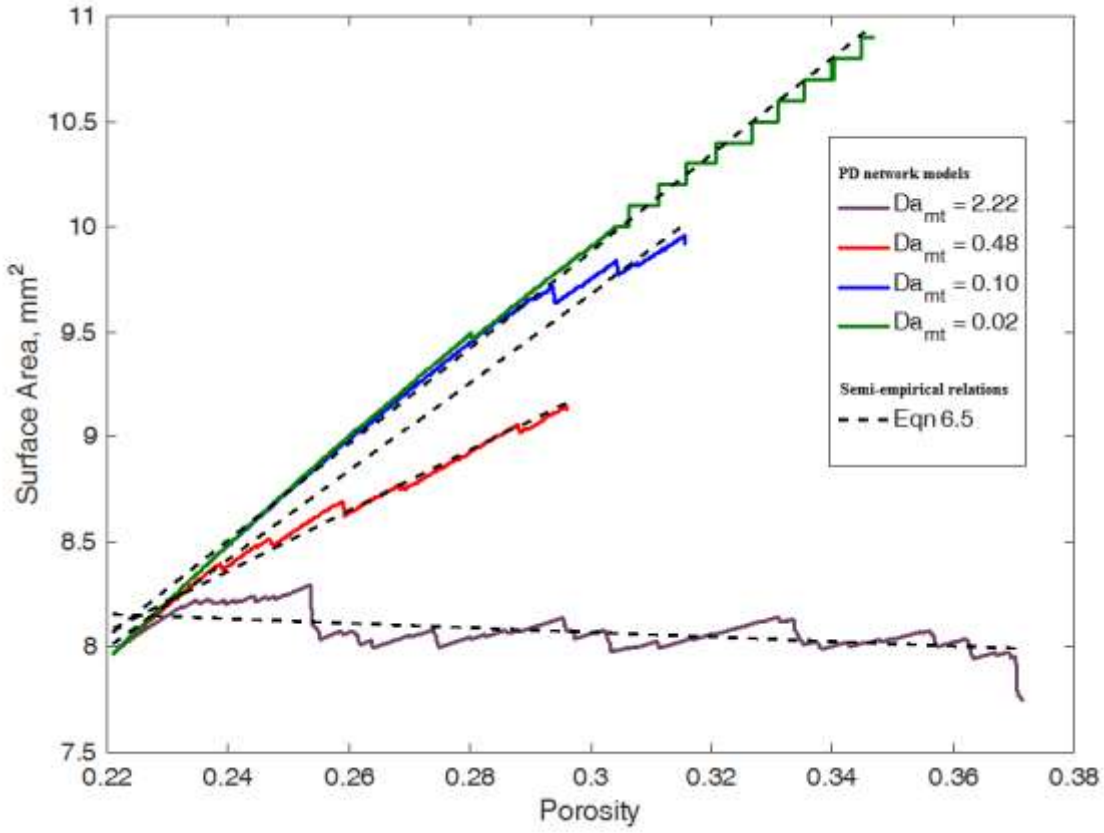

Figure 6.9: Surface area versus porosity for different Damköhler numbers. Curves fit from Eqn 6.5 using coefficients in Table 6.3 are shown in black dashed lines.

Eqns 6.2-6.5 all contain coefficients for specific Damköhler numbers. In simulation, a linear interpolation of these coefficients is taken for the specific local Damköhler number of the Darcy Scale block with hard caps set at specific limits (for example, to avoid negative mass transfer). Furthermore, because of the evolving nature of simulations, it cannot be expected for grid blocks to maintain a static local Damköhler number. Therefore Eqns 6.4 and 6.5 are implemented in derivative form, such that changes in permeability and surface area correspond to increments of porosity increase as

a function of local Damköhler number. The major assumption behind this method is that changes in mass transfer rate and geometry are well-approximated as history independent. This assumption is not likely to lead to large amounts of error. For example, the normalized permeability to porosity ratios at Da_{mt} = 2.22 and 1.03 are $\frac{dK_{ratio}}{d\phi} = 37.0$ and 39.4 respectively at early times. Major changes in structure-property relations occur primarily at advanced stages of dissolution.

Comparisons are made to the 4×1 "all-networks" case in section 6.2.1. Simulation using entirely two-scale continuum blocks is conducted. Failure of the two-scale continuum model to accurately predict permeability response in the wormholing regime is shown in Figure 6.10. Permeability matches at early pore volumes, but once species is propagated significantly past the first subdomain, permeability plateaus. Individual block permeabilities are shown in Table 6.4, where the inlet block's permeability has increased by a factor of more than 1000, while the rest of the blocks show extremely modest dissolution.

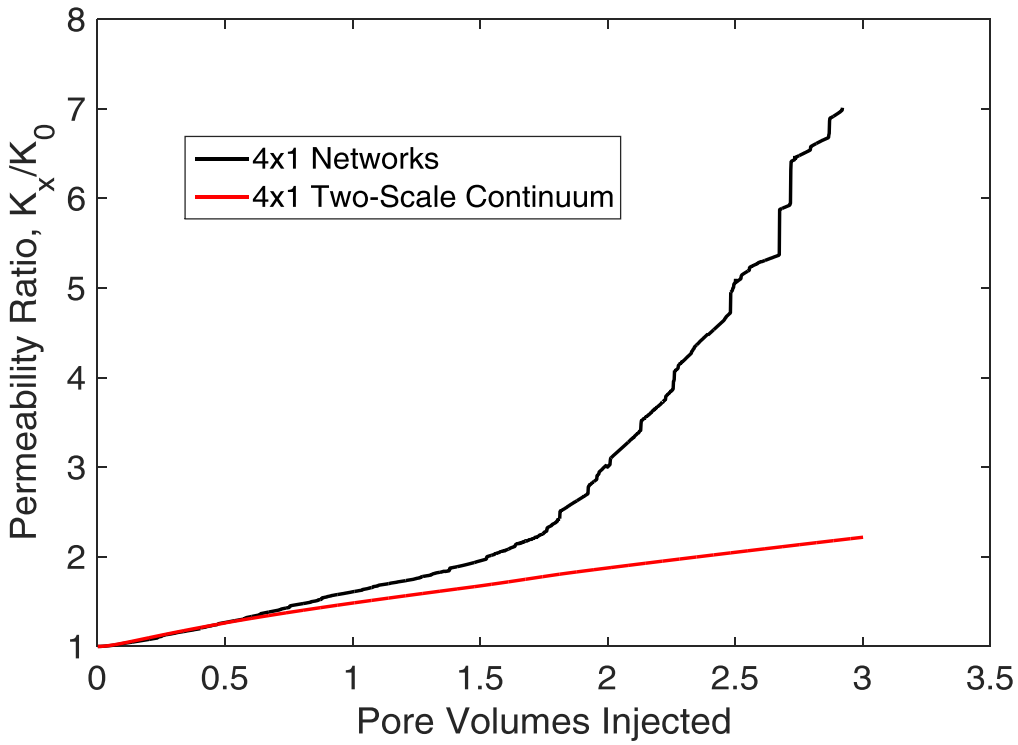

Figure 6.10: Permeability response in networks-only and two-scale continuum model of acidization in 4×1 subdomains of Pink Desert carbonate for Da_{mt} = 0.30

Table 6.4: Individual block permeabilities for two-scale continuum model at Da_{mt} = 0. 30 and 3 PVI

	Block permeability ratios
block 1 (inlet)	1250.00
block 2	5.83
block 3	1.44
block 4 (outlet)	1.07

The hypothesized shortcoming of the two-scale continuum model is that block response is highly sensitive to internal block boundary conditions. For example, in the networks-only simulation, the species distribution between the first and second block is

highly heterogeneous (Figure 6.11). This likely contributes to enhanced wormholing in pore-network models, as the acid input is concentrated in a small area that easily forms a new dominant pathway. Conversely, in the two-scale continuum description, the boundary conditions on the second block are homogeneous and dilute. The fitted equations assume wormholing starts "from scratch" and a new dominant pathway must be formed from baseline in each block. This hypothesis is given support by results at faster injection rates, since less species channeling is observed, and the importance of network heterogeneity is reduced. Permeability response for two-scale continuum models matches much more closely with network-only simulations (Figure 6.12).

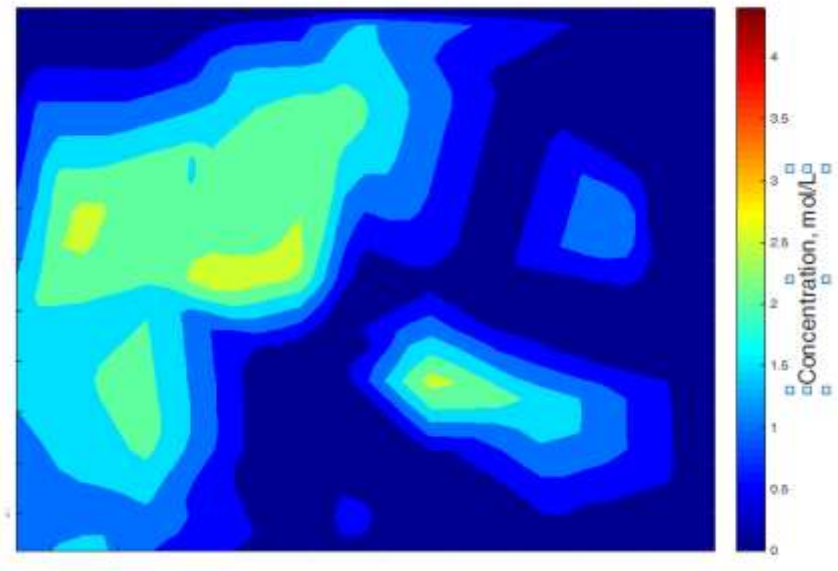

Figure 6.11: Species concentration at interface between blocks 1 and 2 for networks-only simulation at breakthrough.

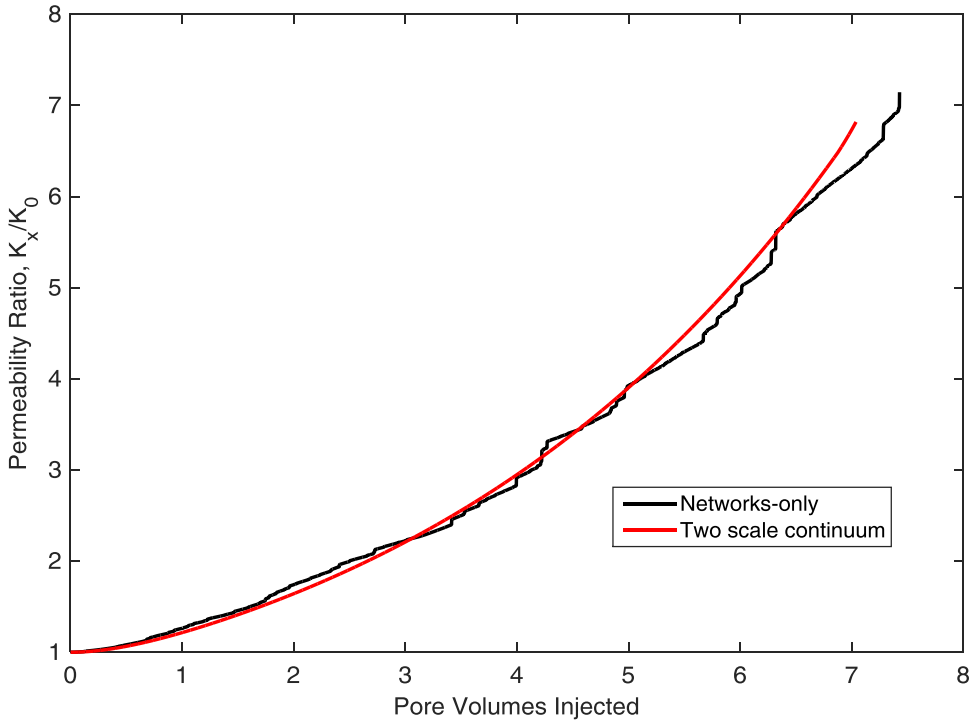

Figure 6.12: Permeability response in networks-only and two-scale continuum model of acidization in Pink Desert carbonate for $Da_{mt} = 0.06$

6.3 TWO-SCALE CONTINUUM MODELING OF CARBONATE ACIDIZATION

For sufficiently fast injection rates, nearly all subdomains will be at a small enough local Damköhler number that the two-scale simulation approach ought to be accurate without any pore network models (Figure 6.10). Compared to previous hybrid simulations using network models, a pure two-scale continuum simulation is extremely fast to simulate. Unfortunately, while the two-scale continuum model gives an excellent match for the 4x1 case, the two-scale continuum physics begin to show severe limitations at intermediate domain sizes. For example, the optimal injection rate is hypothesized by

Fredd and Fogler (1999) to be independent of domain cross section, under the assumption that a wormhole will form and ignore most of the domain area. Near-identical permeability response is produced when the injection rates are scaled linearly with domain length and surface area using the test-case at 4×1×1 and Da_{mt} = 0. 06 as a baseline (Table 6.5). Changes in pore volumes to breakthrough are due to small changes in local Damköhler number (Eqns 6.2-6.5). Permeability in all blocks is unperturbed in order to demonstrate identical breakthrough in comparative cases. Varying permeability according to a random uniform distribution +/- 10% produces very similar dissolution results (Figure 6.13).

Table 6.5: Pore volumes to breakthrough for two-scale continuum model at linearly-scaled injection rate

Network Dimensions	Injection Rate (mm3/sec)	Domain Damkohler number	Average subdomain Damkohler number	Pore Volumes to Breakthrough
4×1×1	8	6.48E-02	2.57E-02	7.94
4×2×1	16	4.08E-02	2.57E-02	7.94
4×2×2	32	2.57E-02	2.57E-02	7.94
8×2×2	64	2.57E-02	1.62E-02	8.15
8×4×4	256	1.02E-02	1.62E-02	8.15
8×6×6	576	5.94E-03	1.62E-02	8.15
16×2×2	128	2.57E-02	1.02E-02	8.79
16×4×4	512	1.02E-02	1.02E-02	8.79
16×6×6	1152	5.94E-03	1.02E-02	8.79

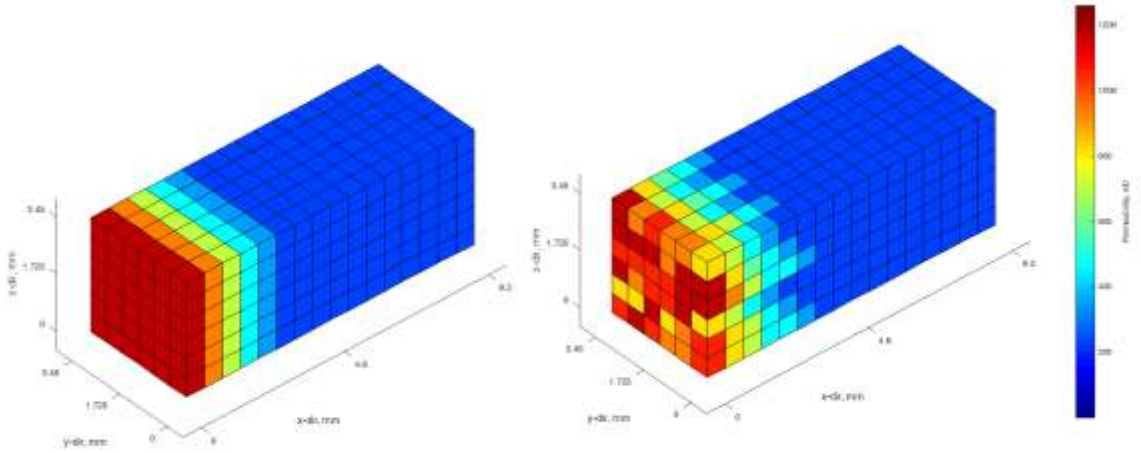

(A) (B)

Figure 6.13: Permeability for 16×6×6 (9.2×3.45×3.45 mm) case at 1152 mm^3/sec. Homogeneous permeability field (A) shows similar dissolution pattern to perturbed permeability field (B). Pore volumes to breakthrough are 8.79 and 8.66 respectively.

The 4×1 case matches network models so well because species channeling is captured by mass transfer and permeability-porosity relationships occurring within a single block. However, for larger cross sections, channeling pathways are interdependent on adjacent subdomains. Emergent pathways seen in network models may have a resolution many times lower than block resolution. Permeability is again uniformly perturbed by +/- 10% in each grid block in order to facilitate initial channeling. This two-scale continuum model is unable to capture channeling at intermediate macroscopic Damkohler numbers (close to 0.29), instead producing consistent face dissolution (Figure 6.14). Inlet blocks do not divert bulk flow into high-permeability pathways, because their local Damkohler number (Da_{mt} = 0.52) is well-outside the Da_{mt} = 0.06 threshold. The homogeneous outlet concentrations produced by two-scale continuum blocks lead to

severe underestimation of species channeling as compared to network models in Figure 6.10.

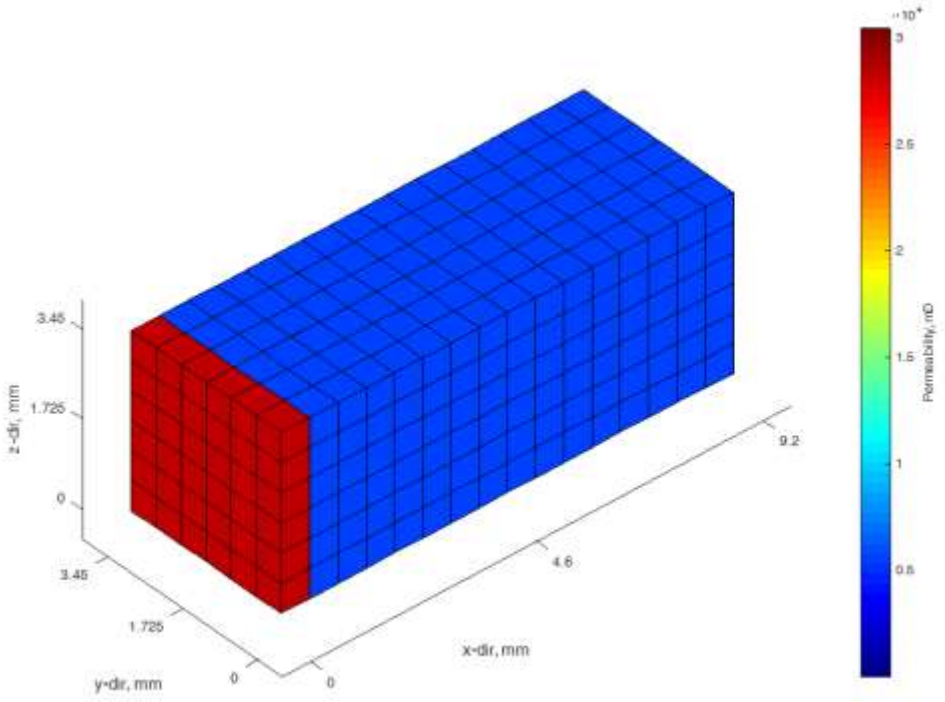

Figure 6.14: Two-scale continuum model at Da_{mt} = 0.30 for 16×6×6 (9.2×3.45×3.45 mm) configuration after 10 pore volumes injected. Local block Da_{mt} = 0.52, far above the regime where two-scale continuum models were shown to be accurate.

Larger domain sizes eventually show emergence of species channeling at sufficiently fast injection rates (Figure 6.15). While the macroscopic injection rates are far higher than expected for wormholing, average local Damköhler numbers are close to the uniform dissolution regime, and thus project species concentrations more accurately. Channeling is a strong function of domain size. However, the quantitative accuracy of

these simulations is very far from the expected value. Simulations were carried out to 20 pore volumes, achieving a macroscopic permeability increase of only a factor of 3. Additionally, the injection rate (12800 mm^3/sec) was almost three orders of magnitude higher than the optimal expected injection rate (15 mm^3/sec).

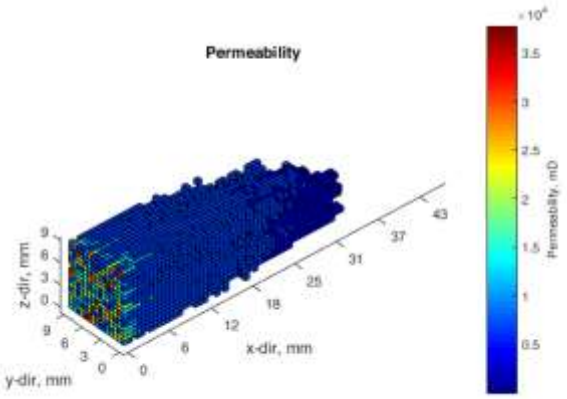

(A)

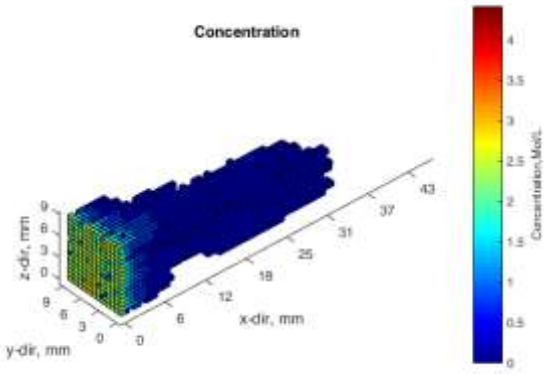

(B)

Figure 6.15: Continued on next page

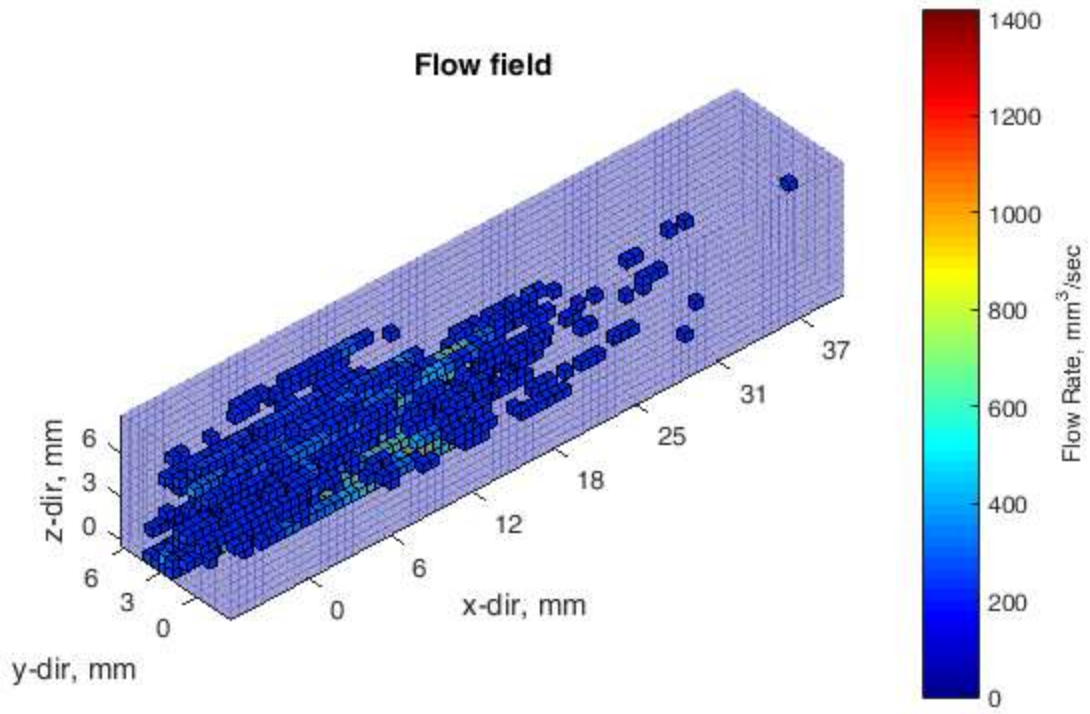

(C)

Figure 6.15: Permeability (A), block concentration (B), and block flow rate (C) for 75×15×15 subdomain TSC simulation. Injection rate is 12800 mm3/sec or Da_{mt} = 0.003. 20 pore volumes have been injected, corresponding to a permeability increase by a factor of 3.

For all domain sizes studied, species does not propagate far into the domain, even at extremely high injection rates. This suggests that the pore-scale mass transfer coefficient, while accurate for a single subdomain, is likely an overestimate at large domain sizes. Block dissolution at larger domain sizes is significantly more pronounced than simulated in a single pore-scale model. For example, permeability increase by a factor of more than 10^6 is observed in some blocks (Figure 6.13A), while permeability

curves for a single network increased by a factor of approximately 50 before increasing exponentially with little change in porosity (Figure 6.7). Therefore, a hard cap on block reaction is introduced once permeability has increased by a factor of 1000. Results show low sensitivity to this cutoff, as extremely small amount of reaction is required to increase local permeability at this level of dissolution. This modification improves quantitative model results drastically (Figure 6.16), capturing channeling in the intermediate wormholing regime for $Da_{mt} = 0.30$ ($15mm^3/sec$).

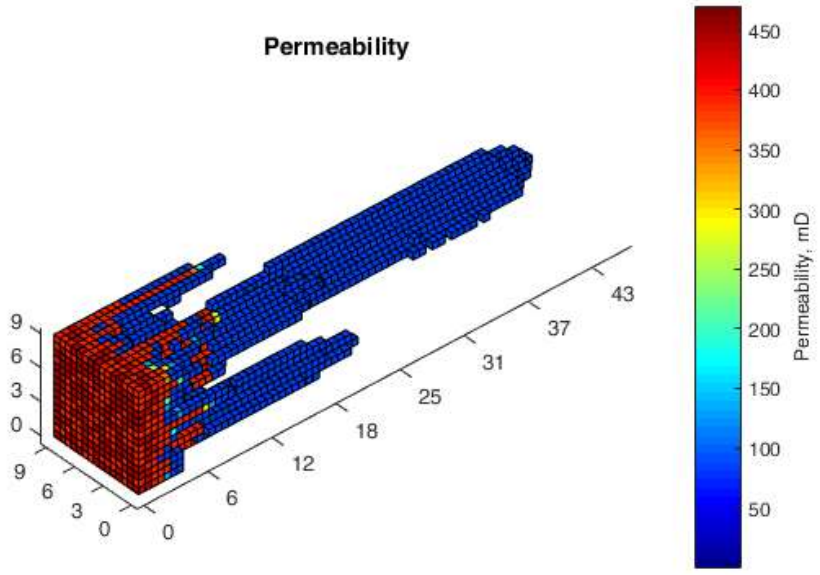

(A)

Figure 6.16: Continued on next page

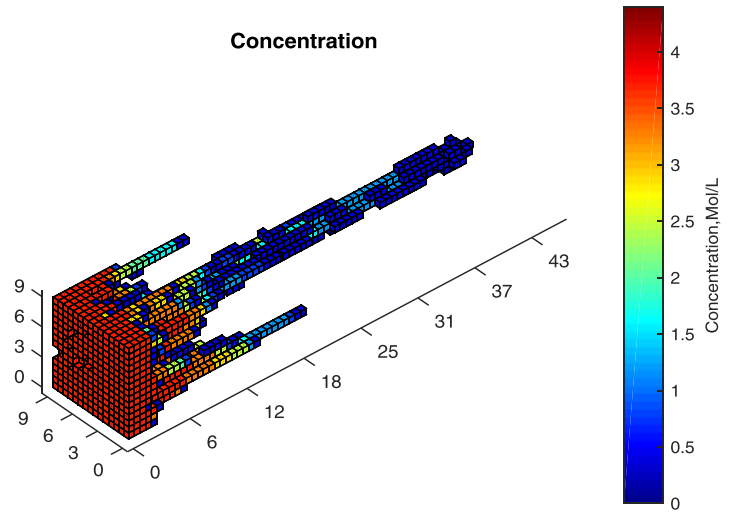

(B)

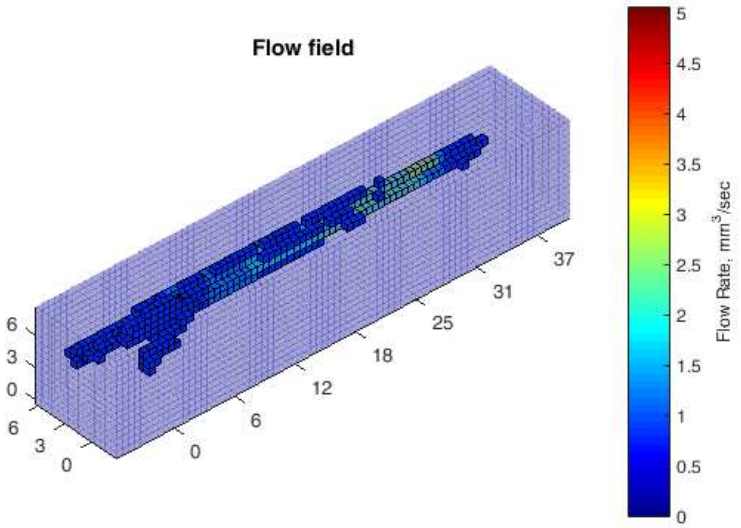

(C)

Figure 6.16: Comparison of 75×15×15 block-length TSC simulations at Damt = 0.30, visualizing breakthrough at 0.39 pore volumes. Permeability (A), concentration (B) and flow field (C) all show strong channeling.s

Comparison of breakthrough curves for different domain sizes are shown in Figure 6.17. Pore volumes to breakthrough are significantly reduced compared to the single network model, and both two-scale continuum model trials have an optimum pore volumes to breakthrough of similar magnitude to experiments (0.74, 0.40 vs. 0.53). Additionally, breakthrough in the two-scale continuum models is much less sensitive to injection rate, which is also in agreement with experimental trends.

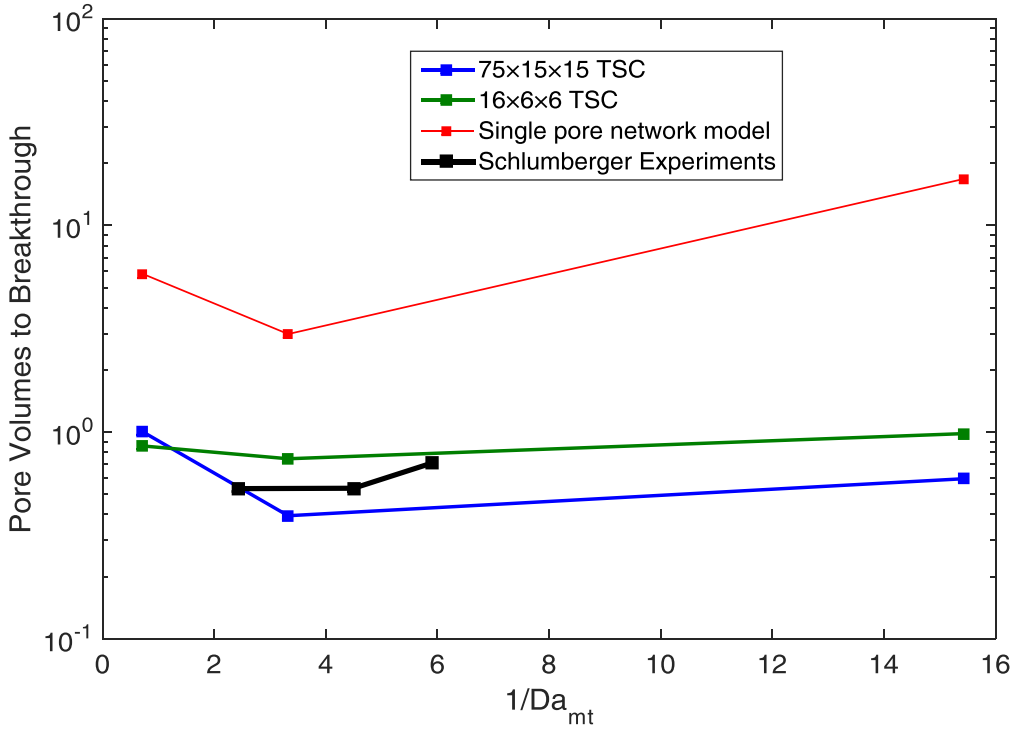

Figure 6.17: Pore volumes to breakthrough curve for TSC, pore network models, and Schlumberger experiments.

In addition to modeling core-scale experiments, the two-scale continuum model can be extended to model acidizing in radial flow. 2D simulations on 200×200×1 grid blocks (115×115×1 mm) are conducted with constant rate injection into central blocks.

Outer boundaries are open to flow with pressure and concentration equal to zero. Domain permeability is defined by:

$$k = \frac{\mu \ln(r_e / r_w)}{2\pi kh(p_e - p_{wf})} \quad (6.6)$$

where r_e is the external radius of an circle inscribed on the domain, r_w is the radius of central injection blocks, p_e is the average pressure at r_e, and p_{wf} is the pressure at r_w. Permeability heterogeneity is again modeled as a uniform distribution within 10% of mean permeability. An injection rate of 32 mm^3/sec is found to be optimal for the current configuration. Simulation outcomes for this injection rate are shown in Figure 6.18. Breakthrough occurs at the righthand side of the domain after 0.77 pore volumes injected. Dominant channels appear to be aligned with the Cartesian grid, which may be due to insufficient domain heterogeneity.

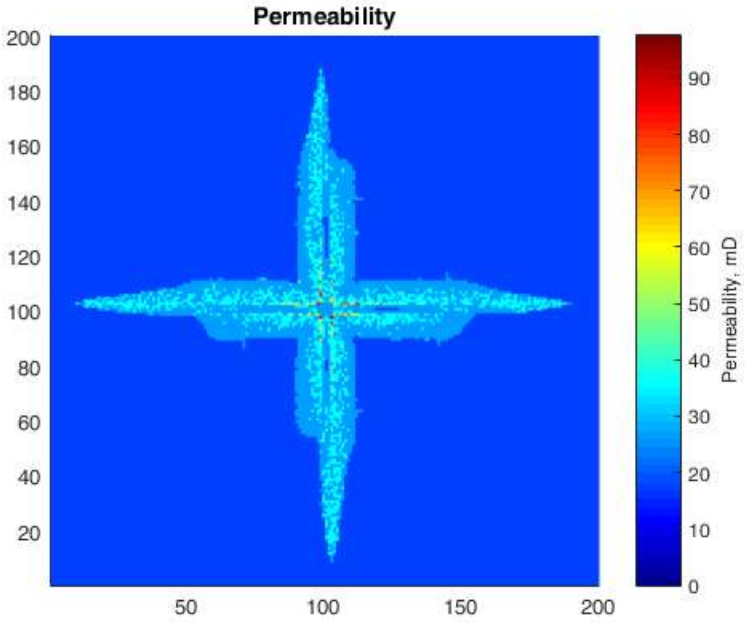

(A)

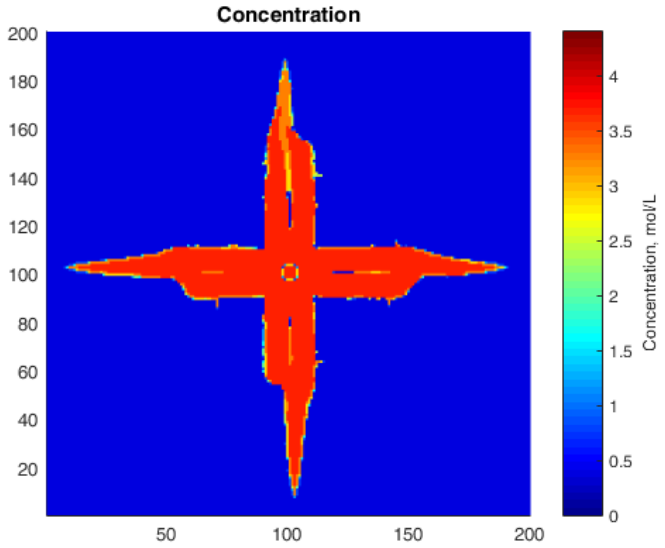

(B)

Figure 6.18: Continued on next page

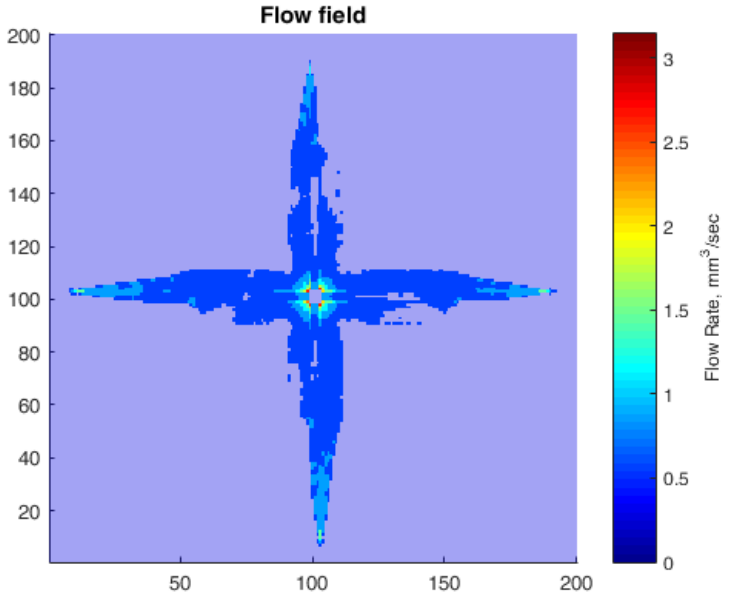

(C)

Figure 6.18: Visualization of 200×200×1 TSC simulation at breakthrough for radial flow. Permeability (A), concentration (B), and flow rates (C) show 4 dominant channels that emerge. Breakthrough occurs on the righthand channel, and is most evident in subplot C.

Figure 6.19 shows pore volumes injected vs. injection rates. The Pink Desert cores acidized by Schlumberger are not studied at a particularly wide range of injection rates, but the curve is much flatter compared to experimental core-scale values obtained by Fredd and Fogler (1999) (Figure 2.2). This suggests support for the field-scale practice of injecting at the maximum rate (below matrix fracture pressure) (Williams et al., 1979; Paccaloni and Tambini, 1993) as a strategy for acidizing optimization.

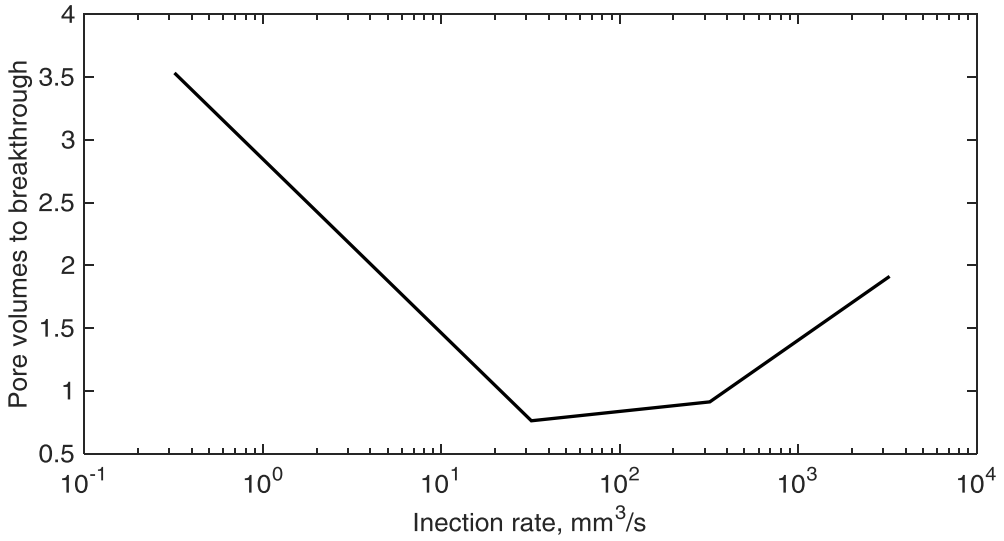

Figure 6.19 Pore volumes injected at various injection rates for 200×200×1 TSC simulation in radial flow.

The channeling observed along the Cartesian grid is likely due to insufficient heterogeneity. While small perturbations are sufficient to induce species channeling, the permeability field is still essentially homogeneous. A high-permeability region applied to the lower-left quadrant and a low-permeability region applied to the upper-right quadrant is also simulated (Figure 6.20), lowering breakthrough time significantly. Finally, a high permeability streak running diagonally is also simulated (Figure 6.21). These results help to indicate the high level of sensitivity radial acidizing has to heterogeneity. Future work could obtain a spatial correlation for heterogeneity via coarse CT scans of an entire core, correlating image density to porosity and permeability.

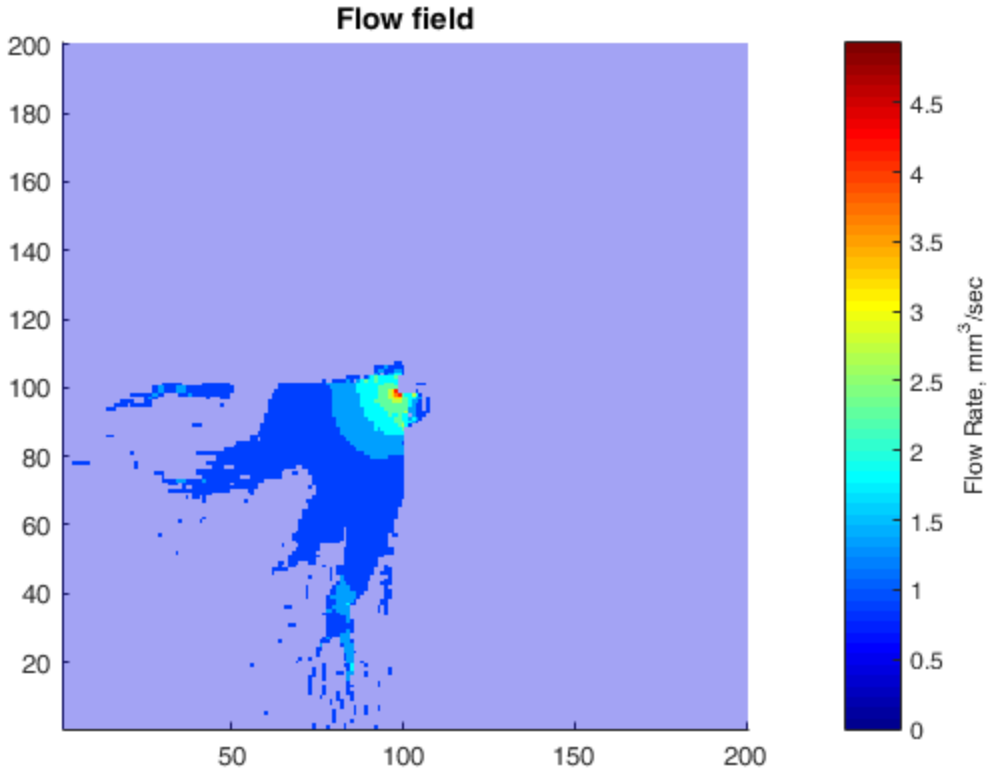

Figure 6.20: Flow field for 200×200×1 TSC simulation in radial flow, visualized at 0.34 pore volumes injected. Permeability field is enhanced by a factor of 10 in the lower left quadrant, while reduced by a factor of 10 in the upper right quadrant. Nearly all fluid flows through channels created in the high permeability region.

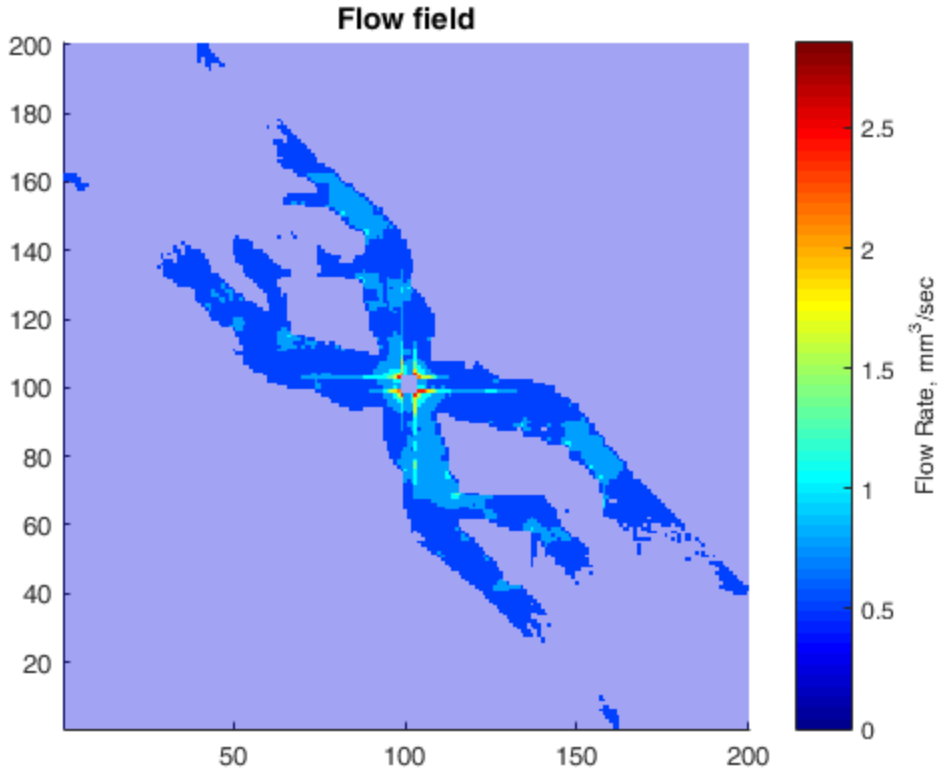

Figure 6.21: Flow field for for 200×200×1 TSC simulation in radial flow, visualized at 0.91 pore volumes injected. A high permeability streak runs diagonally, and is enlarged during acidization.

6.4 Discussion

The hybrid modeling approach has great utility in simplifying simulation physics at larger domain sizes. Extensive verification of the hybrid two-scale continuum approach is conducted before large scale simulations are made. Unfortunately, a sophisticated two-scale continuum model cannot replace computationally expensive network models in all cases. Network models are necessary to capture the heterogeneous outlet concentration

profiles seen at intermediate flow rates. Nonetheless, the full hybrid modeling algorithm is an accurate representation of pore-scale physics that improves computation time at larger domain sizes.

Large scale simulations using the hybrid method show reduced pore volumes to breakthrough. Theoretically, very large domain sizes (1000's of blocks) could be simulated with only the need to model a small percentage of blocks using pore network models. This would allow exploration of the REV for pore volumes to breakthrough, since it is currently unclear whether this property continues scaling downwards with domain size.

A full two-scale continuum model is also developed and tested. Its speed is many times faster than pore network models, allowing thousands of grid blocks to be simulated easily on a single processor. Model inputs are all obtained from simulations on a single pore network model. The expected wormholing regimes are captured, preserving the optimal inection rate of $Da_{mt} = 0.30$. Pore volumes to breakthrough are significantly lower at large domain sizes, which is in accordance with experiments conducted on Pink Desert carbonate cores. Radial models of acidizing show channeling of acid and characteristic dissolution regimes, providing insight into field-scale acidizing practices. Pore-scale heterogeneity is a key model input and shown to significantly affect wormholing patterns.

Chapter 7: Conclusions and Future Work

7.1 PORE-NETWORK MODEL DEVELOPMENT

In chapter 3, a pore network model is presented that establishes an effective method for *a priori* modeling of dissolution using only a network representation of the pore space. With novel implementation of pore-scale physics, the network model is able to capture the familiar dissolution regimes of matrix acidizing and return an optimal Damköhler number of 0.26, which matches favorably to the values of 0.29 commonly found in experiments. This is a significant improvement over the prediction of 0.028 in Fredd and Fogler (1998b).

In contrast to a conventional static rate expression, flow rate is shown to exert a strong effect on mass transfer via compression of the boundary layer. For mass transfer-limited systems, such as the dissolution of calcium carbonate by hydrochloric acid, this effect is likely to be significant. The sizing of pore geometry and flow field strongly determine the rate at which acid can be delivered to the virtually infinitely reactive surface. Additionally, mass transfer resistance induced by ionic resistance to products is easily incorporated into our dimensionless model by a scaling parameter.

The development of a pore merging criterion is shown to be highly important to capturing channeling and breakthrough. Without merging, permeability plateaus and no wormholing occurs. The pore merging criterion developed provides a physical basis for merging in the context of pore network models.

Domain size, a commonly cited drawback of pore network models, is not shown to strongly affect pore volumes to breakthrough or optimal injection conditions. This implies the suitability of extrapolating results, such as optimal injection conditions or a permeability-porosity ratio, for appropriate input in larger-scale models.

Three major areas of future work can be motivated by this chapter. First, comparison was only made with experimental averages. Acidizing experiments on a well-defined micromodel of a porous medium or micromodel constructed from calcite would represent an idealized way to test the pore network model. Exact pore locations and throat conductivities could be obtained, allowing a more direct test of reaction kinetics and pore growth merging algorithms. Alternatively, a homogeneous bead packing could be well-approximated by a pore network model. Experiments conducted on a calcite bead pack would likely return an optimal Damköhler number close to 0.29, but would determine whether the relatively large number of pore volumes to breakthrough seen in network models is representative of real sphere packs

Second, the expression for the mass transfer coefficient and pore merging algorithm were developed in COMSOL under the assumption of spherical pores. In actual simulation, pore surface area was seeded from the initial network extraction algorithm. The ratio of surface area to volume was kept constant (Eqn. 3.23). In practice, pores are initially more likely to be concave than convex. Therefore it is likely that mass transfer is underestimated in irregular and angular pores. However, as pores grow, mass transfer is amplified in throat constrictions. Therefore it is hypothesized that at intermediate and advanced stages of dissolution, pores approach a spherical geometry.

COMSOL simulations could verify the effect for sphere packs using a Delaunay tessellation cell (Figure 7.1) instead of spherical pore geometry. Spheres could be used to represent the grains (no-flow and zero concentration boundary conditions) with constant pressure on each face of the tetrahedron. Total mass transfer rate could be recorded, as before. Additionally, the evolution of the pore space could be approximated by dissolving walls in proportion to their local-element species flux. This could provide key insights into changes in mass transfer coefficient during pore dissolution. The effects could be upscaled into a pore network model by assigning pores an initial value for "sphericity" that correlates with mass transfer, and also evolves as the pore dissolves.

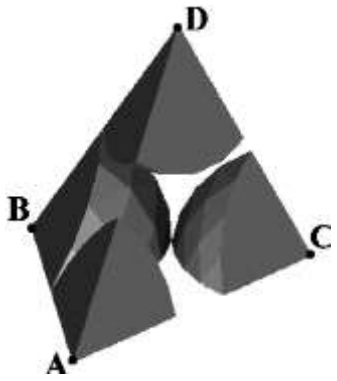

Figure 7.1: Delaunay cell in homogeneous sphere pack (Mahmoodlu et al. 2016)

The third area in which the network model could be expanded is to adapt the physics beyond the HCl-calcite reaction. This is partially investigated in chapter 4, where models for non-Newtonian acids are proposed, but there are a very large number of weaker acids that are not described by the mass-transfer limited assumptions that hold for HCl-calcite. Acids CDTA, DTPA, EDTA, and Hac are all reported by Fredd and Fogler (1999) to

have complex reaction kinetics that are a function of pH and temperature, often becoming partially reaction-rate limited.

Unfortunately, pore network models are likely a poor tool for modeling non-Newtonian acids. Because shear-rate is domain size dependent, reaching an REV either requires a model with the same domain size as the calibrating experiments, or reaching a shear rate at the asymptotic values for rheological properties. Two-scale continuum models are likely the best approach for non-Newtonian acidizing fluids, since these larger domain sizes are more easily achievable.

7.2 PORE-NETWORK MODELING OF CARBONATES

In Chapter 4, Newtonian simulations were performed on networks from all 5 rock types. Optimal injection rates are well-predicted when simulated nonreactive tracers match experimental tracers. This implies that nonreactive tracers are sufficient validation of the extracted network model to be used to predict acidizing behavior. Breakthrough curves capture the expected extreme inefficiency of face dissolution, and return a modest slope at faster injection rates that is consistent with experimental data points (Fredd and Fogler 1999).

Unfortunately, the majority of simulated rock types match experimental values poorly. Porosity is systematically underpredicted, but matches CT scan porosity (binary voxel space) almost exactly. This indicates an intrinsic defect in image acquisition or segmentation, whereby some porosity is omitted. Some microporosity is likely to be lost, since the scanning technique would not capture pores below the 2.2 micron resolution.

Additionally, segmentation techniques (indicator Kriging) tend to "smear" fine-scale features since they assume adjacent thresholded voxel values are spatially correlated.

While it is impractical to re-scan the entire imagine domain at finer resolution, one possibility is to determine the microporosity structure from an extremely fine resolution domain (smaller than the 1-2 mm length domains studied herein). This microporosity structure could be incorporated statistically into the larger-scale pore network model. Mehmani and Prodanović (2014) provide a novel method for incorporating microporous structures into a two-scale pore network model. Microporosity is likely to be important in poorly-connected media where a significant amount of flow must pass through intragranular microporosity. The Austin Chalk, whose CT scan was found to be unconnected when taken as a whole, is likely to benefit significantly from the inclusion of microporosity.

Permeability predicted by network models constructed from the carbonate CT scans is also poorly matched for most rock types, normally falling within a factor of two of the experimental value. For most rock types, this discrepancy is not likely to be due to lack of porosity, as a common trend is for porosity to be lower while network permeability higher than seen in experiments. For example, the Edwards Yellow network porosity is missing 12.5 porosity units (PUs), while predicted permeability is almost double experimental values (Table 4.2). The most likely explanation is that networks are below an REV for permeability in carbonates.

The systematically higher permeability is likely reflected in the extreme channeling seen in network tracers. Breakthrough occurs for all rock types at a value of 0.05, which

is roughly a factor of 10 sooner than seen in experiments. The Indiana Limestone is investigated in great detail, conducting simulations using different pore-scale modeling techniques, and obtaining an additional CT scan. Deficiency in modeling technique is mostly ruled out as a plausible cause for significant error in the flow field. The best conclusion is that samples are below a representative elementary volume. It is suggested that coarser-scale CT scans ought to maintain essential medium textures while expanding the domain size, since in many cases the medium's pore size is very large compared to the simulated domain. Alternatively, CT scan resolution could be maintained if several adjacent sections of the rock were scanned. A composite network could be accurately created using the mortar coupling techniques outlined in chapter 5.

Despite poor match of permeability and tracers for most rock types, acidization simulations were conducted on the networks. The simulated PVBT is higher in most cases, whether this is due to the REV issues discussed above, or to an intrinsic defect in the pore network modeling technique remains unclear. Additionally, all rock types return an optimal Damköhler number close to the global average value of 0.29. This appears to be at odds with experimental values, however experimental data point density is on the order of 0.1 Damköhler number resolution. Additionally, the "optimal" Damköhler number in experiments often corresponds to a negligible change in pore volumes to breakthrough. For example, at Da_{mt} = 0.23 and 0.42, the experimental PVBT for Pink Desert was 0.54 and 0.53 respectively, while the simulation optimal Da_{mt} was 0.30.

While it is encouraging for simulated values and dissolution regimes to fall within indistinguishable experimental ranges, it remains unclear whether extracted networks

truly capture the petrophysical texture of their corresponding rock types. All carbonate networks show a similar optimal Damköhler number. With the exception of the Austin Chalk, they also show similar shape in pore volumes to breakthrough curve (Figure 4.17). Therefore, the possibility exists that network models produce similar results regardless of their input. Note that this universal behavior is also observed in experiments conducted on a variety of rock/fluid systems (Fredd and Fogler, 1999), making it intrinsically difficult to study petrophysical texture in acidization. Future work could test the hypothesis that rock type is mostly irrelevant with respect to acidization optimization by performing experiments on a variety of rock types across a wider range of Damköhler numbers than studied herein. Confirmation of this hypothesis would drastically simplify future simulation and predictive efforts in matrix acidization topics.

Simulations of emulsified acid with a power law model reveal that changes to the flow field are small do not significantly affect acidizing efficiency, illustrating that fluid diversion is not a relevant feature of emulsified acids. A static retarded diffusion coefficient is also investigated, and shown merely to shift the PVBT curve leftwards without introducing any fundamentally different physics. However, a dynamic semi-empirical diffusion coefficient was able to replicate the relative insensitivity to injection rate and universally lowered PVBT. This approach is found to enhance mass transfer along the dominant flow path during dissolution. As discussed in section 7.1, pore-network models are likely poor candidates for simulating larger-scale experiments with non-Newtonian fluids. However, micromodel experiments would eliminate the shear rate discrepancy, and provide an accurate method by which pore-scale models could be

calibrated. Future mortar coupling techniques may allow sufficiently large-scale simulations such that a 1:1 match of simulation and experimental domain size can be achieved.

One other aspect of emulsified acids is the effect of micelle diameter on advection. Micelle diameter is usually assumed to be sufficiently small compared to pore-throat diameters, but it is possible for this effect to become significant, particularly in micropores. Sidaoui et al., (2016) estimate droplet size to be between 1 and 600 microns, while average pore body diameter in the Indiana Limestone is 23.6 microns. This could provide an alternative mechanism of pore-scale acid diversion in carbonates, as reduction of flow in low-conductivity regions would have the same effect as the semi-empirical shear-dependent diffusion coefficient developed in Chapter 4 (Figure 4.20). Fundamental experiments in simplified geometry are likely required to better understand the flow kinetics and mass transfer in emulsified acid.

7.3 DEVELOPMENT OF MORTAR COUPLING TECHNIQUE

Mortar coupling is shown to be an effective method to decompose networks into subdomains. For trials without pore merging, fine mortars are a highly accurate for capturing permeability, species transport, and reaction. Pore merging is challenging to incorporate across subdomains, but primarily effects simulations well-outside intermediate injection rates. At slow injection rates, extremely large pores created by face dissolution do not propagate correctly across the mortar boundary. At fast injection rates, uniform dissolution in the network creates a small but noticeable error at the mortar

boundary. Regardless, accuracy is extremely high for intermediate injection rates, suggesting the suitability of this simulation technique for larger-scale trials.

With respect to mortar resolution, mortars of infinitely small grid size are the most accurate choice, matching results given by the single-network solution with negligible error. However, while coarse mortars may effectively capture macroscopic measurements, they significantly alter property distributions in individual pores, which acidization patterns depend strongly upon. In particular, non-reactive tracer simulations show that coarse mortars are unacceptably inaccurate. However even simulation with the coarsest mortars captures the essential qualitative trends of acidization.

7.4 DEVELOPMENT OF HYBRID MODELING TECHNIQUE

The mortar coupling technique from chapter 5 is extended in chapter 6 to simulate multiple Pink Desert networks. However, it quickly becomes obvious that computational power is wasted simulated large parts of the nonreactive domain. A hybrid modeling technique using a Darcy scale model to simulate nonreactive blocks is shown to preserve a high degree of accuracy in acidization simulation. This technique is most useful at slow injection rates (face dissolution regime), where large parts of the domain remain unreactive. At intermediate and fast injection rates, acid propagates through most network blocks quickly, necessitating reactive modeling in the majority of blocks.

A two-scale continuum model is developed to supplement this hybrid modeling technique. In order to allow some reactive blocks to remain at the continuum scale,

correlations for the mass transfer coefficient, permeability-porosity relation, and surface area are developed in terms of block porosity and local Damköhler number. A single pore-network model is used to obtain these relationships *a priori*, which represents a significant departure from the semi-empirical approach employed by Panga et al. (2005) and Maheshwari et al. (2013). Comparison with their modified Kozeny-Carman model reveals significant underprediction of the permeability-porosity relationship seen in network models. Additionally, this relationship is shown to be a strong function of the local Damköhler number, a feature omitted by E 2.11.

The hybrid model incorporates pore networks and two-scale continuum models, and is shown to be accurate compared to the networks-only case. Unfortunately, the two-scale continuum model is not accurate enough to replace all network blocks. It is of particularly limited utility at intermediate injection rates, where most networks are undergoing significant dissolution, but are below the critical threshold of $Da_{mt} = 0.06$ to be replaced by two-scale continuum models. Therefore, the hybrid approach is most useful at slow injection rates, where most networks are non-reactive, or at fast injection rates where networks can be replaced by two-scale continuum blocks. Unfortunately, the two scale continuum model presented herein is not expected to accurately capture matrix acidization at larger domain sizes. Improvements in mesh size and representation of heterogeneity at the continuum scale are required for a fully flexible hybrid model that is valid at all injection rates. In the model's current state, it is much more accurate (but computationally expensive) to simulate uniform dissolution regimes with pore network models.

Future work includes simulation at much larger domain sizes. Currently, code is written in MATLAB, whose parallel structure necessitates a ratio of 1 "worker" per subdomain as the code is currently written. This is problematic because each worker requires a separate instance of MATLAB to be run in the background, a feature that quickly consumes large amounts of RAM. It would be possible, although counterintuitive and cumbersome, to allow multiple subdomains to be passed to each "worker". Furthermore, MATLAB's license for its parallel cluster environment (MDCS) is currently not implemented in most computation centers, including Texas Advanced Computing Center (TACC). As it stands, large-scale simulations on EC2 incur too much monetary expense for extended development. It is therefore recommended that the code be rewritten in a more mainstream and efficient coding language before massive parallelization is undertaken.

Larger and more complex domain sizes are an important step in future simulation of carbonate acidization. Cohen et al. (2008) found that simulations in radial geometries showed higher optimal injection rates than in linear core flood cases, suggesting that simple linear simulations are inapplicable to field conditions. Additionally, Bartko et al. (2007) found that perforations produce straighter and stronger wormholes than the unperforated (homogenous) case, implying that field-scale simulations of matrix acidization might benefit from including perforations near the wellbore.

To simulate radial flow around a wellbore, Sun et al. (2012) modeled single-phase, incompressible flow in a ~1 m^2 pore-scale region around a producing well coupled tolarger scale Darcy blocks. Over 7500 pore-scale models are coupled using mortars

(Figure 2.26). Sun showed that local pore scale heterogeneities significantly influenced the pressure field and flow path around the wellbore, implying that continuum models would poorly predict acid placement.

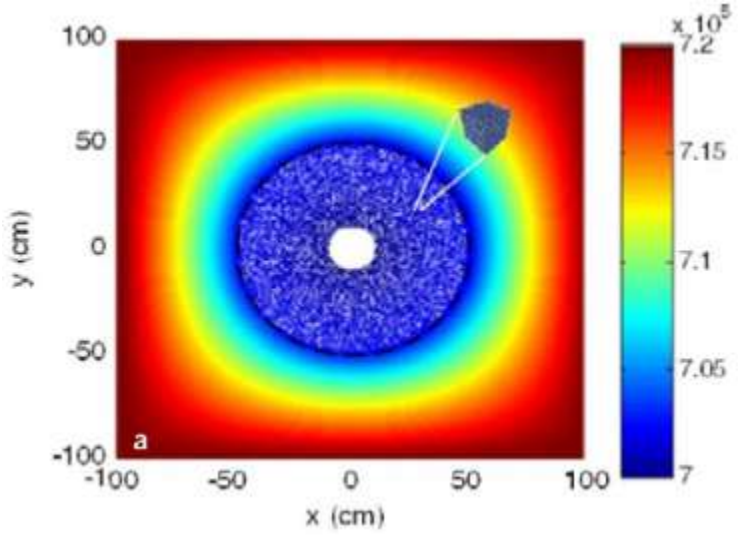

Figure 7.2: Pressure field produced by Sun et al. (2012). Pore scale models compose the near-wellbore region, while Darcy scale blocks make up the far field.

A useful extension of the near-wellbore model presented by Sun et al. (2012) would be integration with a conventional Darcy-scale reservoir simulator. Since acidization occurs primarily in the few feet around the wellbore, the vast majority of the reservoir could be simulated using Darcy-scale blocks. This approach has already been validated in section 6.1.1. Once acidization simulation is completed, the dissolved network models could continue to be simulated with the same physics as surrounding Darcy scale blocks. The simulation of pore space near the wellbore could prove more

accurate in simulating multiphase flow or reaction kinetics that would otherwise be lost in continuum scale blocks calibrated to non-acidized core-scale experiments.

The full two-scale continuum model is very promising. Structure-property relationships obtained from simulations on a single network are an *a priori* way to calibrate the two-scale continuum model without the need for destructive acidizing experiments. Results show wormholing occurs at the optimal Damkohler number of 0.30 for multiple domain sizes. Lowered pore volumes to breakthrough compared to single network models is also encouraging.

A major determinant of the model's dissolution pattern is how heterogeneity in the permeability field is introduced. One possibility is to scan an entire carbonate core at coarse-scale resolution, and use averaged CT scan signal intensity to determine porosity heterogeneity within the core. Correlations could relate permeability to porosity. Additionally, more networks could be extracted from different parts of the core, and multiple structure-property relationships obtained to investigate the effect of heterogeneity.

Once the model is calibrated, the studied core could be acidized and scanned again post-breakthrough. Comparisons between dissolution patterns and permeability response could be made. If a high degree of confidence in the two-scale continuum technique is obtained, the two-scale continuum model could easily be incorporated in the near-wellbore model without the need for an advanced parallel computing environment. This would allow field-scale recommendations to be based off the correct model

geometry, rather than assuming that core-scale performance can be applied to the wellbore environment without upscaling.

Appendix: Pore network models of carbonate rocks

In this section, the pore network models generated from CT scans of carbonate cores presented by Schlumberger are presented. Segmentation of greyscale CT images was achieved via indicator Kriging. Simulations for basic petrophysical properties (Table 4.2), nonreactive tracer (Figure 4.5, Table 4.3), and matrix acidization (Figure 4.7) are performed in chapter 4.

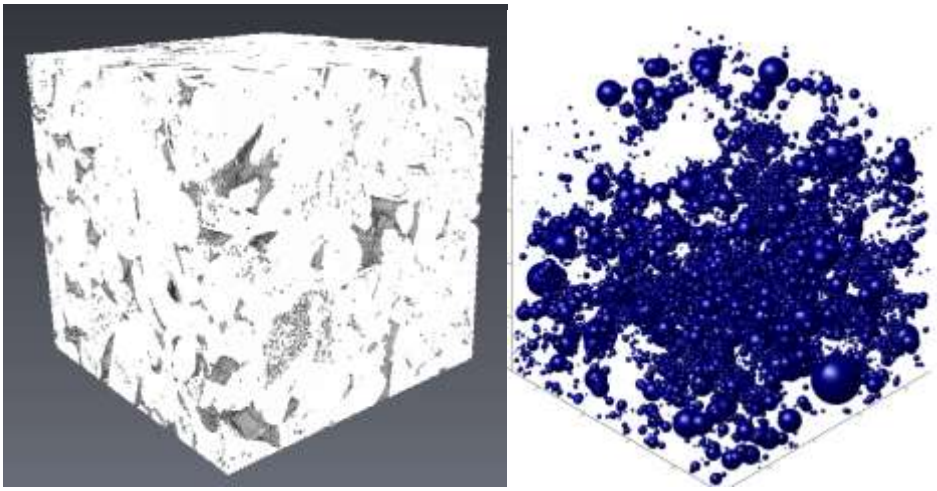

(A) (B)

Figure A.1: Indiana limestone binary voxel space (A) and pore network model (B)

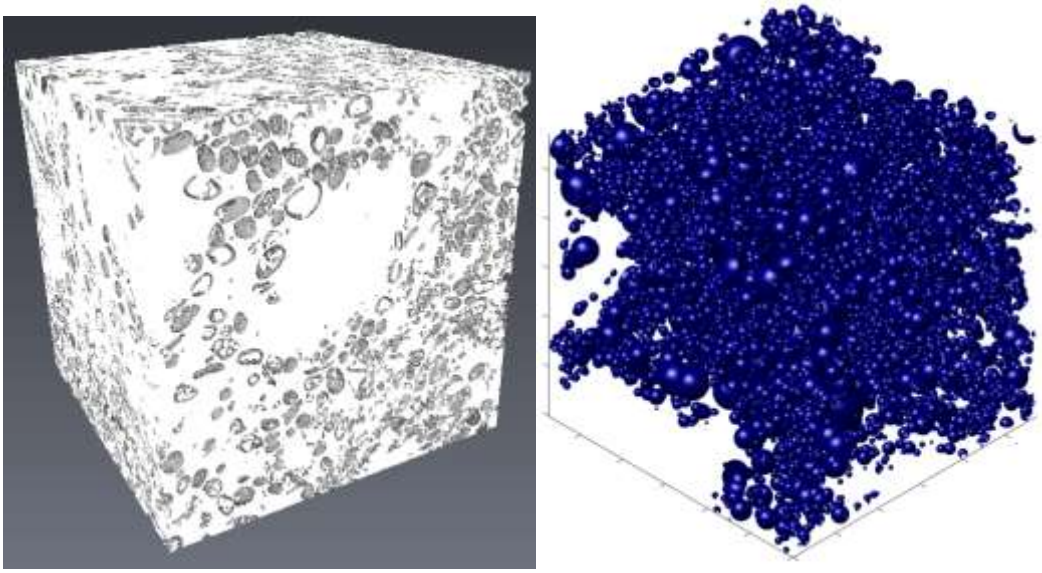

(A) (B)

Figure A.2: Edwards White binary voxel space (A) and pore network model (B)

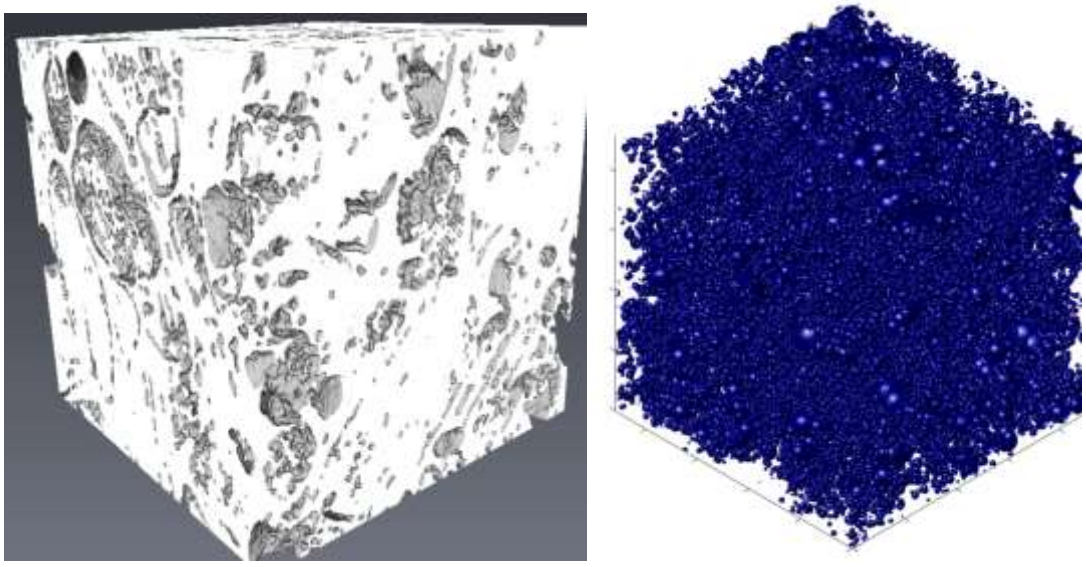

(A) (B)

Figure A.3: Edwards Yellow binary voxel space (A) and pore network model (B)

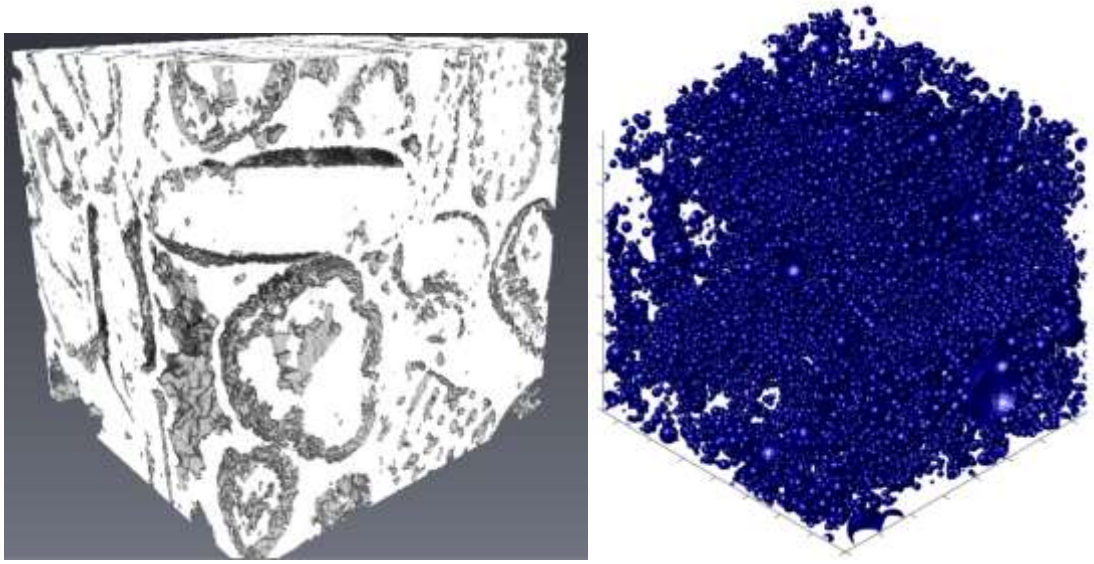

(A) (B)

Figure A.4: Austin Chalk binary voxel space (A) and pore network model (B)

References

Abass, Hazim Hussein, et al. "Acid fracturing or proppant fracturing in carbonate formation? A rock mechanics view." SPE Annual Technical Conference and Exhibition. Society of Petroleum Engineers, 2006.

Arbogast, T., Cowsar, L.C., Wheeler, M.F., Yotov, I.: Mixed finite element methods on nonmatching multiblock grids. SIAM Journal on Numerical Analysis 37 (4), 1295–1315 (2000)

Aharonov, E., Spiegelman, M., Kelemen, P.: Three-dimensional flow and reaction in porous media: Implications for the Earth's mantle and sedimentary basins. Journal of Geophysical Research 102 (B7), 14821 (1997)

Al-Dahlan, M. N., Nasr-El-Din, H.A.: A new technique to evaluate matrix acid treatments in carbonate reservoirs. Paper SPE-58714-MS, SPE International Symposium on Formation Damage Control, 23–24 February, Lafayette, Louisiana (2000). doi: /10.2118/58714-MS

Afsharpoor, Ali. *Pore-scale modeling of viscoelastic flow and the effect of polymer elasticity on residual oil saturation*. Diss. 2015.

Balakotaiah, Vemuri, and David H. West. "Shape normalization and analysis of the mass transfer controlled regime in catalytic monoliths." Chemical Engineering Science 57.8 (2002): 1269-1286.

Balhoff, Matthew T., Sunil G. Thomas, and Mary F. Wheeler. "Mortar coupling and upscaling of pore-scale models." *Computational Geosciences* 12.1 (2008): 15-27.

Balhoff, Matthew T., and Karsten E. Thompson. "A macroscopic model for shear-thinning flow in packed beds based on network modeling." *Chemical Engineering Science* 61.2 (2006): 698-719.

Ballard, Dana H., and Christopher M. Brown. "Computer vision, 1982." Prenice-Hall, Englewood Cliffs, NJ (1982).

Bazin, B.: From matrix acidizing to acid fracturing: A laboratory evaluation of acid/rock interactions. SPE Production & Facilities 16 (1), 22–29 (2001)

Berkowitz, Brian, Curt Naumann, and Leslie Smith. "Mass transfer at fracture intersections: An evaluation of mixing models." Water Resources Research 30.6 (1994): 1765-1773.

Bijeljic, Branko, and Martin J. Blunt. "Pore-scale modeling of transverse dispersion in porous media." Water Resources Research 43.12 (2007)

Bijeljic, B., A.H. Muggeridge, and M.J. Blunt (2004), Pore-scale modeling of longitudinal dispersion, *Water Resources Research 40, no. 11*.

Blunt, Martin J., et al. "Detailed physics, predictive capabilities and macroscopic consequences for pore-network models of multiphase flow." Advances in Water Resources 25.8 (2002): 1069-1089.

Bruderer, C., and Y. Bernabé (2001), *Network modeling of dispersion: Transition from Taylor dispersion in homogeneous networks to mechanical dispersion in very heterogeneous ones*, Water Resources Research 37, no. 4: 897-908.

Bryant, Steven L., Peter R. King, and David W. Mellor. "Network model evaluation of permeability and spatial correlation in a real random sphere packing." *Transport in Porous Media* 11.1 (1993): 53-70.

Budek, A., Szymczak, P.: Network models of dissolution of porous media. Physical Review E 86 (5), 056318 (2012)Buijse, M. A., Van Domelen, M. S.: Novel application of emulsified acids to matrix stimulation of heterogeneous formations. SPE Production & Facilities 15 (3), 208–213 (2000)

Buijse, M. A., Glasbergen. G.: A Semiempirical model to calculate wormhole growth in carbonate acidizing. Paper SPE-96892-MS, SPE Annual Technical Conference and Exhibition, Dallas, 9–12 October, Dallas, Texas (2005). doi: 10.2118/96892-MS

Carey, J. William, et al. "Experimental investigation of wellbore integrity and CO 2–brine flow along the casing–cement microannulus." International Journal of Greenhouse Gas Control 4.2 (2010): 272-282.

Chen, Yueting, et al. "Reaction-transport simulation of matrix acidizing and optimal acidizing strategies." *International Symposium on Oilfield Chemistry*. Society of Petroleum Engineers, 1997.

Christof M., Tuncay K.: Scale dependence of reaction rates in porous media. Advances in Water Resources 29 (1)): 62-71 (2006)

Cohen, Charles Edouard, et al. "From pore scale to wellbore scale: Impact of geometry on wormhole growth in carbonate acidization." *Chemical Engineering Science* 63.12 (2008): 3088-3099.

Cussler, E.L.: Diffusion: Mass Transfer in Fluid Systems. Cambridge University Press (2009)

Daccord, G., E. Touboul, and R. Lenormand. "Carbonate acidizing: toward a quantitative model of the wormholing phenomenon." SPE production engineering 4.01 (1989): 63-68.

Deidre, Taylor, et al. "Viscoelastic Surfactant Based Self-Diverting Acid for Enhanced Stimulation in Carbonate Reservoirs." *SPE European Formation Damage Conference*. 2003.

Ennis-King, J. P., Paterson, L.: Role of convective mixing in the long-term storage of carbon dioxide in deep saline formations. SPE Journal 10 (3), 349–356 (2005)
Fatt, Irving. "The network model of porous media." (1956).

Fredd, C. N., and H. Scott Fogler. "Alternative stimulation fluids and their impact on carbonate acidizing." *SPE Formation Damage Control Symposium*. Society of Petroleum Engineers, 1996.

Fredd, C. N., Fogler, H.S.: Alternative stimulation fluids and their impact on carbonate acidizing. SPE Journal 3 (1), 34–41 (1998a)

Fredd, C. N., Fogler, H.S.: Influence of transport and reaction on wormhole formation in porous media. AIChE journal 44 (9) 933-1949 (1998b)

Fredd, C. N., Fogler H. S.: Optimum conditions for wormhole formation in carbonate porous media: Influence of transport and reaction. SPE Journal 4 (3) 196-205 (1999)

Fredd, C. N. : Dynamic model of wormhole formation demonstrates conditions for effective skin reduction during carbonate matrix acidizing. Paper SPE-59537-MS *SPE Permian Basin Oil and Gas Recovery Conference*. Society of Petroleum Engineers (2000). doi: 10.2118/59537-ms

Ganis, B., et al. "A global jacobian method for simultaneous solution of mortar and subdomain variables in nonlinear porous media flow." ICES REPORT (2012): 12-46.

Gdanski, R: A Fundamentally New Model of Acid Wormholing in Carbonates. Paper SPE 54719 presented at the SPE European Formation Damage Conference, The Hague, The Netherlands, May 31-June 1. (1999). doi: 10.2118/54719-ms

Glover, Martin C., and James A. Guin. "Dissolution of a homogeneous porous medium by surface reaction." *AIChE Journal* 19.6 (1973): 1190-1195.

Golfier, F., Bazin, B., Zarcone, C., Lenormand, R., Lasseux, D., Quintard, M.: Acidizing carbonate reservoirs: numerical modelling of wormhole propagation and comparison to experiments. paper SPE 68922 21-22 (2001). doi: 10.2118/68922-ms
Gong, M., and A. M. El-Rabaa. "Quantitative model of wormholing process in carbonate acidizing." *SPE Mid-Continent Operations Symposium*. Society of Petroleum Engineers, 1999.

Hoefner, M. L., and H. Scott Fogler. "Pore evolution and channel formation during flow and reaction in porous media." *AIChE Journal* 34.1 (1988): 45-54.

Hoefner, M. L., and H. S. Fogler. "Fluid-velocity and reaction-rate effects during carbonate acidizing: application of network model." *SPE production engineering* 4.01 (1989): 56-62.

Huang, TianPing, A. D. Hill, and R. S. Schechter. "Reaction rate and fluid loss: The keys to wormhole initiation and propagation in carbonate acidizing."*International Symposium on Oilfield Chemistry*. Society of Petroleum Engineers, 1997.

Huang, T., L. Ostensen, and A. D. Hill. "Carbonate Matrix Acidizing with Acetic Acid." *SPE International Symposium on Formation Damage Control*. Society of Petroleum Engineers, 2000.

Hung, K. M., A. D. Hill, and K. Sepehrnoori. "A mechanistic model of wormhole growth in carbonate matrix acidizing and acid fracturing." *Journal of petroleum technology* 41.01 (1989): 59-66.

Jha, R. K., S. L. Bryant, and L.W. Lake (2011), Effect of diffusion on dispersion, SPE J., 16(1), 65–77.

Kang, Qinjun, et al. "Lattice Boltzmann simulation of chemical dissolution in porous media." *Physical Review E* 65.3 (2002): 036318.

Kang, Qinjun, et al. "Pore-scale study of dissolution-induced changes in permeability and porosity of porous media." *Journal of Hydrology* 517 (2014): 1049-1055.

Kalia, Nitika, and Vemuri Balakotaiah. "Modeling and analysis of wormhole formation in reactive dissolution of carbonate rocks." Chemical Engineering Science 62.4 (2007): 919-928.

Kim, D., Peters C. A., Lindquist W. B. :Upscaling geochemical reaction rates accompanying acidic CO2-saturated brine flow in sandstone aquifers. *Water Resources Research* 47 (1) (2011)

Klemmel, H. D. "World oil and gas reserves from analysis of giant fields and petroleum basins (provinces)." The Future Supply of Nature-Made Petroleum and Gas: Technical Reports (2013): 217.

Kelemen, P. B., Whitehead, J.A., Aharonov, E., Jordahl, K.A.: Experiments on flow focusing in soluble porous media, with applications to melt extraction from the mantle. Journal of Geophysical Research: Solid Earth (1978–2012) 100 (B1) 475-496 (1995)

Lee, Ta-Chih, Rangasami L. Kashyap, and Chong-Nam Chu. "Building skeleton models via 3-D medial surface axis thinning algorithms." CVGIP: Graphical Models and Image Processing 56.6 (1994): 462-478.

Levich, V.G.: Physicochemical Hydrodynamics, Prentice-Hall, Englewood Cliffs, New Jersey (1962)

Li L., Peters C.A., Celia M. A.: Upscaling geochemical reaction rates using pore-scale network modeling. Advances in Water Resources 29 (9) 1351-1370 (2006)

Lichtner, Peter C., and D. M. Tartakovsky. "Stochastic analysis of effective rate constant for heterogeneous reactions." *Stochastic Environmental Research and Risk Assessment* 17.6 (2003): 419-429.

Lindquist, W. Brent, et al. "Pore and throat size distributions measured from synchrotron X-ray tomographic images of Fontainebleau sandstones." Journal of Geophysical Research: Solid Earth 105.B9 (2000): 21509-21527.

Lopez, Xavier, Per H. Valvatne, and Martin J. Blunt. "Predictive network modeling of single-phase non-Newtonian flow in porous media." Journal of colloid and interface science 264.1 (2003): 256-265.

Lund, K., Fogler, H.S., McCune, C.C.: Acidization—II. The dissolution of calcite in hydrochloric acid. Chemical Engineering Science 30 (8) 825-835 (1975)

Lungwitz, B., et al. *Diversion and Cleanup Studies of Viscoelastic Surfactant-Based Self-Diverting Acid. SPEPO 22 (1): 121–127*. SPE-86504-PA. DOI: 10.2118/86504-PA, 2007.

Maheshwari, P., et al. "3-D simulation and analysis of reactive dissolution and wormhole formation in carbonate rocks." *Chemical Engineering Science* 90 (2013): 258-274.

Mahmoodlu, Mojtaba Ghareh, et al. "Effects of Sand Compaction and Mixing on Pore Structure and the Unsaturated Soil Hydraulic Properties." Vadose Zone Journal 15.8 (2016).

McDuff, Darren, et al. "Understanding wormholes in carbonates: Unprecedented experimental scale and 3-D visualization." SPE Annual Technical Conference and Exhibition. Society of Petroleum Engineers, 2010.

McLeod, Harry O. "Matrix acidizing." Journal of Petroleum Technology 36.12 (1984): 2-055.

McLeod, H. O. "Matrix Acidizing to Improve Well Performance." Short Course Manual. Richardson, Texas: SPE (1986).

Mehmani, Ayaz, and Maša Prodanović. "The effect of microporosity on transport properties in porous media." Advances in Water Resources 63 (2014): 104-119.

Mehmani, Y., Sun, T., Balhoff, M.R., Eichhubl, P., Bryant, S.: Multiblock Pore-Scale Modeling and Upscaling of Reactive Transport: Application to Carbon Sequestration. Transport in Porous Media 95(2) 305-326 (2012)

Mehmani, Y., Oostrom M., Balhoff M.T.: A streamline splitting pore-network approach for computationally inexpensive and accurate simulation of transport in porous media. Water Resources Research 50(3) 2488-2517 (2014)

Meile, Christof, and Kagan Tuncay. "Scale dependence of reaction rates in porous media." *Advances in Water Resources* 29.1 (2006): 62-71.

Mohamed S., Nasr-El-Din H., Al-Furaidan, Y.: Acid stimulation of power water injectors and saltwater disposal wells in a carbonate reservoir in Saudi Arabia: Laboratory testing and field results. Paper SPE-56533-MS SPE Annual Technical Conference and Exhibition. (1999)

Mostaghimi, Peyman, Min Liu, and Christoph H. Arns. "Numerical simulation of reactive transport on micro-CT images." Mathematical Geosciences 48.8 (2016): 963-983.

Mourzenko, V. V., et al. "Solute transport at fracture intersections." Water resources research 38.1 (2002).

Mumallah, N. A. "Factors influencing the reaction rate of hydrochloric acid and carbonate rock." SPE International Symposium on Oilfield Chemistry. Society of Petroleum Engineers, 1991.

Nasr-El-Din, Hisham A., et al. "Lessons Learned and Guidelines for Matrix Acidizing with Viscoelastic Surfactant Diversion in Carbonate Formations."*SPE Annual Technical Conference and Exhibition*. Society of Petroleum Engineers, 2006.

Nasr-El-Din, Hisham A., et al. "Evaluation of Methods to Improve Matrix Stimulation of Horizontal Carbonate Wellbores." Abu Dhabi International Petroleum Exhibition and Conference. Society of Petroleum Engineers, 2015.

Navarrete, R. C., et al. "Emulsified acid enhances well production in high-temperature carbonate formations." *European Petroleum Conference*. Society of Petroleum Engineers, 1998.

Noiriel, Catherine, Philippe Gouze, and Dominique Bernard. "Investigation of porosity and permeability effects from microstructure changes during limestone dissolution." Geophysical research letters 31.24 (2004).

Oh, Wonho, and Brent Lindquist. "Image thresholding by indicator kriging." IEEE Transactions on Pattern Analysis and Machine Intelligence 21.7 (1999): 590-602.

Paccaloni, Giovanni, and Mauro Tambini. "Advances in matrix stimulation technology." Journal of Petroleum Technology 45.03 (1993): 256-263.

Patzek, T. W., Silin D. B.: Shape factor and hydraulic conductance in noncircular capillaries: I. One-phase creeping flow. Journal of colloid and interface science 236(2) 295-304 (2001)

Panga, Mohan KR, Murtaza Ziauddin, and Vemuri Balakotaiah. "Two-scale continuum model for simulation of wormholes in carbonate acidization."*AIChE journal* 51.12 (2005): 3231-3248.

Peszyńska, Małgorzata, Mary F. Wheeler, and Ivan Yotov. "Mortar upscaling for multiphase flow in porous media." Computational Geosciences 6.1 (2002): 73-100.

Pomès, V., et al. "On the use of upscaling methods to describe acid injection in carbonates." *SPE Annual Technical Conference and Exhibition*. Society of Petroleum Engineers, 2001.

Qajar, Jafar, and Christoph H. Arns. "Characterization of reactive flow-induced evolution of carbonate rocks using digital core analysis-part 1: Assessment of pore-scale mineral dissolution and deposition." Journal of Contaminant Hydrology 192 (2016): 60-86.

Qiu, Xiangdong, et al. "Quantitative Modeling of Acid Wormholing in Carbonates-What Are the Gaps to Bridge." SPE Middle East Oil and Gas Show and Conference. Society of Petroleum Engineers, 2013.

Raoof, Amir, S. Majid Hassanizadeh, and Anton Leijnse. "Upscaling transport of adsorbing solutes in porous media: pore-network modeling." UNKNOWN 9.3 (2010): 624-636.

Raoof, A., Nick, H.M., Wolterbeek, T.K.T., Spiers, C.J.: Pore-scale modeling of reactive transport in wellbore cement under CO_2 storage conditions. International journal of greenhouse gas control11 S67-S77 (2012)

Schechter, R. S., and J. L. Gidley. "The change in pore size distribution from surface reactions in porous media." *AIChE Journal* 15.3 (1969): 339-350.

Scheibe, Timothy D., et al. "Hybrid numerical methods for multiscale simulations of subsurface biogeochemical processes." Journal of Physics: Conference Series. Vol. 78. No. 1. IOP Publishing, 2007.

Shin, Hyunkyung. A throat finding algorithm for medial axis analysis of 3D images of vesiculated basalts. Diss. State University of New York at Stony Brook, 2002.

Sheng, Qiang: Pore-To-Continuum Multiscale Modeling of Two-Phase Flow in Porous Media. Dissertation, Louisiana State University and Agricultural and Mechanical College, Department of Chemical Engineering. (2013)

Smith, C. F., and A. R. Hendrickson. "Hydrofluoric acid stimulation of sandstone reservoirs." *Journal of Petroleum Technology* 17.02 (1965): 215-222.

Stockman, Harlan W., Chunhong Li, and John L. Wilson. "A lattice-gas and lattice Boltzmann study of mixing at continuous fracture Junctions: Importance of boundary conditions." Geophysical research letters 24.12 (1997): 1515-1518.

Sun, Tie, Yashar Mehmani, and Matthew T. Balhoff. "Hybrid multiscale modeling through direct substitution of pore-scale models into near-well reservoir simulators." *Energy & Fuels* 26.9 (2012): 5828-5836.

Szymczak, P., and A. J. C. Ladd. "Wormhole formation in dissolving fractures." *Journal of Geophysical Research: Solid Earth* 114.B6 (2009).

Taylor, Deidre, et al. "Viscoelastic surfactant based self-diverting acid for enhanced stimulation in carbonate reservoirs." SPE European Formation Damage Conference. Society of Petroleum Engineers, 2003.

Talbot, Malcolm Seth, and Rick David Gdanski. "Beyond the Damköhler number: a new interpretation of carbonate wormholing." *Europec/EAGE Conference and Exhibition*. Society of Petroleum Engineers, 2008.

Thomas, R. L., Saxon A., Milne A. W.: The Use of Coiled Tubing During Matrix Acidizing of Carbonate Reservoirs Completed in Horizontal, Deviated, and Vertical Wells. SPE Production & Facilities 13(3) 147-162 (1998)

Thompson, K.E., Willson, C.S., White, C.D., Nyman, S., Bhattacharya, J.P., Reed, A.H.: Application of a new grain-based reconstruction algorithm to microtomography images for quantitative characterization and flow modeling. No. NRL/JA/7430-07-13. Naval Research Lab Stennis Space Center MS Marine Geoacoustics Division (2008)

Ulrich M.K., Frind, E.O., Blowes D.W.: Multicomponent reactive transport modeling in variably saturated porous media using a generalized formulation for kinetically controlled reactions. Water Resources Research 38 (9) 13-1 (2002)

Urdan, Timothy C. Statistics in plain English. Routledge, 2011.

Van Duijn, C. J., Pop I.S.: Crystal dissolution and precipitation in porous media: pore scale analysis. Journal für die reine und angewandte Mathematik (Crelle's Journal) 2004 (577) 171-211 (2004)

Walsh, Mark P., Larry W. Lake, and Robert S. Schechter. "A description of chemical precipitation mechanisms and their role in formation damage during stimulation by hydrofluoric acid." *Journal of Petroleum Technology* 34.09 (1982): 2-097.

Walsh, M. P., et al. "Precipitation and dissolution of solids attending flow through porous media." *AIChE Journal* 30.2 (1984): 317-328.

Wang, G. V., Vanka S. P.: Convective heat transfer in periodic wavy passages. International Journal of Heat and Mass Transfer 38 (17) 3219-3230 (1995)

Wang, Y., A. D. Hill, and R. S. Schechter. "The optimum injection rate for matrix acidizing of carbonate formations." SPE Annual Technical Conference and Exhibition. Society of Petroleum Engineers, 1993.

Wheeler, Mary F., et al. "A parallel multiblock/multidomain approach for reservoir simulation." Proceedings of the 15th Reservoir Simulation Symposium. No. 51884. 1999.

Wheeler, Mary F., John A. Wheeler, and Małgorzata Peszynska. "A distributed computing portal for coupling multi-physics and multiple domains in porous media." Computational Methods in Water Resources 12 (2000): 167-174.

Williams, B. B., et al. "Characterization of liquid-solid reactions. hydrochloric acid-calcium carbonate reaction." Industrial & Engineering Chemistry Fundamentals 9.4 (1970): 589-596.

Zakaria, A. S., H. A. Nasr-El-Din, and M. Ziauddin. "Flow of Emulsified Acid in Carbonate Rocks." *Industrial & Engineering Chemistry Research* 54.16 (2015): 4190-4202.